Membrane-based purification of nanoparticle dispersions

by

Nkem Alele

Thesis submitted to the Department of Chemistry of
Universität Duisburg-Essen, in partial fulfilment of
the requirements of the degree of
Dr. rer. nat.

Approved by the examining committee on the 9th of June 2016

Chair: Prof. Dr. Matthias Epple

Advisor: Prof. Dr. Mathias Ulbricht

Reviewer: Prof. Dr. Stephan Barcikowski

Essen, 2016

Abstract

Membrane-based separations of nanoparticles dispersion (i.e. mixtures of proteins and metal oxide nanoparticles) have received little or no attention. The conventional separation methods (e.g. centrifugation) often compromise the product's properties and recovery. In this work, a model study has been carried out by removing proteins (bovine serum albumin (BSA) or lysozyme (LYS)) from the dispersion mixtures with silica nanoparticles (nominal size 20 nm) by employing the sieving properties of ultrafiltration (UF) membranes. Membrane-based methods are easily scalable, less tedious and high throughput among other advantages. In this study, regenerated cellulose (RC) and polyethersulfone (PES) membranes with nominal molecular weight cut-off (NMWCO) of 100 kDa, and a PES UF membrane (NMWCO 300 kDa) functionalized with UV-grafted amphoteric polymer hydrogel layer consisting of *N*-[3-(dimethylamino)propyl]-acrylamide (DMAPAA) and 2-acrylamido-2-methyl-1-propanesulfonic acid (AMPS) and having an experimentally determined cut-off of 180 kDa (identical with the experimental data for PES 100 kDa) were studied. Some relevant membrane characterization such as contact angle, zeta potential as well SEM measurements were done to elucidate fractionation performance, anti-fouling properties and membrane-solute interactions. Membrane properties and filtration conditions, in particular pH value and flux, were selected or adapted based on data for single component feeds to achieve maximum protein transmission, complete silica retention and, hence, maximum silica/protein selectivity. Batch dead-end and continuous diafiltration processes were used for fractionation and purification. Overall, the performance of PES UF membranes was inferior compared to the other membranes because of too strong fouling. With membrane RC 100, the transmission data of LYS and BSA from the mixture with silica were 80 % and 30 %, respectively. With the hydrogel-functionalized or modified PES membrane, the respective

transmissions from the mixture were ~35 % and ~15 % for LYS and BSA, respectively. In both cases, quantitative rejection of silica could be achieved. Using continuous diafiltration, membrane RC 100 had better purification efficiency, removing a total of 91 % of LYS using 6 diavolumes (DV) in 2.4 h and 84 % of BSA using 10 DV in 5.5 h. With the hydrogel-functionalized PES membrane, 82 % of LYS and 74 % of BSA were removed using 6 and 10 DV within larger time, i.e. 4.0 and 6.8 h, respectively. Importantly, the retained silica nanoparticles remained stable in the dispersion, without any indication of aggregation.

The result of the model study was applied to show feasible benefits in biotechnological and medical fields were combination of nanoparticles with biomolecules to form functional hybrid systems demands high purity and separation of excess or unbound solutes. The RC membranes were used to separate unbound excessive ligands from the mixtures of gold nanoparticles-peptide bioconjugates (8.5 nm with dynamic light scattering) in a pressure driven diafiltration. This is pertinent because unbound ligands can compromise the specificity of bioassays and multivalent bioconjugation cannot be controlled without proper ligand removal. The RC membrane with NMWCO of 30 kDa showed absolute rejection of the bioconjugated AuNP. Using RC 30 kDa membrane, the recovery of AuNP-peptide bioconjugate in the retentate was > 87 % relative to the initial amount in the mixture. The latter results were additionally compared to the centrifugal membrane filtration method, where the efficiency of ligand removal and Au-peptide conjugate purity were found to be significantly lower than the ultrafiltration membrane method. All results indicate that RC membranes can be very well suited for the purification of bioconjugated nanoparticle dispersions and the diafiltration mode is much better suited for scale-up. Overall, this work has significantly expanded the knowledge about the use of membrane based separation methods for nanoparticle fractionation/purification as well as removal of residual reactants.

Dedication

This thesis is dedicated with great love to my wife (Jessica) and our wonderful children (Abigail and Caleb) both for their needed support, love, patience, tolerance and sacrifice provided over the duration of my doctorate study.

Acknowledgments

I heartily wish to express my profound gratitude to Prof. Dr. Mathias Ulbricht for opening the door of opportunity for me to work in his research group, His valuable guidance throughout the work and the uncommon experiences will remain indelible.

I would like to thank my reviewer Prof. Dr. Stephan Barcikowski for his support.

Special thanks are dedicated to Dr. Eberhard Wünn and Dr. Volkmar Thom, from Sartorius-Stedim Biotech GmbH, Göttingen, Germany, for providing the base membranes for this work.

I am grateful to Dipl.-Ing. Danielzik Inge, Dipl.-Ing. Kallweit Tobias and Claudia Schenk for the logistics and technical support during the course of this work.

I would like to acknowledge the René Streubel of (Lehrstuhl für Technische Chemie I/ Center for Nanointegration Duisburg-Essen (CENIDE)) for supplying bioconjugated-gold nanoparticle materials and the UV measurements. I also want to thank Lisa Gamrad of (Lehrstuhl für Technische Chemie I/ Center for Nanointegration Duisburg-Essen (CENIDE)) for supplying the centrifugation data used for comparison.

I wish to thank Benedikt Aumeier (M.Sc. Thesis), Ayu Mutiara Hapsari (M.Sc. Thesis), and Tyler Myers (RISE program) for their effort in working with me.

The shared experiences of Dr. Alexander Dundua, Ahmed and Ibrahim are all appreciated.

I appreciate the willing spirit of Dipl.-Ing. Smail Boukercha (Center for Scanning Electron Microscopy at UDE), Birgit Gleising (NanoEnergieTechnikZentrum /NETZ/) at UDE for conducting the SEM, SEM-EDX and TEM analyses.

The effort of Dieter Jacobi (Lehrstuhl für Technische Chemie I) and Dr. Jackelyn Aragon-Gomez (Lehrstuhl für Technische Chemie II) are acknowledged for performing most of the GPC analyses.

My kind regards to Prof. Dr. Ranil Wickramasinghe and Dr. Olusola O. James for their motivation during the course of this work.

I wish to extend my gratefulness to all those who directly and unknowingly might have contributed to the success of this work and the entire members of the Ulbricht group for their cooperative support, excellent and warm atmosphere.

I wish to especially acknowledge my good friend and colleague Mark Birkner who passed away on the 10 July 2015, your contribution towards the success of this work and the memories of our endeavors will endure.

Finally, my deep thanks go to my parents (Josephine and Julius Alele) and my siblings (Evarista, Onyeka, Glory, Osaro and Victor) in Nigeria for their prayers and spiritual support and most importantly our Almighty God Jehovah for his protection and the privilege of knowing him.

Declaration

I declare that this dissertation represents my own work, except where due acknowledgement is made.

Nkem Alele

Contents

1 Introduction

Separation techniques such as adsorption, absorption, distillation, extraction as well as filtration play a key role in product processing in all chemical related industries. However, membrane based separation processes are a growing preferred alternatives because of its beneficial characteristics such as low energy utilization, easy control of operation and lower waste generation. Membrane based separation processes particularly ultrafiltration (UF) and microfiltration (MF) are established separation technique in various applications, including water and wastewater treatment, purifications in biotechnological and pharmaceutical industries, food and beverage processing, and medical applications [1-4]. The most common applications of UF in biotechnology downstream processing are protein concentration and bioseparations in which traditional separation methods are less convenient, undesirable or even non-applicable. Others includes buffer exchange and desalting, virus removal and product clarification [5]. Current research and development efforts are directed towards large improvements in selectivity while maintaining the inherent high-throughput characteristics of membranes. Conflicting with those increasing demands are problems like concentration polarization and fouling which cause significant loss in performance with respect to flux and product selectivity. This is critical if membrane processes are to satisfy the new purification process and economic challenges, especially in biotechnology applications.

On the other hand, nanotechnology is presently attracting rapidly growing interest. The combination of metal or metal oxide nanoparticles (NP) with biomolecules to form bioconjugated systems is of great relevance for many applications, including drug delivery, target-specific therapy, as well as bio-imaging and sensing for diagnostic and therapeutic purposes [6]. However, purification of these NP-bioconjugates from free ligands such as

proteins still remains a challenge to achieve reproducible and well controlled performance in the intended applications. Primary requirements are a uniform particle size distribution and a high degree of purity. Those are needed to gain systematic insight into structure-function relationships. In addition, there is an increasing concern about NP impurities, especially for chemically synthesized nanomaterials. These potential impurities which may be harmful must also be removed from the final product. These impurities include organic solvents, surfactants, emulsifiers or stabilizers, monomer residues, polymerization initiators, large polymer aggregates and salts [7]. There have been various approaches employed for the purification of nanoparticles in general. Traditional techniques such as ultracentrifugation, extraction, size exclusion chromatography and dialysis are still being used for NP purifications which comprise ligand exchange, and many washing steps using differences in polarity, solubility and molecular weight, respectively. These separation methods are limited by many draw backs that include: low capacity, highly time consuming, product loss by non-specific binding, tedious recovery and large amounts of required solvents [8, 9].

The main advantages of membrane-based separation processes are high energy efficiency, easy scale-up, use at moderate temperature and pressure conditions as well as no requirement for additional separating agent (compared to chromatography) and either no or easy regeneration (in case membrane fouling can be minimized). Therefore, membrane separations are regarded as environmentally benign [10, 11].

In this study, membrane based method was further expanded to the separation of nanoparticle dispersion. The sieving properties of UF membranes were employed to remove proteins (BSA and LYS) from colloidal silica nanoparticle dispersions. In this model study, RC and PES UF membranes with different NMWCO were used. Membrane properties and filtration conditions, in particular pH value and flux, were selected or adapted based on data

for single component feeds to achieve maximum protein transmission, complete silica retention and, hence, maximum silica/protein selectivity during purification. To investigate an alternative to possible chemical instability problems associated with RC membranes and fouling problems with PES membranes, a higher MWCO PES was modified and also studied. PES is commonly used for the preparation of UF membranes due to their mechanical, chemical and thermal stability [12-15]. However, these materials are plagued by fouling during filtration, basically due to their relatively hydrophobic character. Through increasing the hydrophilicity the non-specific binding of product or other components to the membrane surface can be minimized. A hydrogel composite PES UF membrane was prepared using UV-initiated graft copolymerization ("grafting-from"; analogous to previous published work [16]), here yielding an amphoteric polymer hydrogel layer consisting of DMAPAA and AMPS.

The result of the model study was adapted to separate unbound excessive ligands from mixtures with gold nanoparticle-peptide bioconjugates in a pressure driven process. This work will expand the knowledge about the efficient use of polymeric UF membranes in solving separation challenges posed in the removal or purification of proteins from systems comprising other colloidal particles as well as unbound biomolecules from bioconjugated metal and noble metal nanoparticle dispersions.

2 Theory

2.1 Membrane processes and separation mechanism

The separation, concentration and purification of the chemical species present in a mixture is a major problem in the chemical process industry [17]. In recent years, traditional mass separation techniques such as distillation, crystallization, solvent extraction, etc. have been complemented by a class of processes which utilize semipermeable membranes as separation agents. In many cases, membrane separation processes are faster, more efficient and more economical than conventional separation techniques. For example, membrane processes offer significant advantages in the food and drug industries where separation is performed at ambient temperature, thus allowing temperature sensitive solutions to be handled without the constituents being denatured or chemically modified. Some other applications include; production of potable water, treatment of industrial effluents, metal and catalyst recovery, solvent recovery, gas separation and concentration of biological macromolecules and proteins etc. [17-19].

The transport of materials across a membrane barrier requires a driving force to effect separation. A chemical potential gradient provides the driving force for material transport from the upstream side of a membrane to the other. The chemical potential gradient can come from an electric potential difference, pressure difference, concentration difference, or temperature difference. Table 1 summarizes some technically relevant membrane separation processes, their operating principles, driving forces and some examples of application areas. The membrane itself is the key of every membrane process because of the ability to transport one component more preferable than the other due to differences in physical and/or chemical properties between the membrane and the permeating species.

Table 1: Some industrial membrane separation processes

Separation process	Membrane type	Driving force	Method of separation	Range of application
Microfiltration	(A)Symmetric, porous membrane 0.05 to 10 µm pore radius	Pressure difference 0.1 to 1 bar	Sieving mechanism	Sterile filtration, clarification
Ultrafiltration	Asymmetric microporous membrane 2 to 50 nm pore radius	Pressure difference 0.5 to 5 bar	Sieving mechanism	Separation of macromolecular solutions
Nanofiltration	Thin-film Composite < 2 nm pore size	Pressure difference 10 to 25 bar	Solution-diffusion mechanism	Desalination of brackish water
Reverse osmosis	Asymmetric "skin type" membrane, Thin-film Composite	Pressure difference 20 to 100 bar	Solution-diffusion mechanism	Separation of salts and microsolutes from solutions
Dialysis	Symmetric micro-porous membrane ≤ 2 nm pore diameter	Concentration gradient	Differences in diffusion rate, solution diffusion	Separation of salts and microsolutes from macromolecular solutions
Electrodialysis	Cation and anion exchange membrane nonporous	Electrical potential gradient	Electrical charge of particle & Donnan exclusion	Desalting of ionic solutions/water
Gas separations	Asymmetric or composite (elastomeric or glassy polymeric top layer), nonporous (or porous < 1 µm)	Pressure difference, concentration gradient	Solubility, diffusion	Separation of gas mixture

Other than the driving force, the membrane is the primary factor determining the selectivity and flux. In reality the nature of the membrane determines the type of application, covering the separation of microscopic particles to the separation of molecules of similar size or shape [20].

Synthetic membranes are produced from a variety of materials, including both organic and inorganic materials such as polymers, ceramics and metals. Ceramic and metal membranes can be employed in separations where aggressive media (e.g., acids, strong solvents) are present. They also have excellent thermal stability, which makes them suitable for high-temperature operations. Polymeric membranes dominate the market because they are less expensive and more versatile than inorganic membranes. Synthetic membranes can be classified as porous membranes (e.g., microfiltration, ultrafiltration) or nonporous (dense) membranes (reverse osmosis, nanofiltration, and gas separation) according to their structure and mechanism of separation (cf. Table 1) [17, 20]. The widely used preparation techniques are sintering, stretching, track-etching, phase inversion, sol-gel process, solution coating and vapour deposition. However, the technique employed depends on the material used, the targeted membrane structure and end use (separation problems or mechanism). Membrane separation can be performed either in dead-end flow mode or cross- flow mode.

In dead-end process, the feed stream moves perpendicular to the membrane surface and it passes through the membrane as permeate. Particulates and aggregates rejected by the membrane form a gel layer, which reduces flux and increases feed pressure over time.

In crossflow mode, the feed stream moves parallel to the membrane surface, and some portion of the feed stream permeates through the membrane as permeate while the rejected part of the feed stream becomes the retentate which can be further processed or recycled back to the feed.

The tangential feed stream which continuously sweeps across the upstream part of the membrane prevents or minimizes the buildup of particulates and aggregates and ensures a more steady permeate flux and low trans membrane pressure (TMP). Most large-scale industrial membrane separation processes operate in crossflow mode. Membrane filtration employs several different membrane formats (e.g., flat sheets and hollow fibers) and a wide variety of module designs (e.g., cassette, cartridge, and spiral-wound).

Required membrane properties include high porosity, narrow pore size distribution, sharp MWCO, high mechanical strength and flexibility, high pH and chemical stability. In addition, the desired surface properties (e.g., surface charge and hydrophilicity/hydrophobicity balance), low fouling tendency, and low cost.

Moreover, membrane separation processes also have some drawbacks that include concentration polarization/fouling, and low selectivity and flux.

2.1.1 Ultrafiltration

The most widely used membrane separation technologies are pressure-driven processes-reverse osmosis (RO), nanofiltration (NF), ultrafiltration (UF), and micro-filtration (MF). However further detailed discussion will be centered on UF because its separation regime is relevant to this work.

The UF characteristic lies between NF and MF with separation mechanism mainly due to “size exclusion” or “sieving” (Cf. Table 1). UF membranes are commonly used to reject relatively large dissolved macromolecules (e.g., proteins, polysaccharides) and suspended solids or particles (e.g., colloids, viruses) while allowing salts and smaller dissolved organic compounds to permeate [21]. UF membranes are typically classified by their ability to retain components of specific sizes dissolved in a solution. This is referred to as the molecular weight cut-off (MWCO), which is defined as the smallest molecular weight at which at least

90 % of the solute is rejected by the membrane. UF membranes generally have MWCO values between 1 kDa and 300 kDa and pore diameters in the range of ≤ 2 nm to 0.1 µm [1, 4]. UF membrane processes are mostly used in biopharmaceutical protein separation, virus clarification, and whey protein concentration, intermediate buffer exchange and isolation in the dairy industry. UF membranes are highly asymmetric; they have tight surfaces with small pores (skin layer) to provide the separation capability, and a large porous support that span through the rest of the membrane thickness to maximize flux. Crossflow filtration with flat-sheet cassettes dominates this application, although hollow-fiber cartridges are sometimes used. Membrane performance is typically characterized by the product rejection coefficient, which is defined as one minus the ratio of product concentration in the filtrate to product concentration in the feed.

UF is a well-known technique for macromolecular separation, it is supported by large scale production of membrane materials through phase inversion process with a typical cut−off in the range of about 5 to 200 kDa. Polymeric materials used for the fabrication of UF membranes include; polysulfone (PS), polyethersulfone (PES), polyacrylonitrile (PAN), cellulose−based polymers (mostly from cellulose acetate) and poly(vinylidene fluoride) (PVDF). Cellulose−based membranes such as regenerated cellulose (RC) are the state-of-the-art for low fouling UF membranes. In addition to the organic polymers, inorganic materials such as ceramic are presently used as UF membrane material. In biotechnology mostly RC and PES membranes are applied. The RC low protein binding property reduces fouling and improves yield and facilitates cleaning for reuse. However, PES material is much more resistant to extreme chemical conditions (acidic, basic and chloric), mechanical and also more stable to temperature exposure than cellulose based materials. Hence, due to the above mentioned advantages as well as its excellence film forming properties, PS and PES

are frequently used as materials for high performance UF membranes [22]. Nevertheless, the hydrophobicity of those materials can lead to high unspecific adsorption (e.g., proteins) causing severe fouling problem during application [23]. The ability to reduce fouling propensity, chemical and thermal resistance are important process performance indicators in UF operations.

UF versus diafiltration (DF) operations: UF and DF are primarily used as downstream processing steps for product concentration and/or buffer exchange. Both UF and DF have similar separation mechanisms (molecular/particle size dependent), with a porous membrane that, for instance, selectively rejects product and allows smaller substances (e.g., water, salts, residuals, etc.) to permeate through the membrane barrier. The setup of DF is also similar to UF, except for the addition of diafiltration buffer which is fed to the retentate volume at same flow the permeate is passing through the membrane. UF is most commonly used for concentrating a dilute product stream, while DF is a technique that uses UF membranes and is most often used to exchange a product into a desired buffer formulation. In biotechnological downstream processing, DF is also commonly used to prepare the product stream for chromatography step, to exchange drug product into the end formulation buffer, or other conditions where higher or lower conductivity/pH levels are required. DF can be performed in continuous and discontinuous or semi-continuous mode.

2.1.2 Transport Mechanisms

The most significant property of membranes is their ability to control the rate of permeation of different species [21]. The models used to describe the mechanism of permeation are the pore flow model and the solution-diffusion model. In the solution-diffusion model the permeate dissolve in the membrane material and then diffuse through the membrane down a concentration gradient. The permeate are separated because of the differences in the

solubilities of the materials in the membrane and the differences in the rates at which the materials diffuse through the membrane barrier. Examples of this transport mechanism occur in the reverse osmosis, pervaporation and polymeric gas separation membranes. In the pore-flow model, permeates are transported by pressure-driven convective flow through microporous membrane. Separation happens because one of the permeate is excluded (filtered) from some of the pores in the membrane through which other permeants passes the barrier. This transport mechanism occurs in the UF, MF and microporous gas flow membranes are mainly known as "size exclusion".

The fluid flow through the UF membrane can be described by the well-known Darcy equation [24].

$$J = \frac{K\,\Delta P}{\mu\,\Delta L} \tag{2.1}$$

The water flux J through the membrane is directly proportional to the applied pressure difference ΔP across the membrane. K is the specific permeability of the membrane, μ is the fluid viscosity and ΔX is the thickness of the membrane.

Considering the membrane barrier structure, laminar convective flow (solvent) through a porous system is better described by Hagen-Poiseuille's law with $K \approx \varepsilon\, r^2$. Here it is assumed that the membrane consists of straight capillaries or parallel array of nonintersecting cylindrical pores.

$$J = \frac{\varepsilon\, r^2 \Delta P}{8\,\eta\tau\Delta X} \tag{2.2}$$

Where r is pore radius, ΔX is the membrane thickness, η is the dynamic viscosity, τ is the tortuosity factor which is one for cylindrical pores and ε is the surface porosity of the membrane.

In reality the pores are interstices between closed-packed spheres as seen in sintered shapes, hence the Kozeny-Carman equation can be used:

$$J = \frac{\varepsilon^3 \Delta P}{K \eta S^2 \Delta X} \quad (2.3)$$

Where K is a dimensionless constant which depends on the pore geometry, S is the surface area of the spherical particles.

It should be noted that equations 2.1 through 2.3 only describe pure solvent flux in an ideal condition as well as membrane related parameters and none which apply to the solvent containing solutes [20].

2.1.3 Solute Transport

During UF process, solutes and/or particles are retained by the porous membrane. Solute is transmitted by convection towards the membrane as soon as the transport of solvent through the membrane commences. Therefore, the concentration is increased on the feed side of the membrane as solute is retained compared to the bulk solution. The concentration profile is exemplified in Figure 1 for a component *i* (labeled s in the figure) on both sides of the membrane and in the boundary layer, especially.

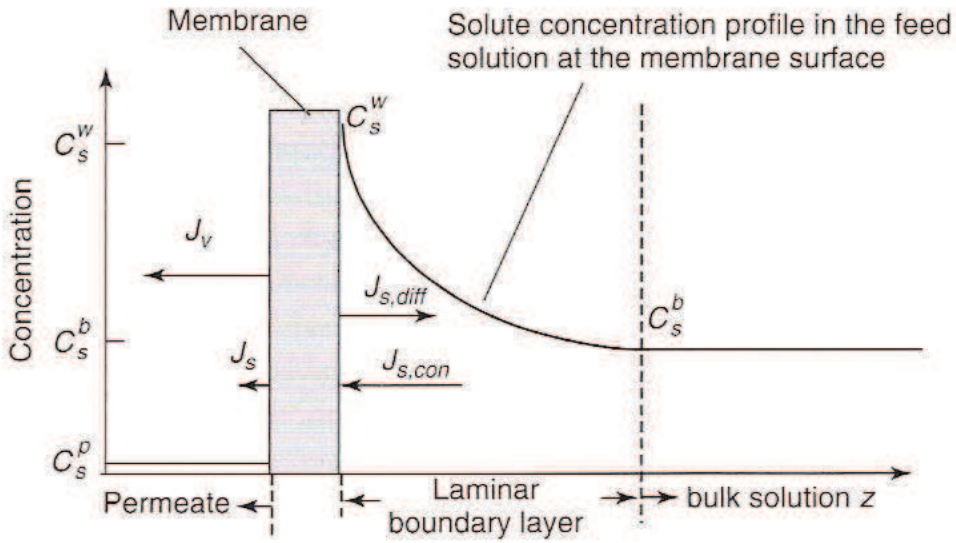

Figure 1: Fluxes and concentration profiles under steady state conditions in a membrane filtration process by film model [25]

This concentration gradient acts as driving force for component transport from the membrane-solution interface back into the bulk solution by diffusion. This phenomenon is called concentration polarization (CP). The osmotic pressure difference $\Delta\pi$ across the membrane can then become effective. The driving force of the solution is related by $\Delta P - \sigma\Delta\pi$, according to the 3-parameter model of Kedem and Katchalsky [26, 27]. The reflection coefficient σ indicates the degree of permselectivity of the membrane. When $\sigma = 1$ the solute is totally rejected and when $\sigma = 0$ it is totally permeable.

The resistance of the accumulated solute at the membrane surface is sometimes expressed as a hydraulic resistance R_S. If permeability is replaced by the hydraulic resistance in Darcy's equation (2.1) and taken into account the osmotic pressure of the solute, the UF flux may be described by the generalized equation:

$$J = \frac{\Delta P - \sigma\,\Delta\pi}{\mu(R_m + R_s)} \qquad (2.4)$$

Theoretical models: UF of macrosolutes causes an instantaneous and unavoidable reduction in flux relative to the pure water flux of the membrane. The polarization phenomenon to

which this loss of flux is ascribed to has been explained by mass transfer theory and classical fluid mechanics. The most wide spread theories include osmotic pressure model [28-30], the gel layer model [31, 32] and the resistance in series model [33, 34].

2.1.4 Fouling

Membrane fouling plays a major role in the effectiveness and economical feasibility of large-scale operation of pressure-driven membrane processes. Fouling is the deposition of suspended or dissolved substances on a membrane surface, at its pore openings, or within the pores [21]. Membrane systems are prone to different types of fouling. This includes inorganic fouling, particulate and colloidal fouling, organic fouling, and biofouling [34]. The result of fouling also causes a flux decline which is not reversible by simply changing the operating conditions. This is a major problem in UF since it reduces performance (productivity and selectivity), shortens membrane life (often due to aggressive cleaning agents) and impairs fractionation capability of the membrane [35]. The problem of fouling is often superimposed upon the concentration polarization. CP is the accumulation of the solute concentration at the membrane surface due to selectivity of the membrane. Although CP is reversible process it can facilitates irreversible membrane fouling by altering interactions among solvent, solute and membrane [36]. Fouling intensity depends on the membrane material, the nature of the solutes, and other variables such as concentration, pH, ionic strength, solution temperature, operating pressure and specific interactions (hydrogen bonding, dipole-dipole interactions) [20, 37].

Fouling mechanism

The phenomenon of membrane fouling is a very complex to describe theoretically, however pore blocking and cake formation are deemed the two main mechanisms of membrane fouling while other factors such as adsorption, particle deposition within the pores, and

changes to the cake layer affect membrane fouling through the modification of either one or both mechanisms [38]. The effects of such fouling types on the membrane pore size distribution are schematically described in Figure 2. In protein filtration process, hydrophobic protein-membrane interactions dominate the initial stage of the fouling behaviour (deposition on the membrane surface), in later stages protein-protein interaction determine the membrane performance (interactions of the bulk solutes with the deposited layer) [39, 40].

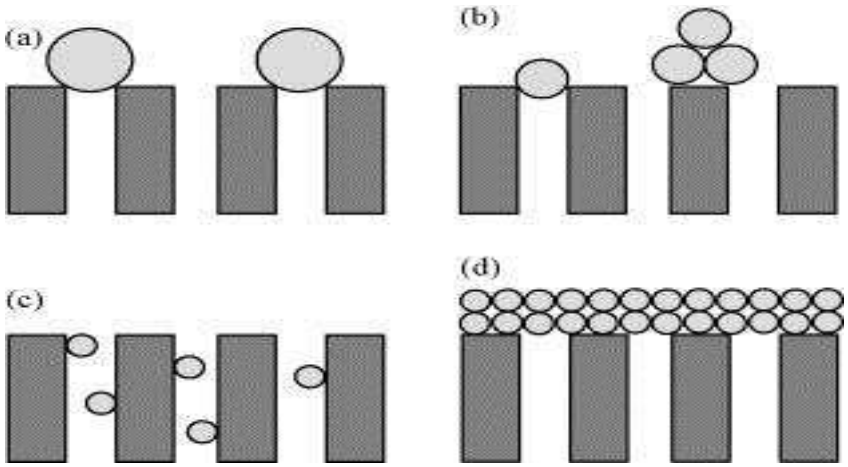

Figure 2: Illustration of the fouling mechanisms considered by the models: (a) complete blocking; (b) intermediate blocking; (c) standard blocking and (d) cake layer formation [41].

Bacchin *et al*. [42] further classified the pore/solute fouling using the following characteristics terms:

(a) Adsorption: Components adsorb onto the membrane, either on its surface or within its support structure. The reason for adsorption is the existence of solute-membrane interaction, i.e. hydrophobic interactions, van der Waals force attractions, electrostatic force interaction, or hydrogen bonding [25]. A monolayer of particles and solutes can occur even in the absence of permeation flux leading to an additional hydraulic resistance. If the degree of adsorption is concentration dependent then concentration polarization aggravates the amount of adsorption. Adsorbed molecules normally lead to narrowed pore diameters.

Adsorption is typically irreversible with physical cleaning measures, but may be reversed by the use of chemical cleaning.

(b) Pore blockage: During filtering, convective component transport can lead to pore blockage leading to a reduction of flux due to the closure (or partial closure) of pores. This can happen at the membrane surface or at pore constrictions within the support structure. Pore blocking may be reversible using physical cleaning measures (like backwashing).

(c) Deposit: The result of strong CP is deposition on the membrane surface, i.e. the formation of a cake layer (also called dynamic membrane). A deposit of the particle can grow layer by layer at the membrane surface leading to an additional hydraulic resistance. This is often referred to as a cake resistance. Component-component interactions govern this type of fouling [43]. Surface deposition is normally physically reversible (by external washing or backwashing).

(d) Gel: the level of concentration polarization may lead to gel formation for certain macromolecules.

Proteins and other biological components normally form more or less dense layers, whereas rigid particles such as silica-NPs tend to form more permeable layers [25].

As earlier mentioned, fouling can also be attributed to the flux decline over filtration time. De *et al*. [44] classified the flux decline in UF into short and long terms. The short term decline is an osmotic pressure controlled, while the long term decline is restrained by growth of polarized layer. Another classification given by L. Song [45] profiled the flux decline over time into three regions as depicted in Figure 3: (i) initiated by a rapid initial drop from the flux of pure water filtration, (ii) proceeded by a long term gradual flux decrease, and (iii) climaxed with a steady state flux.

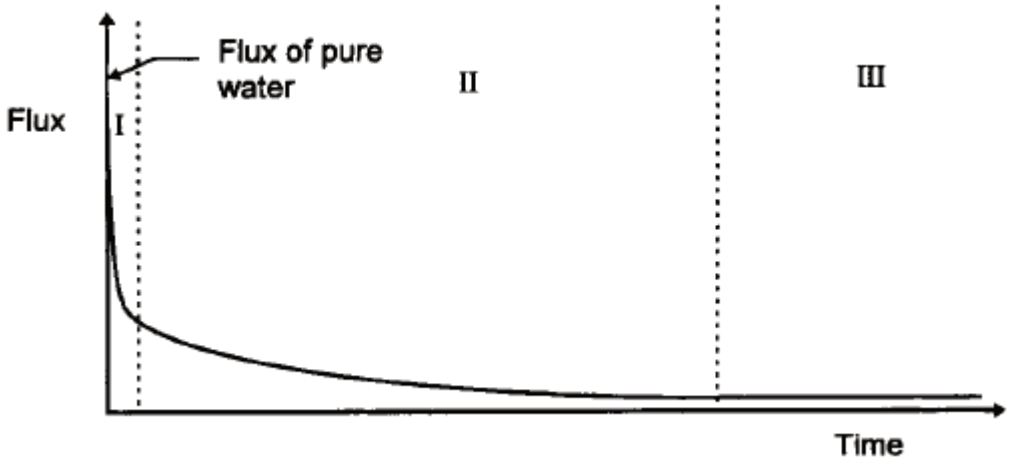

Figure 3: Schematic representation of three stages of time-dependent flux decline [45].

The classical fouling model developed by Hermia is often used to analyze the flux over time data in order to ascertain the fouling mechanism [46],

$$\frac{d^2t}{dV^2} = k\left(\frac{dt}{dV}\right)^n \tag{2.5}$$

Where t is the filtration time, V is total filtered volume, K is a fouling coefficient, and n is a dimensionless filtration constant reflecting the mode of fouling. Basically, that model defines three possible fouling mechanisms, i.e. pore blocking, pore constriction and cake formation (cf. Figure 2). Cake formation corresponds to the value of $n = 0$, whereas complete pore blocking corresponds to $n = 2$. Pore constriction is represented by the value of $n = 3/2$. (cf. ref. [41, 46, 47]). The required derivatives are evaluated in terms of the filtrate flux as follows:

$$\frac{dt}{dV} = \frac{1}{JA} \tag{2.6}$$

$$\frac{d^2t}{dV^2} = -\frac{1}{J^3A^2}\frac{dJ}{dt} \tag{2.7}$$

A is the effective membrane surface area and $\frac{dJ}{dt}$ was determined by differentiating the polynomials that gave the best fitting for the experimental data. It should be noted that this

model assumed uniform non-connected pores [46] which may not be the case for most UF membranes.

Critical flux

An important part of fouling studies is the critical flux determination. The critical flux is defined as the flux point where the permeate flux deviates from the linear dependence of the water flux with pressure, this is the "first" permeate flux at which fouling becomes noticeable [42, 48, 49]. This implies that a critical transmembrane pressure (TMP) corresponds to a given critical flux. Above the critical pressure, flux increases non-linearly with increasing TMP. It should be noted that operation below the critical point does not necessarily mean that no fouling will occur during the process, but it can be related to minimizing fouling [42]. At very high pressures, a limiting flux can be observed. Beyond this point the flux becomes independent from the applied pressure, i.e. no further increase in flux can be achieved by applying higher pressure. Bacchin *et al.* [42] gave a detailed overview on critical flux issues, (re-)defining a small set of critical fluxes depending on the corresponding experimental conditions and substances involved.

The strong form of critical flux is defined as the flux at which the flux-TMP curve starts to deviate from the linear slope of pure solvent flux. Therefore, adsorption and osmotic pressure (CP, respectively) are assumed to be negligible. In another hypothesis, a critical flux can exist below which the same transmembrane pressure (TMP) is required to maintain it when filtering a colloid as for clean water at the same flux [50, 51].

The weak form of critical flux is defined as the flux at which the flux-TMP curve starts to deviate from linearity. In this case, adsorption being independent of hydrodynamic conditions is allowed or at least tolerated. Thus, it addresses the deposition onto the membrane by convection. Sometimes the TMP required is greater than for clean water but

the TMP still increases linearly with the flux up to a critical flux [49]. Figure 4 illustrates the difference between the two forms of critical flux.

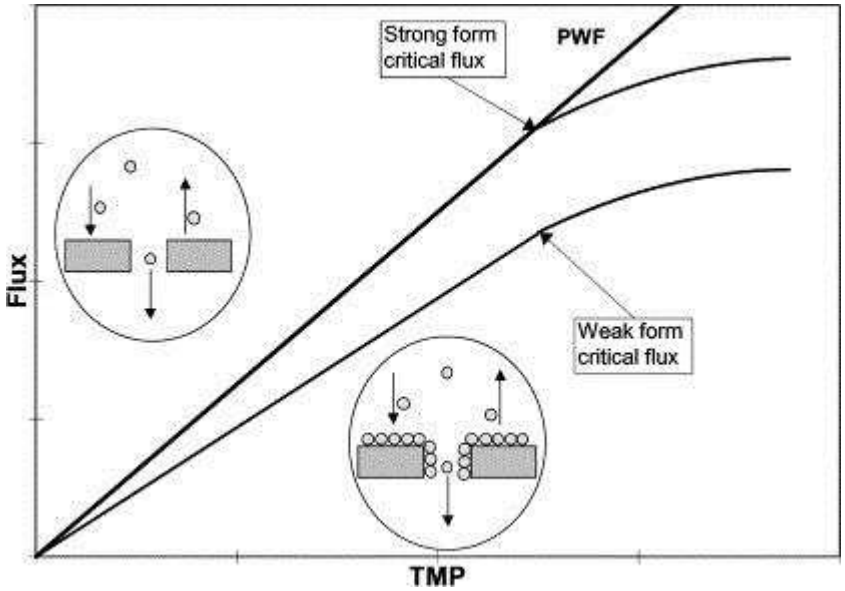

Figure 4: Schematic representation of a weak form and a strong form critical flux [49].

2.1.5 Factors affecting Fouling

The fouling mechanisms are governed by the solute/particle properties, the membrane characteristics and the hydrodynamic conditions during filtration.

Membrane properties

The membrane properties impacting fouling include hydrophilicity, surface topography, charge on the membrane surface, and pore structure. It is basically known that hydrophilic membranes show less fouling tendencies than those with hydrophobic properties [52-54]. Membrane that posses smooth and uniform surface tends to foul less than membrane with high surface roughness.

Surface charge of the membrane is also an important property especially for the processing of charged solutes and macromolecules. It is pertinent to note that most membranes and colloids have a negative charge under normal aqueous and natural conditions. As a result,

electrostatic repulsion should be maximized in order to reduce fouling. The membrane morphology (pore structure, porosity and pore connectivity) also influenced the fouling behavior [55]. The solute and membrane pore size ratio is also very important both in flux decline and in fouling rate. A usual rule of thumb is particle size to membrane pore size of 10, which means selecting a membrane with pores that are one-tenth the particle size on average, as initial starting point during testing [3].

Solution properties

The solute (solution) properties affecting the fouling include functional group content, solute charge (density), hydrophobicity, and the physical structure [3]. As a result of these solute properties, additional solution properties arise: salt (ionic strength), pH and cation content also impact the extent and the nature of fouling. Salts can increase the ionic strength, which in turn affects solute-solute and solute-membrane interactions. Mineral salts can also precipitate on the membrane surface because of poor solvation or bind to the membrane directly by charge interactions [3]. Increasing salt concentration will reduced electrostatic repulsion between similar charged materials i.e. increasing adsorption tendency, while decreased electrostatic attraction between unlike charged materials will lower fouling i.e. decreasing adsorption tendency [56]. Basically, pH influences the fouling by weak electrolyte colloids through the charge interaction. It is well known that lowest flux is attained at the isoelectric point (IEP) during colloidal filtration due to hydrophobic interaction. However, flux increases as the pH is moved away from the IEP. Moreover, the change in pH affects solubility and conformation of feed component. For example, the solubility of protein is usually low at the IEP. The charge density also plays an important part in membrane fouling. The protein charge density is at lowest at its IEP. Many investigations have shown that membranes were strongly fouled when the pH was tuned to the proteins IEP [39, 57, 58].

Operating parameters

Fouling is strongly influenced by process parameters including flow rate (cross flow velocity, stirring), pressure, feed concentration and temperature as well as overall equipment design. Temperature increase can either decrease or increase fouling during UF operations. This depends on the effects of temperature on the solubility of feed components, viscosity and diffusivity. Babu et al. [59] reported that the increase in temperature decreased the fouling during UF of BSA using cellulose triacetate and regenerated cellulose membrane. Mostly, at high flow rate or stirring rate the accumulated solutes components on the membrane surface tend to be swept from the membrane surface thereby reducing fouling layer growth. On the other hand, fouling at higher cross flow velocity have also been reported [60, 61]. Transmembrane pressure was also found to affect fouling: an increase in process pressure caused stronger permeate flux decline and increasing the cake resistance [62, 63]. The hydrodynamics can be impacted by the process design. Protein accumulation and fouling can be influenced by microcavitations in valves and pumps [2].

Strategies for fouling mitigation

According to the nature of the occurring and/or dominant fouling mechanism(s) different methods to prevent or control fouling may be applied:

• Pretreatment of the feed solution: chemical precipitation, prefiltration, pH adjustment, chlorination, carbon adsorption,

• Hydrodynamic optimization of the membrane module: increase of shear rate (high feed cross-flow velocity, stirring) by proper module design and/or operation,

• Membrane cleaning with proper chemical agents: backwash, acids and bases like HNO_3 and NaOH, complexing agents like EDTA, enzymes, detergents, and disinfectants [25].

• Membrane surface modifications: introduction of hydrophilic and/or charged groups.

2.1.6 Membrane surface modification

Membrane surface modification objectives are to either minimize undesired (secondary) interactions (adsorption or adhesion), which reduce the performance (membrane fouling), or to introduce additional interactions (affinity, responsive or catalytic properties) for improving the selectivity or creating an entirely novel separation function [64]. The membrane surface can be chemically treated in order to influence the hydrophilicity. The modified layer has been shown to decrease fouling during protein filtration [65]. Various works have been devoted to different polymer classes with respect to their affinity to proteins. The evaluated results have furnished a database of material properties which are responsible for eliminating or reducing fouling. The following characteristics have been identified as inherent: the investigated materials were hydrophilic, overall electrically neutral and hydrogen bond acceptors, but not hydrogen bond donors [66]. Membrane surface modification has wide application for minimizing fouling and achieving the desired membrane properties. UF membranes for industrial applications are prepared from PES, PSf and PVDF. Due to their rather hydrophobic character and susceptibility to fouling, the polymeric materials are usually modified. The following general strategies are often used for changing the material performance: bulk polymer modification and surface modification. During bulk polymer modification other active groups are chemically added to the polymer solution, after which, the membrane can be casted. Surface polymer modifications are further sub-divided into surface treatment with plasma, polymer blending, grafting methods and coating. Comprehensive overviews covering the development of UV-assisted grafting methods including tailored surfaced modification has been extensively investigated by Ulbricht et al. [64, 67-74]. Hence only membrane modification via activation by UV irradiation, which is relevant to this work, will be expanded.

Activation by UV irradiation

The commonly used technique for grafting initiation is the direct UV excitation due to its simplicity. However, this will work only for very few polymers, with such intrinsic photoreactivity. Photo-initiated functionalizations of polymeric membranes can be very selective and efficient in combination with low cost integration to large scale processes [75]. Ultraviolet (UV) irradiation is basically considered as a radiation that has a wave length ranging from 100 to 450 nm [76]. In this technique, the membrane is modified by growing polymer chains through free radical polymerization. The membrane surface is modified by a graft co-polymerization using the "grafting-from" mechanism. Contrary to "grafting-to" reactions where the already synthesized polymer chains (e.g. block co-polymer) are either adsorbed or chemically bonded to the base material, in grafting-from reactions functional monomers polymerize successively to an initiator group fixed on the base material or the latest bonded monomer, respectively. In this way the polymer chains grow from the surface and a higher density of functionalization is achieved compared to grafting-to reactions [77]. The mechanism of the initiation is schematically represented in Figure 5 [64]. In Figure 5 (a), UV light is used for the direct creation of radicals on the surface of UV active polymers, such as PSf or PES [67, 78]. That way, degradation of the membrane polymer occurs due to chemical bonds cleavage (e.g., the C-S bond of PES). In addition, moderate conditions ($\lambda >$ 300 nm) limit the change of morphology of the PES material through irradiation effectively [67].

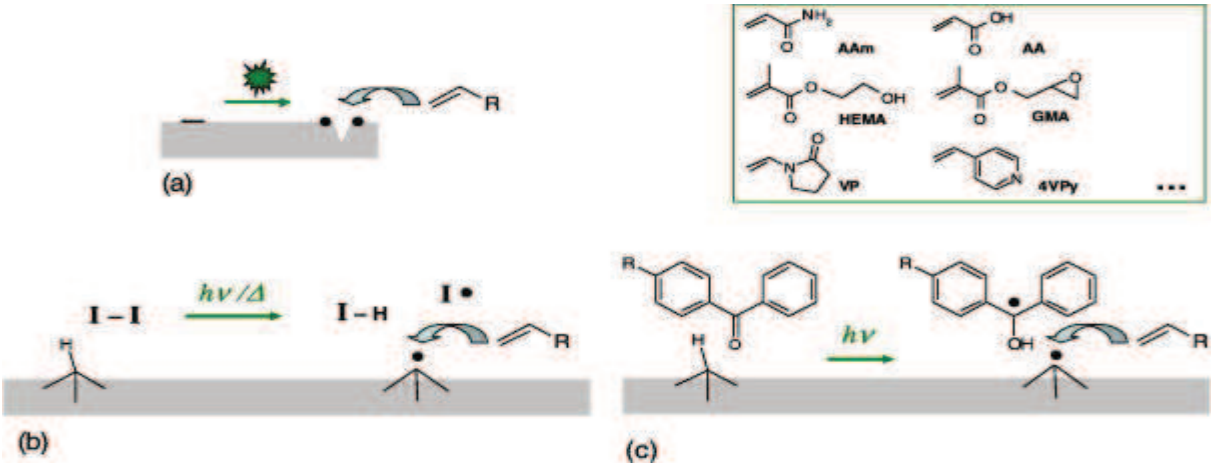

Figure 5: Initiation mechanism for "grafting-from" of functional monomers on membrane polymers through formation of starter radicals during surface functionalization; (a) controlled degradation of the membrane; (b) decomposition of an initiator; (c) adsorption of initiator on the surface [64].

It has also been observed that above 170°C cross linking is dominant, while chain scission is much more important at room temperature [79]. In cases, when the membrane polymer is not UV sensitive, other reactants are employed. Feasible mechanisms are the decomposition of an initiator in solution and radical transfer Figure 5(b)) and the adsorption of a photoinitiator on the surface Figure 5(c)). A primary covalent attachment of chemical groups can be also used and further activated. It should be mentioned that, the polymeric layer structure cannot be well controlled during "grafting from" modifications. Thus, to control the chain length and density of the grafted layer, living polymerisation techniques are often utilized [80, 81]. Moreover, the sieving properties of membranes can be additionally controlled by modification with "smart" (stimuli-responsive) polymers [82] or hydrogels [69]. On the whole, the excitation with UV irradiation has the great advantage that the wavelength can be adjusted selectively to the reaction to be initiated, and, hence, undesired side reactions can be avoided or at least reduced [64]. Photoinitiation can be used without problems also in small pores. Inadequate control of chain scission can lead to pore degradation and therefore, increase the membrane pore size which may not be completely

compensated by the synthesized hydrophilic layer. In this way, loss of performance of the modified membrane may be disadvantageous. Photo−initiated processes have their largest potential when surface−selective functionalizations of complex polymer structures are required with minimal degradation of the base polymer in view.

Modification with Hydrogels

As noted above, one of the most commonly used techniques for surface functionalization is the UV initiated “grafting-from” copolymerization method [83]. Several classes of monomers, such as acrylic acid and various acrylates or methacrylates having PEG, carboxyl, sulfopropyl, dimethylaminoethyl or trimethylammoniumethyl side groups have been tested for functionalization of hydrophobic membranes, and the resulting membrane hydrophilicity, surface charge and the consequences for membrane performance have been studied [67, 68, 74, 84, 85]. The most studied modifier is poly(ethylene glycol) (PEG), which is a charge-neutral polymer that can interact with water via hydrogen bonds creating an energetic barrier to the adsorption of biomolecules at the membrane surface [86]. The reason why PEGs are fouling resistant to proteins is their kosmotropic properties [87]. Hence, thin-film composite membranes with grafted antifouling layers made of such kosmotropic polymer hydrogels are very promising materials in membrane separations. When a hydrogel layer is applied on the membrane surface (and in the pore openings), the membrane surface is shielded from the foulants, so that they cannot reach the hydrophobic material and deposit. Functionalization of UF membranes with hydrogel layers by UV-photo initiated graft copolymerization have been performed for many applications such as enhanced nanofiltration performance [88], the improvement of various protein solutions and separation [68, 89, 90], the reduction of fouling and biofouling propensity for UF and RO membranes [16, 91, 92] and obtaining low-fouling membranes with acceptable flux for

sugarcane juice clarification [93]. Jimbo et al. [94] grafted amphoteric charge groups prepared by heterogeneous graft polymerization from aqueous solution containing acrylic acid and (N,N-dimethylamino)propyl acrylamide. An approach was proposed to characterize the amphoteric-charged pore surface by the pH-dependent ζ potential and as well its theoretical modeling.

In this work, PES membranes with a molecular weight cut-off (MWCO) of 300 kDa (PES300) are modified using UV-initiated graft copolymerization (grafting-from) of an amphoteric hydrogel layer consisting of N-[3-(dimethylamino)propyl]-acrylamide (DMAPAA) and 2-acrylamido-2-methyl-1-propanesulfonic acid (AMPS) (total monomer concentration of 150 mM) to obtain a composite membrane exhibiting an isoelectric point (IEP) at pH of 7 and a MWCO of about 100 kDa. The monomer ratios and the irradiation time were the necessary parameters needed for the corresponding changes in thin-film hydrogel amphoteric composite membranes. The hydrogel layer depending on the solvent composition will impact anti fouling effect during filtration. Such composite amphoteric membrane would be useful in wide range of separation problems (e.g. in colloidal dispersion of nanoparticles and proteins) by manipulating solution parameters and the grafted hydrogel functional groups. Tailored characterization such as surface charge density via zeta-potential measurement and cut-off determination via dextran filtration/rejection, water permeability, surface hydrophilicity/hydrophobicity via contact angle measurement, surface morphology investigation via scanning electron microscopy (SEM) were carried out. The fractionation and the purification performance of the grafted membranes was investigated for fouling resistance during ultrafiltration and diafiltration of dispersions/solutions containing nanoparticles (silica nanoparticles as model) and/or proteins (bovine serum albumin as model) and hence to achieve maximum separation selectivity and throughput.

2.2 Nanoparticles

Nanoparticles (NPs) are particles with at least one dimension smaller than 1 micron and potentially as small as atomic and molecular length scales (~0.2 nm). NPs can have amorphous or crystalline form and their surfaces can act as carriers for liquid droplets or gases [95]. To some degree, nanoparticulate matter should be considered a distinct state of matter, in addition to the solid, liquid, gaseous, and plasma states, due to its distinct properties (large surface area and quantum size effects). Examples of materials in crystalline nanoparticle form are fullerenes and carbon nanotubes, while traditional crystalline solid forms are graphite and diamond. Many authors limit the size of nanomaterials to 50 nm [96] or 100 nm [97], the choice of this upper limit being justified by the fact that some physical properties of nanoparticles approach those of bulk when their size reaches these values. However, this size threshold varies with material type and cannot be the basis for such a classification. A legitimate definition extends this upper size limit to 1 micron, the sub-micron range being classified as nano [95]. It is important to highlights the two primary factors that cause nanomaterials to behave significantly different from bulk materials: surface effects (causing smooth properties scaling due to the fraction of atoms at the surface) and quantum effects (showing discontinuous behavior due to quantum confinement effects in materials with delocalized electrons) [98]. These factors affect the chemical reactivity of materials, as well as their mechanical, optical, electric, magnetic, and catalytic properties. The fraction of the atoms at the surface in nanoparticles is increased compared to microparticles or bulk. Compared to microparticles, nanoparticles have a very large surface area and high particle number per unit mass [95]. Nanoparticles structures are generally classified based on their dimensionality, morphology, composition, uniformity, and

agglomeration. Synthesized NPs are derived from different polymeric and metallic sources, including liposomes, micelles, dendrimers and in varieties of nanoassemblies [99].

The current and potential applications for nanoparticles are growing and cover an extremely broad range of markets and industries including biomedical and cancer treatment, renewable energy, environmental protection, pharmaceuticals, personal care, surface coatings, plastics, textiles, food, building materials, electronics and automotives etc.

Like other fields of nanotechnology, applications of nanoparticles offer much promise to improve and enrich our daily life. In fact, there are already a number of nanoparticle-based consumer products available on the market [100]. For example, personal care products containing TiO2 and ZnO nanoparticles are sold extensively to protect human skin from harsh UV rays. Silver nanoparticles are used as an antibacterial agent in many consumables ranging from surgical instruments to door knobs [101].

The established nanoparticles syntheses are categorized into two main approaches: top-down and bottom-up [102-104]. Top-down is characterized by reducing the dimension of the original size by utilizing special size reduction techniques (physical approach). Bottom-up or chemical approach involves a common route used to produce nanoparticles from atomic or molecular scale. Here, attention is focused on the nanoparticles used in this work. Two principally different process technologies are used for the manufacture of synthetic amorphous silica (SAS), namely the thermal route which leads to the formation of pyrogenic SAS and the wet route yielding precipitated SAS, SAS gel or solution (sols). SAS sols (colloidal SASs) are stable dispersions of SAS particles in a liquid, usually water. SAS sols are produced directly by hydrolysis of monomeric SiCl4, in aqueous solution followed by condensation of the initial SAS particles into a sol. Hydrolysis of tetraethoxysilane in an alkaline solution of water and alcohol leads to monodisperse SAS sols of exceptionally large particle sizes.

Alternatively, a dilute solution of water glass can be passed through a hydrogen exchange resin, where sodium is removed and polymerisation of monomeric SAS takes place. The particle size, size distribution and morphology is controlled through systematic monitoring of reaction parameters (e.g. avoiding excessive addition rates of the reactants). An indirect way of manufacturing SAS sols is by re-dispersion of existing silicas. In this case, SAS gels, precipitated SAS or, less commonly, pyrogenic SAS are re-dispersed by applying large shearing forces to these previously produced SASs. Finally, the SAS sol is filtered and concentrated to the desired level. Furthermore, SAS sols can also be spray dried.

The most important point in either sol manufacturing process is stabilization of the dispersed SAS sol particles. This is achieved by the addition of KOH, NaOH, NH3 or HCl. An alternative method for stabilization is based on electrostatic repulsion of the particles. By adding small amounts of other metal oxides like aluminium oxide the net charge of the particles in the solution is increased leading to higher repulsive forces between the sol particles.

The gold nanoparticle employed in this work was generated using laser ablation. Laser ablation is a physical process which involves the use of short pulses of laser energy focused on a target in a solvent [105]. The target absorbs the energy from the laser pulse and is vaporized. The vaporized material then condenses as nanoparticles. Laser ablation generates nanoparticle dispersions that are free of any contaminants, such as unreacted starting materials. Most importantly there is no use of chemical toxic stabilization agents. The released nanoparticles are stabilized by the surrounding medium against agglomeration and are readily suitable for further processing owing to the high purity of the generated gold nanoparticle colloids [106].

2.2.1 Interactions of Nanoparticle and stabilization

Derjaguin, Landau, Vervey, and Overbeek (DLVO) developed a theory of colloidal system stability, which currently represents the basic foundation to understanding the interactions between colloidal particles and their aggregation behavior. The theory was firstly formulated for two identical interfaces (symmetric system), which is analogous to the case of the aggregation of identical particles (homoaggregation). This model was later extended to the two different interfaces (asymmetric system) and aggregation of different particles (heteroaggregation). In the restricted case of large size disparity between the particles, this process corresponds to deposition of particles to a planar surfaces [107-109]

DLVO theory assumes that the free energy per unit area can be well estimated by two additive influences, as

$$W(h) = W_{vdW}(h) + W_{dl}(h) \qquad (2.8)$$

These two contributions refer to van der Waals and double layer interactions. Van der Waals forces are almost always present and the interaction can be modeled using the relationship in equation (2.8). Double layer interactions are important for charged substances, more especially at lower salt levels. The interaction free energy can be approximated by

$$W_{dl}(h) = \frac{2\sigma_+ \sigma_-}{\varepsilon_0 \varepsilon K} \exp(-Kh) \qquad (2.9)$$

Where σ_+ and σ_- are the surface charge densities per unit area of the right and left surface, ε_0 is the permittivity of vacuum, ε the dielectric constant of water, and K is the inverse Debye length. The latter is given in equation (2.11).

The dominating interparticle forces in most NP systems are the van der Waals, double layer (electrostatic), and steric (polymeric) forces, as shown in Figure 6.

The van der Waals or dispersion force is an electrodynamic interaction that arises as a consequence of the interactions between fluctuating or permanent dipoles between molecular and macroscopic bodies (i.e. nanoparticles in this context) in close proximity [110]. This Van der Waals force is typically active at an interparticulate distance <1 nm and rapidly falls off at >10 nm [111].

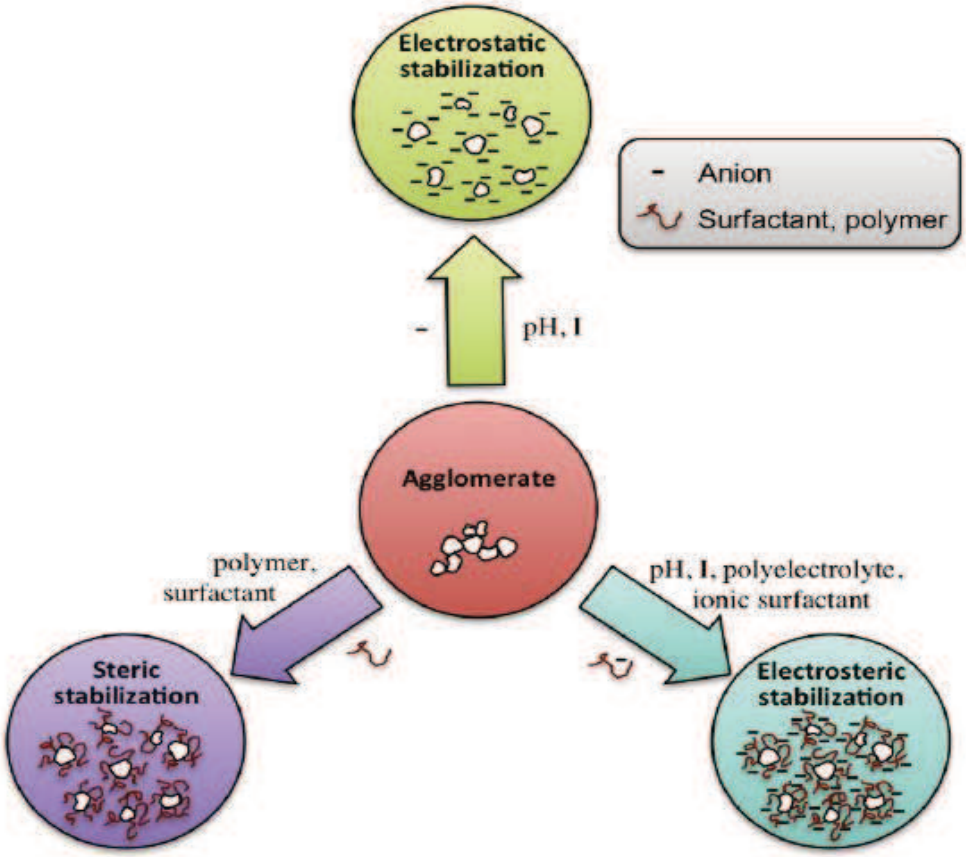

Figure 6: Schematic illustration of the main mechanisms for stabilization of nanoparticle dispersions [110].

The magnitude of the van der Waals (vdW) pair interaction energy, V_{vdW}, scales with the value of the Hamaker constant A [111], and decreases with the separation distance, s. The exact form of the distance scaling depends on the geometry of the interacting particles, the pair interaction for two spheres of radius r, is shown in equation (2.10).

$$V_{vdW} = -\frac{Ar}{12s} \tag{2.10}$$

The Hamaker constant is material dependent and increases with the contrast in dielectric properties between the particles and the solvent. It is possible to directly measure the van der Waals forces between inorganic particles using atomic force microscopy and also to estimate the magnitude of *A* from optical data using Lifshitz theory [112, 113].

Colloidal stable dispersions require that some type of interparticle repulsion is introduced to overcome the ever-present van der Waals attraction. In a stable system, the maximum attractive interparticle energy should be sufficiently small, in the order of $1 - 2k_BT$, to allow thermal motion or agitation to readily break all particle-particle bonds [114].

Electrical double layer interactions originate from the cumulation of counter ions near a charged surface. A net charge may build up on the surfaces of nanoparticles in liquids through various mechanisms such as the dissociation of surface groups, the specific adsorption or dissolution of ions, and the presence of crystalline defects [115]. The dissociation of surface hydroxyl groups is the main charging-up mechanism for metal oxide surfaces in water and depends on the pH. The pH at which the net surface charge is neutral is called the isoelectric point, and Colloidal dispersions of metal oxide particles can be stabilized by electrical double layer interactions, e.g., by adjusting the pH away from the pH value of the IEP.

The adsorption of charged molecules with a high affinity for the surface can also be used to increase the surface charge. The range of these interactions is defined by the Debye length and strongly decreases with increasing ionic strength:

$$K^{-1} = \left(\frac{\varepsilon_r \varepsilon_0 k_B T}{2N_A e^2 I^2}\right)^{\frac{1}{2}} \tag{2.11}$$

Where ε_r is the dielectric constant of the solvent, ε_0 the permittivity of vacuum, I is the ionic strength, e is the elementary charge, k_B the Boltzmann constant, T the temperature, N_A

Avogadro's number and e the elementary charge. A high concentration of free ions will screen the repulsive double layer interactions and decrease their range.

One may say that the surface potential of the particles determines the magnitude of the electrostatic repulsion [116], whereas the electrical double layer determines the distance from the surface where this repulsive force arises. Therefore, effective stabilization of a liquid dispersion is most readily obtained once the thickness of the electrical double layer $(1/k)$ exceeds the range where F_{VDW} starts to become active. Nanoparticles stabilization is usually discussed in terms of two general categories of stabilization, electrostatic and steric. Electrostatic stabilization is achieved by the coordination of anionic species, such as halides, carboxylates or polyoxoanions, to metal particles. This results in the formation of an electrical double layer (really a diffuse electrical multilayer), which causes coulombic repulsion between the nanoparticles.

In many nanoparticle systems, it is not possible to create a stable dispersion simply by controlling the pH. Hence, addition of suitable surfactants or polymeric dispersants is commonly used to provide a so-called polymer-induced or steric stabilization. Polymer-induced interactions arise when the adsorbed surfactants or polymers have segments or chains that protrude into the solvent and thus provide a protective adlayer on the nanoparticle surfaces. Several conditions should be fulfilled for efficient steric stabilization: the adsorbed layer should be thick enough to screen the attractive van der Waals interaction, the adsorbed molecules should be strongly adsorbed and cover the entire nanoparticle surface, the segments protruding into the solvent should be in so-called good solvent conditions [117]. Hence, the presence of bulky, typically organic materials (for example polymers and large cations such as alkylammonium) which due to their bulk, impede the nanoparticles from diffusing together [118] are examples of steric stabilizers.

Functionalization of Nanoparticles (FNPs): NPs either display novel nanoscale properties or when combined with other materials provide novel property or function. The main goal of functionalizing NPs is to envelop their surface with a molecule that possesses the appropriate chemical functionality for the desired application. Metal NPs are good vehicles for tracers and therapeutic agents and can be easily functionalized. In addition, some polymeric NPs are biocompatible and can serve as active targeting nanocarriers [119]. Biomolecules decorated on the surface of such nanoparticles can still show activity [120] with versatile applications in drug delivery, therapy, imaging and sensing. Nanoparticles can be functionalized using four major mechanisms: electrostatic adsorption, direct chemisorption of thiol derivatives, covalent binding through bifunctional linkers, and specific affinity interactions.

2.3 Techniques for purification and fractionation of nanoparticles

To explore the nanoscale distinctive effects and in the synthesis of nanostructured materials/devices with well-defined properties and functions, it is desirable to reduce the polydispersity of their nanoparticulate components. In several cases (e.g., using polymeric stabilizers, [121] reverse micelles, [122] or thermal decomposition methods [123]), low degree of polydispersity can be achieved during particle synthesis; in many others, however, the particles need to be purified after synthesis. In addition, for non-spherical particles (e.g., nanorods, prisms, or cubes [124-126]) solution based procedures yield target particles contaminated with differently shaped objects, including small spherical “seeds” and other competing particles. The methods discussed here are also being used for purification of nanoparticle dispersion and nanomaterial-biological hybrids systems.

2.3.1 Conventional methods

2.3.2 Separation of NPs by magnetic fields

Magnetic fields can separate NPs according to their magnetic susceptibilities and/or sizes. The magnetic force (F_M) which acts on a particle is given by equation 2.12.

$$F_M = \mu_O \chi V_P H \nabla H \qquad (2.12)$$

Where H is an external magnetic field, χ is the magnetic susceptibility, and V_P is particle's volume.

Yavuz et al. [127] described in details the potential and usefulness of magnetic separations under experimentally feasible conditions (fields < 1-2 T, field gradients < 100 T/m). These authors showed efficient separation of differently sized Fe_3O_4 NPs on a column packed with steel wool and subject to a tunable magnetic field. The influence of the field on the retention of separate batches of differently sized (4, 6, 9.1, 12, and 20 nm) nanocrystals was demonstrated by high gradient magnetic separation (HGMS) with higher fields required to retain smaller particles on the column (since $F_M \propto V_P$).

Different mechanism, based on the so-called capillary magnetic field flow fractionation (MFFF) and described by Latham et al., [128] demonstrates that magnetic NPs can be separated not only according to size but also to material composition.

2.3.3 Chromatography

In chromatographic separations, a mobile phase containing a mixture to be separated passes through a stationary phase. The separation is then based on the differences in the partition coefficients between mobile and stationary phases for all components of the mixture. While several examples of the use of HPLC for NP separation have been reported [129, 130], size exclusion chromatography (SEC), is probably the most popular chromatographic technique used to fractionate nanoparticles. SEC is based on the differences in the particles'

hydrodynamic volumes and not on the interaction of these particles with the stationary phase. Small particles meander freely through the pores around the stationary phase and thus travel through the column slowly. In contrast, large particles which do not fit inside the pores of the stationary phase, can travel only through the accessible volume (~30 % of total volume) and elute more rapidly [131]. SEC has been used in the separations of different types of nanoparticles, including gold, silica, and semiconductor ones [132-135].

2.3.4 Density gradient centrifugation

Centrifugation is one of the most important separation techniques used widely in colloid science and in cellular and molecular biology [136]. While objects denser than a liquid settle spontaneously due to gravity, this process can take very long; for very small particles (e.g., nanoparticles, nanotubes), where gravitational energy is commensurate with thermal energy, the particles will not settle at all. However, centrifugal forces can help particles to move radially away from the axis of rotation and can separate these particles by size and shape. In a centrifugal field, three main forces act on a particle: centrifugal force (Fc), buoyant force (Fb) and frictional force (Ff). The particle will be accelerated in a centrifugal field until the forces balance, $Fc + Fb = Ff$, and will afterwards sediment with a constant velocity $v = V(Pp-Pr)w^2r/f$.

The fact that particles of different sizes and/or shapes move with different velocities in the medium provides a basis for particle separation into distinct bands, though the quality of separation is poor if the particles are similar. To remedy this, more powerful techniques are needed. One such technique is the density gradient centrifugation, in which particles are centrifuged in a liquid column supporting a density gradient (such that the buoyant force varies within the tube). Density gradient can be created by careful layering of the different-concentration liquids on top of one another. As a result, density increases from the top to

the bottom of the tube. For example, Sun et al [137] used rate zonal centrifugation (RZC) to separate FeCo@C (FeCo nanoparticles coated in graphitic shells) and gold nanoparticles (Au NPs). Controlling the step gradient densities and centrifugation times, polydisperse FeCo@C NPs of a larger (on average, 7 nm) and smaller (on average, 4 nm) size ranges were separated.

The work of Sharma et al., [138] recently described the separation of AuNRs and AuNPs by centrifugation at 5600 g for 30 min. The results showed that spheres and cubes sediment at the bottom, segregating from rods that form a high-purity deposit on the side wall.

2.3.5 Electrophoresis

Electrophoretic techniques can separate charged objects in a uniform electric field. These methods are used widely in biological and biochemical research, protein chemistry, and pharmacology [139]. Charged molecules or particles migrate in an electric field toward the opposite-polarity electrode. Overall, particles having different charges, sizes, or shapes have different migration velocities and ultimately separate into distinct bands.

The most popular electrophoretic modalities are gel electrophoresis (GE), free flow electrophoresis (FFE), and isoelectric focusing (IEF) electrophoresis. In the familiar GE, [140] the particles migrate through a gel matrix (e.g., agarose or PAA-polyacrylamide). IEF electrophoresis is used extensively in biology to separate isoforms of proteins according to their isoelectric point (pI). These techniques have been recently applied in nanoscience. For example, Hanauer et al. [141] used GE to separate polymer-coated spherical, rod-shaped, and triangular gold and silver nanoparticles.

The IEF gel electrophoresis technique was used by Arnaud et al to narrow the size distribution of 1.7 ± 0.8 nm water soluble gold NPs stabilized by mercaptosuccinic acid [142].

2.3.6 Selective Precipitation

Size-selective precipitation (SSP) is a simple technique which allows for separating the NPs according to size-dependent physical and chemical properties, reactivity, and/or stability. Since these properties depend strongly on the surface chemistry of the NPs, SSP should be tailored to specific particle type/functionalization.

An illustrative example of SSP is the DNA-induced size-fractionation of gold nanoparticles developed by the Mirkin group [143]. These authors discovered that the so-called melting temperature, T_m - that is, temperature above which the hybridized DNA duplexes in DNA-linked NP clusters disassemble ("melt") causing sharp transition from an aggregated to a dispersed phase-increases with NP size. These observations allowed for the separation of binary and ternary mixtures of differently sized (15, 30, 40, 50, 60 and 80 nm) NPs into separate batches with purity above 90 %.

Oligonucleotides capping AuNPs were also used for NP separation by Zhao et al. [144]. It was reported that oligonucleotide-capped AuNPs undergo reversible salt-induced aggregation, and that the concentration of salt at which aggregation commences depends on NP sizes in particular, larger particles aggregate at lower salt concentration than the smaller particles.

Tao Xu et al. [145] applied tensions at Liquid Interfaces as a general filter for the Separation of Micro-/Nanoparticles (size selective precipitation through fractionation of Cu_2O NPs with diameter 2 µm and 400 nm (2,8 mL) was achieved by the addition of ethanol to n-pentanol (1:4 by volume) and centrifuging at 4000 rpm for 5 mins). In another development, Saunders et al. [146] size-selectively fractionated dodecanethiol-stabilized Au and Ag NPs using CO2-expanded hexane at an application scale (size precipitated by fine tuning the subtle balance between the van der Waals attractive forces and osmotic repulsive forces by varying an applied pressure of C02 above the - NPs dispersion).

2.3.7 Extraction

Extraction is a method to separate compounds based on their relative solubilities in two different, immiscible liquid phases, usually water and an organic solvent. This method has been used widely for separation and purification of organic and inorganic compounds. Recently, Wilson et al. [147] reported selective extraction of Au and Ag dendrimer-encapsulated NPs (DENs). The authors proposed that in this method, a selective separation was possible owing to the fact that *n*-alkanoic acids (here, *n*-decanoic acid) have higher affinity for chemisorption onto Ag than onto Au surface.

A different extraction method for reversible separation/concentration and dispersion of various NPs based on cloud point extraction (CPE) was proposed by Liu et al. [148].

It is well known that surface-active chemicals can assemble into colloidal-sized clusters called micelles. During their formation, these micelles can encapsulate various substances thus segregating them from the bulk solution. The solubility of non-ionic or zwitterionic surfactants in water phase is dramatically depressed above a well-defined temperature called cloud point temperature, CPT. Above CPT, a solution separates into a concentrated phase containing most of the surfactant (the surfactant-rich phase) and a dilute aqueous phase. CPE is based on the affinity of compounds/particles of interest toward the surfactant, this affinity then determines the extent of partitioning between the surfactant-rich and the surfactant-poor phases. In their work, Liu and co-workers extracted/concentrated several types of NPs (capping reagents listed in parentheses): Au NPs (trisodium citrate), Ag NPs (polyvinylpyrrolidone), C_{60} fullerene, TiO_2, Fe_3O_4 NPs (humic acid), CdSe/ZnS (polyethylene glycol), and SWCNTs (dispersed with sodium dodecylbenzene sulfonate). Triton X-114 sufactant (3.6 mM) and NaCl (3.4 mM) were added to the NP solution, which was then heated above the CPT (23-25 °C). Owing to the NP-micelle interactions, nanoparticles were

extracted from the aqueous suspension (10 mL) into the surfactant rich phase (0.1 mL). The samples were centrifuged, and the concentrated NPs were redispersed into the aqueous phase by cooling to a temperature below CPT.

2.4 State of the art for membrane separations applied to nanoparticle dispersions

Separation though a membrane is another alternative for the purification and size-fractionation of NPs dispersions and mixtures. In this class of methods, retention and elution of an analyte depend on the size of membrane pores.

2.4.1 Membrane separations (non – polymeric membranes)

Hai-Wei Lang et al. [149] fabricated a carbonaceous nanofiber membrane (CNF) for selective filtration and separation of nanoparticles of 5 nm and 25 nm Au nanoparticles using the CNF-50 membrane. Mekawy et al. [150] employed mesoporous silica hybrid membranes for precise size-exclusive separation of silver nanoparticles. In their work, Ag-NPs dispersed in toluene/methanol mixture were fractionated but only particles smaller than 4.5 nm are able to pass the membrane though high level of control over NPs morphology and size was achieved. Gaborski et al. [151] used a porous nanocrystalline silicon (pnc-Si) of 15 nm thin free-standing membrane material for successful separation of 10 from 15 nm Au.

2.4.2 Membrane separations (polymeric membranes)

Xie et al. [152] demonstrated that membrane separation technique was an efficient way to achieve fractionation of Fe_2O_3 nanoparticles. Fractionation was then realized by using cellulose acetate (CA) microfiltration (MF) membrane of 5 μm pore size. The permeate and the retentate were found to have a smaller size (36.7-39.8 nm) and a larger size (52.4-56.9 nm). Akthakul et al. [153] fractionated AuNPs using a thin polymeric membrane made of graft copolymer with hydrophobic poly(vinylidenefluoride) (PVDF) backbone and

hydrophilic poly(oxyethylene methacrylate) (POEM) side chains. When a toluene solution containing polydisperse, octanethiol-modified AuNPs was filtered through the PEO/PVDF matrix, particles larger than 3.8 nm were retained on the membrane, while smaller ones passed through it freely. As a result, the size distribution improved from 3 ± 1 nm in the initial sample to 2.2 ± 0.7 nm in the filtrate. E. Krieg et al. [154] synthesized a recyclable supramolecular membrane for size-selective separation of nanoparticles-allowing their application in the size-selective separation of both metal and semiconductor nanoparticles. A thin (12 μm) membrane is used for filtration (fractionation of Au NPs reveals a cut-off of 5 Nm), and a thicker (45 μm) membrane allows for size-selective chromatography in the sub-5 nm domain. Sweeney et al. [155] have demonstrated that membrane filtration is also a good method for the size-fractionation of water soluble nanoparticles. They performed separate experiments in which they purified small AuNPs, separated binary mixtures into corresponding fractions, and finally fractionated polydisperse samples into several fractions characterized by different mean diameters of the metal cores. In the same work, the authors have also shown that a sample containing polydisperse NPs could be fractionated with sequential filtrations through membranes characterized by different MWCO values.

Further reports have demonstrated that membrane filtration could be used as a purification process for removing excessive surfactants in formulating stable nanoparticle dispersions and also as size fractionation/purification technique for nanoparticle dispersions in water [153, 155-157]. Further studies have investigated the use of cross-flow MF, UF and diafiltration for the purification of nanoparticle suspensions [7, 155, 157-159]. Dalwadi et al. have compared diafiltration and tangential flow filtration and shown that it is possible to remove surplus surfactant to achieve stable nanoparticle dispersions [156]. Most recently, Zhao et al. have also demonstrated the use of stimuli-responsive membranes for the

separation of BSA and polystyrene nanoparticles [160]. In addition, macromolecule-formulated nanoparticles (PEGylated or drug loaded NP) had also been purified from surfactants (polyvinylalcohol, sodium cholate) using tangential flow filtration and diafiltration centrifugal device [161, 162]. While most of these studies where done with the purpose to improve non-uniform size distribution of NP, or to remove unwanted impurities from NP synthesis/production processes, there was a single work devoted to the purification of proteins from polymeric NP (cf. above), and no work has been done to purify biomolecules (e.g. BSA) from metal oxide nanoparticle dispersions.

3 Aim and concept

The aim of this work is to establish membrane-based methods for both fractionation and purification of nanoparticle dispersion. The study will show that UF membranes could be used to separate mixtures of metal oxide nanoparticles (or other similar colloids) from proteins based on size differences, and thus reveal membrane process as having wider scope because of its easy scalability to large volumes. The nanoparticle dispersion comprises a model mixture of silica nanoparticles and proteins (Bovine serum albumin and lysozyme). This approach will show a more detailed insight into precise size selective fractionation of nanoparticle/protein mixtures with compounds of similar size, such as the purification of unbounded peptides in the gold nanoparticles bioconjugate systems. The sieving properties of ultrafiltration membranes (RC, PES) were employed through careful selection of membrane pore size with membrane appropriate features. Manipulation of the model mixture (proteins solution chemistry and filtration conditions) during purification/separation to eliminate/reduce fouling was done.

In addition to the commercial membranes (RC and PES) used in this work, surface modification of PES 300 was carried out as alternative to operational stability problems associated with RC. Therefore, PES membranes and their modified PES 300 or hydrogel-functionalized PES 300 membrane (H_{gel}F-PES 300) derivatives are evaluated. Product loss during filtration should be reduced by impacting anti-fouling properties to the membrane surface and hence to achieve maximum separation selectivity and throughput.

The base membranes as well as the H_{gel}F-PES 300 membrane have been characterized with respect to water permeability, hydrophilicity, surface charge and solute rejection, and fouling studies etc., to maximize selectivity during separation. The model purification concept is shown in Figure 7.

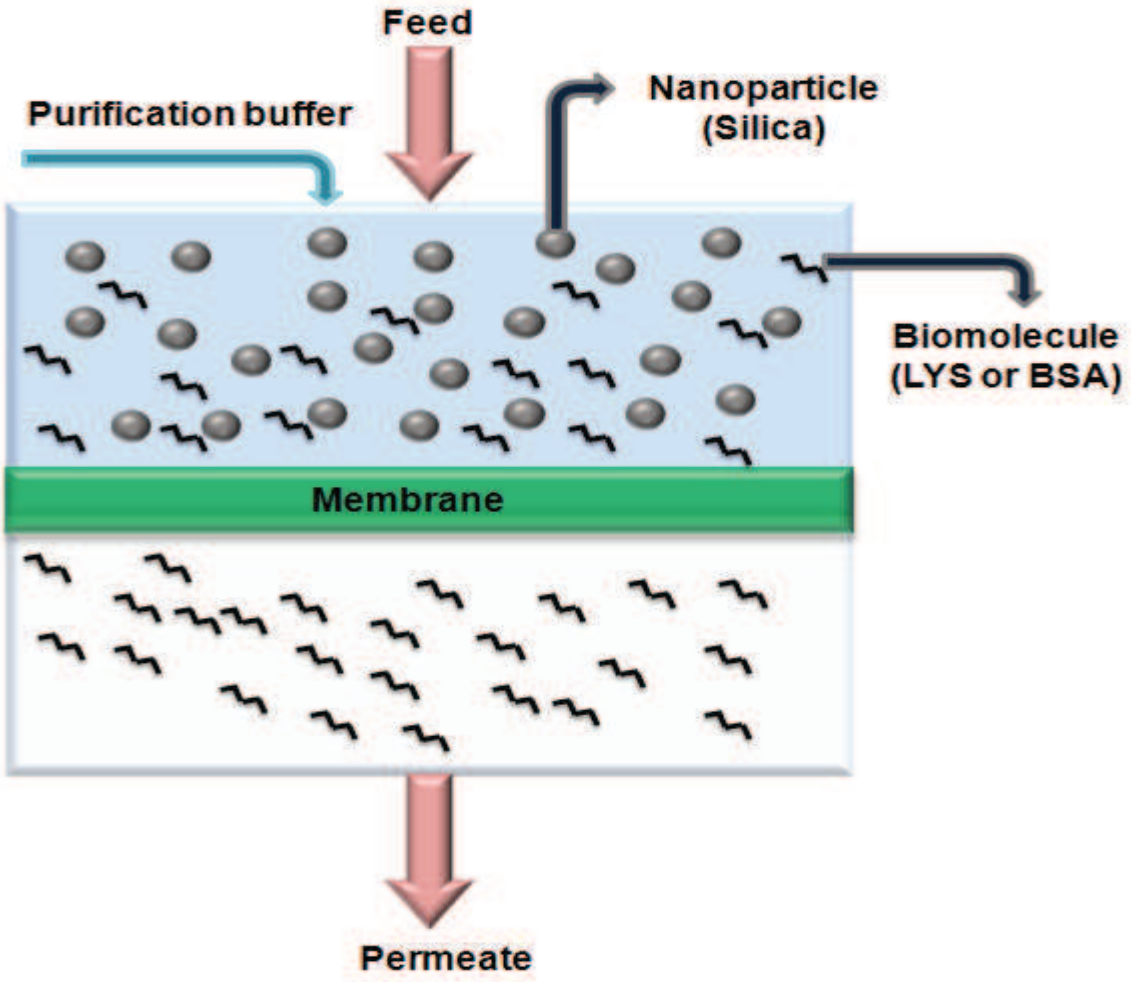

Figure 7: Schematic concept for the purification of metal oxide nanoparticle dispersion by removal of proteins through the membrane

Batch dead-end ultrafiltrations were used for fractionation and rejection measurements and continous or semi- continuous diafiltration processes were used for purification. The fractionation and purification efficiency were analyzed using analytical techniques such UV-Vis spectroscopy, atomic absorption spectrophotometry etc.

The result of the model solute study was applied to the purification of unbounded peptides in the Au-NP bioconjugate. The separation concept is also shown in Figure 8.

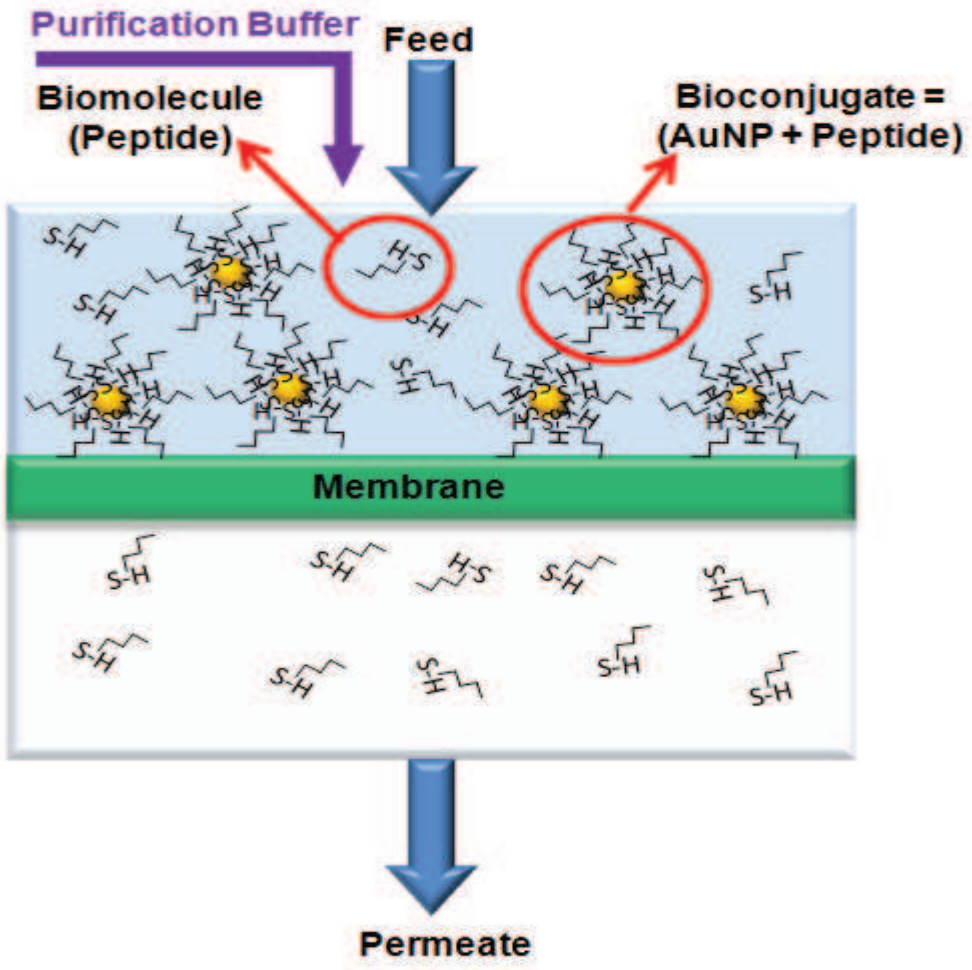

Figure 8: purification concept showing the use of ultrafiltration membranes to purify gold nanoparticle-biomolecule conjugates from unbound excess peptide ligands.

To achieve clear results, Au-NP produced from a model system based on a laser synthesis process (AK Barcikowski) possessing a ligand-free and bare gold surface which were subsequently bioconjugated with excess peptide was employed [163] and purified. To the best of our knowledge, this is the first systematic study to expand the use of polymeric UF membranes to the purification of bioconjugated noble metal nanoparticle dispersions by removal of unbound biological ligands. Subsequent comparison with standard centrifugal membrane filtration process shall give quantitative performance indicators for the AuNP-polypeptide model system purification method.

4 Experimental

4.1 Materials

Commercial RC and PES UF membranes with NMWCO of 30 and 100 kDa, donated by Sartorius-Stedim (Göttingen, Germany), were used for the filtration studies. In addition, a PES membrane from Sartorius-Stedim with NMWCO of 300 kDa was functionalized with a grafted amphoteric polymeric hydrogel and used for performance comparison. *N*-[3-(Dimethylamino)propyl]-acrylamide (DMAPAA) from Tokyo Chemical Industry Co., Ltd., Tokyo, Japan, and 2-acrylamido-2-methyl-1-propanesulfonic acid (AMPS) from Sigma-Aldrich Co., St. Louis, USA, were used as hydrogel monomers. Analytical reagent grade (99.99 %) ethanol (Fisher Scientific, UK) was used for washing of membranes before use. Sodium azide (NaN_3) used for membrane storage was purchased from Sigma-Aldrich. In order to determine the actual molecular weight cut-off, dextrans with molecular weights of 10, 40, 70 and 500 kDa were obtained from Pharmacia Fine Chemical AB, Uppsala, Sweden, while dextrans with molecular weights of 4 and 2000 kDa were procured from Serva Feinbiochemica GmbH & Co (Heidelberg, Germany) and Sigma-Aldrich, respectively. The chemicals used during zeta potential measurement include hydrochloric acid (HCl), potassium chloride (KCl) and potassium hydroxide (KOH), all from Bernd Kraft GmbH, Duisburg, Germany. Buffer chemicals purchased for this work include sodium hydroxide (NaOH) from Bernd Kraft GmbH, potassium dihydrogen phosphate (KH_2PO_4) from AppliChem GmbH, Darmstadt, Germany, and disodium hydrogen phosphate (sodium phosphate, dibasic, 99+ %, anhydrous, Na_2HPO_4) from Acros Organics, New Jersey, USA. The model proteins, BSA and LYS, were obtained from GERBU Biotechnik GmbH, Heidelberg, Germany, and Sigma-Aldrich, respectively. Ludox HS-50, the colloidal silica nanoparticles were purchased from Sigma-Aldrich Co. The gold (Au), peptide ($CE_{12}W$) and bioconjugated AuNP

used were supplied from the group of (AK Barcikowski). Milli-Q quality (≥ 18.2 MΩ·cm^{-1}) water, produced with a system from Millipore, USA, was used in all experiments.

4.2 Membrane pre-treatment

The membranes were cut in circular discs of required size with separation area of 4.16 cm^2. The samples were pre-treated with pure ethanol by placing them in a beaker and on a shaker for one hour, with 150 rpm at room temperature. This was done to remove impurities left from the manufacturing process or additives used for stabilization. Thereafter, the membranes were rinsed three times and washed overnight with Milli-Q water and stored in aqueous 0.01 M NaN_3 before use. Freshly pre-treated membranes were used in all experiments unless indicated otherwise.

4.3 Membrane modification by photografting

Following the same pre-treatment as outlined above (cf. 4.2), PES 300 kDa membranes were photo-grafted using the UVACUBE 2000 (Dr. Hönle AG, Gräfelfing, Germany) equipped with a high-pressure mercury lamp as source of radiation emitting wavelengths above 300 nm. To control the modification, the UV radiation was filtered through 2 green glass plates of 3 mm thickness and a special glass filter adjusting the wavelength to a range between 315 and 400 nm. The procedures have already been described in detail [16]. At first, a screening experiment was done to determine reaction conditions (irradiation time) to obtain desired membrane characteristics. In a second step larger batches of suitable membrane modifications are reproduced. Briefly the optimized conditions had a total monomer concentration of 150 mM in water with DMAPAA and AMPS in 1/1 molar ratio. Circular samples of PES 300 base membrane (diameter 25 mm) were immersed with the active layer side down into 2 mL of monomer solution in a Petri dish and soaked for 5 minutes. Next, they were turned active side up and covered with another smaller Petri dish so that the

surface was completely wetted with monomer solution. Three Petri dishes with different samples were placed at the same time in the UV irradiation chamber with above described glass filters on top of the membranes to eliminate UVB and UVC radiation impact. The effective irradiation intensity on the membrane surface, measured with the UVA sensor (Dr. Hönle AG), was 14 mW/cm², and the UV irradiation time used was 45 minutes. The grafting schematic is shown in Figure 9.

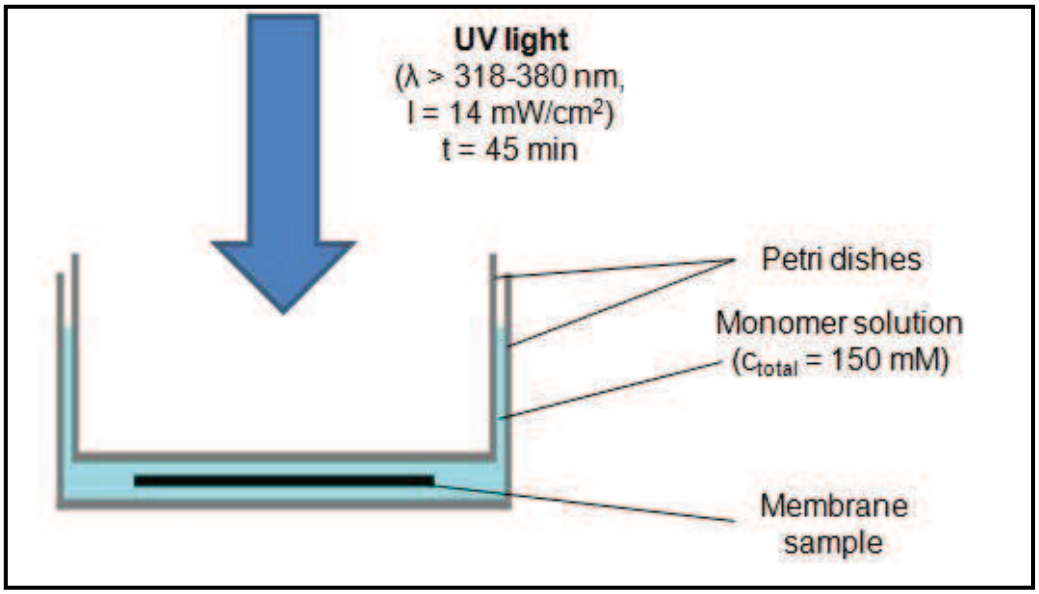

Figure 9: Schematics of the UV-initiated "grafting-from" functionalization of the membranes.

After UV irradiation, the membranes were rinsed and washed in excess of Milli-Q water for 24 hours at room temperature in order to remove residual non-reacted monomer and physically adsorbed polymer chains. The functionalized membranes were stored, as all other membranes, in aqueous 0.01 M NaN_3 solution. The degree of grafting (DG) is calculated using Equation (4.13).

$$DG = (m_{gr} - m_0)/A \qquad (4.13)$$

Where m_0 is the initial membrane sample weight, m_{gr} the membrane weight after modification and drying, and A is the outer surface area of the membrane used. All membranes used for DG determination were not used for further experiments because the

drying could have additional impact on barrier properties. The base membranes and monomers and their chemical structures used in this work are shown in Table 2.

Table 2: Base membrane polymers and monomers used in this work with their chemical structures.

Material	Abbreviation	Structural formula
Polyethersulfone	PES	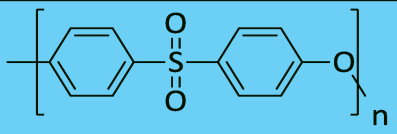
Regenerated cellulose	RC	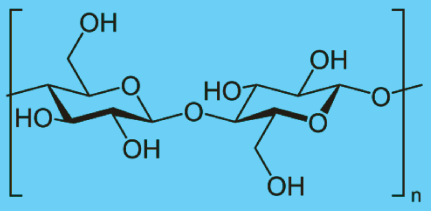
N-[3-(Dimethylamino)propyl]-acrylamide	DMAPAA	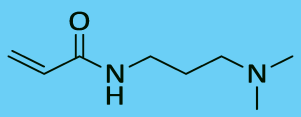
2-Acrylamido-2-methyl-1-propanesulfonic acid	AMPS	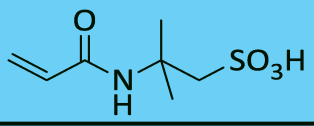

In the photografting, the acidic and basic groups (AMPS and DMAPAA, respectively) were used to form an amphoteric polymer brush layer. DMAPAA carries an amino group (pK_a ~ 9.6) that is protonated at moderate to low pH values. AMPS adds a negative charge to the polymer layer at moderate to high pH values because of dissociation of its sulfonic acid group (pK_a of about 0 to 2 [164]). The proposed mechanism of photo-initiation and first step of radical polymerization [77, 78] is shown in Figure 10.

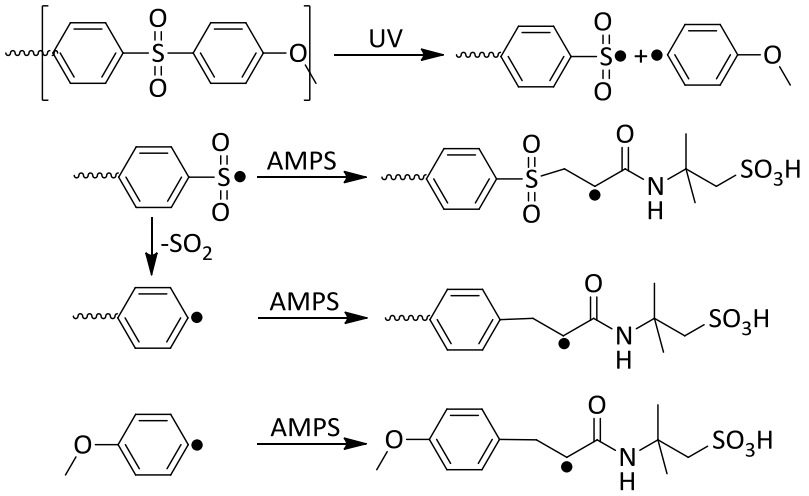

Figure 10: Proposed mechanism for photo-initiation and first step of radical polymerization

PES material represents a UV-sensitive polymer where initiator groups can be created by main chain scission through direct UV irradiation [78, 165]. The formed aryl and sulfonyl radicals react either directly or after elimination of sulfur dioxide with the vinyl group of an acrylamide monomer. The terminal radical enables the subsequent chain propagation whereby the two different monomers are both incorporated into the polymer chain (without distinct order). Since termination takes place rather often, the degree of grafting can be controlled by irradiation time. Moderate conditions ($\lambda > 300\,nm$) limit the change of morphology of the PES material through irradiation effectively [67].

4.3.1 Degree of swelling (of bulk hydrogel)

The degree of swelling of a bulk hydrogel is determined in different solutions with pH value of 8, adjusted by 20 mM PBS and varying NaCl concentration (0.0, 0.05, 0.1 and 0.2 mol/L). The prepared bulk hydrogel contains 16 wt % of monomer and the same monomer ratio ($n_{DMAPAA}/n_{AMPS} = 50/50$) as in the optimized conditions, but here polymerization is initiated by redox reaction instead of radiation and the hydrogel is cross-linked to stabilize the bulk phase. Table 3 shows the utilized concentrations of the hydrogel components.

Table 3: Bulk hydrogel component concentrations

Component	Concentration [mM]	Concentration [g/L]
DMAPAA	476.25	74.40
AMPS	422.68	87.00
MBAA	45.00	6.93
TEMED	120.00	13.94
APS	30.00	6.85

Crosslinker MBAA and accelerator TEMED are added to DMAPAA and AMPS being weighed in 25 mL Milli-Q water. To initiate the polymerization the radical starter APS is added at last, the solution is mixed well and put to rest for complete gelation. Then the hydrogel is washed for 8 days (until the amount of organic carbon washed out per day is less than 0.5 wt % of the net weight of synthesized hydrogel), cut into 10 similar pieces and equilibrated 7 days in the different buffer solutions, weighed in wet state, dried for 24 hours in vacuum oven at 40 °C and weighed again in dry state. The degree of swelling (DS) is calculated according to Equation 4.14 [166]

$$DS = \frac{m_{wet}}{m_{dry}} \tag{4.14}$$

where m_{wet} and m_{dry} are the masses of wet and dry gel, respectively.

4.3.2 Chemical resistance of modification

The stability of the modification, of the membrane material respectively, i.e. the chemical resistance to exposure to cleaning agent (i.e. caustic soda) is investigated by measuring both, the water permeability (cf. Section 4.7.1) and the gravimetric degree of grafting (cf. Section 4.3) before and after the exposure time. The experiment is carried out with PES 300 and PES 300_1/1_45 membranes. After determining the initial water permeability of a membrane

sample, it is dried for 2 hours at 40 °C in a vacuum oven ($p \leq 20\,mbar$, series VD from Binder GmbH, Tuttlingen, Germany). The mass of the membrane is measured with a semi-microbalance (type Genius ME215P from Sartorius AG, Göttingen, Germany) to calculate the gravimetric degree of grafting (cf. Eq. 4.13). Then the sample is exposed to 50 mL 0.1 M NaOH for a certain time (varying from 3 hours to 7 days). After exposure the membrane is washed in 100 mL Milli-Q water for 2 hours, the water permeability is determined, the membrane sample is dried and weighed as before. This procedure is repeated until a total exposure time to caustic soda of 7 days is achieved.

4.4 Membrane surface characterization

4.4.1 Membrane surface morphology

Scanning electron microscopy (SEM) with the instrument QUANTA 400 FEG from FEI Co. (Hillsboro, USA) was used to visualize outer membrane surfaces and cross-sections. All samples were sputtered with a gold/palladium layer using a K 550 sputter coater from Emitech Ltd. (Ashford, UK). The Au/Pd target consisted of 80 % Au and 20 % Pd. For cross-section analysis, the membrane were broken in liquid nitrogen and sputtered for 1.5 min, while for analysis of outer membrane surface, the sputtering time was limited to 0.5 min; obtained layer thicknesses were approximately 6 nm and 12 nm for surfaces and cross-sections, respectively. A beam of electrons is produced by an electron gun which generates and accelerates electrons to an energy range 0.1 - 30 kV. SEM imaging was done using 10 kV under high vacuum conditions and subsequent magnification of cross-sections and surfaces, respectively.

4.4.2 Membrane wettability

Contact angle (CA) measurement system (OCA 15 Plus; Dataphysics GmbH, Filderstadt, Germany) uses an optical subsystem to capture the profile of the air bubble on the

membrane. CA was measured by using the static captive bubble method. The sample holder with the fixed membranes was inverted in pure water at a temperature of 21 ± 1 °C. An air bubble (5-10 µL) was injected from a syringe with a stainless steel needle onto the sample surface water. The angle formed between the air/solid interface and the air/liquid interface was captured by a high resolution camera and the image was analyzed by computer. The camera magnification was set to 1.5 and the lamp brightness to 23. The contact angle was determined at minimum 6 different sites for each membrane sample and averaged accordingly.

4.4.3 Membrane surface charge

Membranes surface charge was characterized by streaming potential measurements using the SurPASS electrokinetic analyzer (Anton Paar GmbH, Graz, Austria) equipped with the so-called adjustable-gap cell with disk shape, having circular sample fitting of diameter 14 mm. The experimental set-up and procedures have already been described in detail [88, 167]. Briefly, two membrane samples were stuck to the sample holders (pistons) by double-faced adhesive tape and mounted into the adjustable-gap cell (membrane surface area of 1.54 cm^2). A flat-sheet tangential flow module set to a gap width of 100 ± 5 µm was used. The streaming potentials were measured as a function of pressure using 0.001 M KCl solution, in the range of pH of 2.5-11.5 through an integrated titration unit at room temperature. The zeta potential ζ was calculated using the Helmholtz-Smoluchowski equation (eq. (4.15).

$$\zeta = \frac{dI}{dp} \times \frac{\eta}{\mathcal{E} \times \mathcal{E}_o} \times \frac{L}{A} \qquad (4.15)$$

Where ζ is the zeta potential, I streaming current, p pressure difference across the sample, η viscosity of the electrolyte, $\mathcal{E}$ vacuum permittivity, $\mathcal{E}_o$ dielectric constant of the electrolyte solution, L length of the streaming channel, and A cross section of the streaming channel. Multiple samples were analyzed and averaged accordingly.

4.4.4 Membrane chemistry

Surface chemistry for the hydrogel-functionalized PES 300 membrane was determined using the instrument Varian 3100 Fourier transform infrared spectroscopy (FTIR) Excalibur series. A total of 64 scans were performed at a resolution of ± 4 cm^{-1} at room temperature. The Varian's resolution Pro 4.0 was used to record the modified membrane spectra versus the corresponding background spectra of the based membrane.

4.5 Colloid characterization

4.5.1 Colloid size determination via dynamic light scattering (DLS)

Sizes of BSA, LYS and silica in solution/dispersion were determined by dynamic DLS using the StabiSizer® PMX 200CS (Particle Metrix GmbH, Meerbusch, Germany) in particle size analysis mode. Freshly prepared solutions/dispersions containing 1 g/L in 20 mM PB at pH 8 for each colloid were measured. The particles were assumed to be transparent and of irregular shape. The refractive index values used were 1.33, 1.46 and 1.46 for the solvent (water or PB), the proteins (BSA or LYS), and silica, respectively [168, 169]. The dispersity is a measure of the heterogeneity of sizes of molecules or particles in a mixture. In light scattering, the term polydispersity is derived from the Polydispersity Index (PDI). The PDI is dimensionless and scaled such that values smaller than 0.05 are rarely seen other than with highly monodisperse standards. Values greater than 0.7 indicate that sample has a broad size distribution. Here the parameter was calculated from a Cumulants analysis of the DLS-measured intensity autocorrelation function. In the Cumulants analysis, polydispersity describes the width of the assumed Gaussian distribution.

4.5.2 TEM

Transmission electron microscopy (TEM) was used to analyze the silica. A drop of the silica dispersion was placed on a carbon-resin copper grid. The grid was then dried on a filter paper and analyzed by TEM on an EM 400 (Fa. Philips, Eindhoven) with an accelerating voltage of 120 kV.

4.5.3 Mixture Stability

For effective separation, it is very important that, the solute and most importantly the mixture solution maintain a stable dispersion throughout the filtration time. Therefore setting the pH below and above the solute IEP was use to optimize the most stable condition. Mixture dispersions contain BSA or LYS and silica-NPs. The visible turbidity and eventual precipitation are evaluated. BSA or LYS and silica-NP concentrations are 100 mg/L each in a 20 mM K-Na-phosphate buffer at pH of 4.9, 8.0 and 12.0 respectively. The solution is termed “stable” if there is neither visible turbidity nor precipitation.

4.6 Analyses (substances and model solutes)

Dextran: For GPC Analyses, a SUPREMA column (linear, 10 µm, 600/8 mm, size exclusion of 10^2 to 10^8 g/mol, from PSS Polymer Standards Service, Mainz, Germany) and RI-71 differential refractometer (Shodex Showa Denko K.K., Tokyo, Japan) as detector were used. Eluent was aqueous 0.01 M NaN_3 with a flow rate of 1 mL/min.

Silica nanoparticles: The fluorescence spectrophotometer Cary Eclipse (Varian Australia Ply Ltd, Mulgrave, Australia) was used to determine the silica concentration in single colloid experiment, based on a light scattering effect which is proportional to the silica fraction in the dispersion. The wavelengths for excitation and emission were 308 nm and 318 nm, respectively [170]. The excitation and emission slits were both set to 10 nm. A 4 mL cuvette

made of fused quartz was utilized and zeroed with the phosphate buffer. Calibrations in the range of 1 to 200 mg/L of silica showed a very good linearity ($R^2 \geq 0.99$).

To determine the silica concentration in presence of BSA or LYS, the atomic absorption spectrophotometer (AAS) 1100B (Perkin-Elmer & Co GmbH, Überlingen, Germany) with hollow-cathode lamp as radiation source was utilized. Mixture dispersions containing silica were atomized by a nitrous oxide/acetylene flame (6.5 L/min/6.0 L/min) and absorption was measured at a wavelength of 252 nm. Standards were prepared by serial dilution with Milli-Q water as diluents, yielding concentrations of 1, 5, 10, 20, 50, 100, and 200 mg/L silica. Colloidal silica can be detected quantitatively by this method in a range from 1 to 200 mg/L of Silica. The presence of BSA, LYS and/or K-Na-phosphate buffer (20 mM) did not have significant influence on the measurement.

BSA and LYS: To quantify the amounts of BSA or LYS after UF and as well as in the presence of silica, the test tube procedure of the Micro BCA™ Protein Assay Kit (Pierce Biotechnology, Rockford, USA) has been expanded for this purpose (concentration determination). The reaction was followed by absorbance at 562 nm using UV/vis spectrophotometer Cary 50 Probe (Varian Australian Ply Ltd, Mulgrave, Australia). A comparison of methods is given in Appendix 8.3, regarding their detection limit and accuracy.

UV-Vis spectroscopy*: The quantification of the amount of AuNP and peptide in the solution was done by UV-Vis absorbance measurements using an Evolution 201 (Thermo Scientific). For all measurements a quartz glass cuvette with a path length of 10 mm and a volume of 1.5 mL was used. In the case of peptide quantification, the absorbance at 278 nm is dependent only on the concentration.

* Quantification experiment had been perform by R. Streubel and coworkers (AK Barcikowski).

Hence, a calibration with a known amount of peptide was done. For the AuNP, the interband absorbance at 380 nm was used for the calibration. At this wavelength the absorbance of the colloid is linearly dependent only on the concentration of gold in the solution.

4.7 Membrane separation performance

4.7.1 Filtration studies

Flux and rejection experiments were performed in batch mode using a stirred cell resembling the ones widely employed in the study of flux and rejection by UF membranes. A typical UF filtration cell employed in this work is shown in Figure 11.

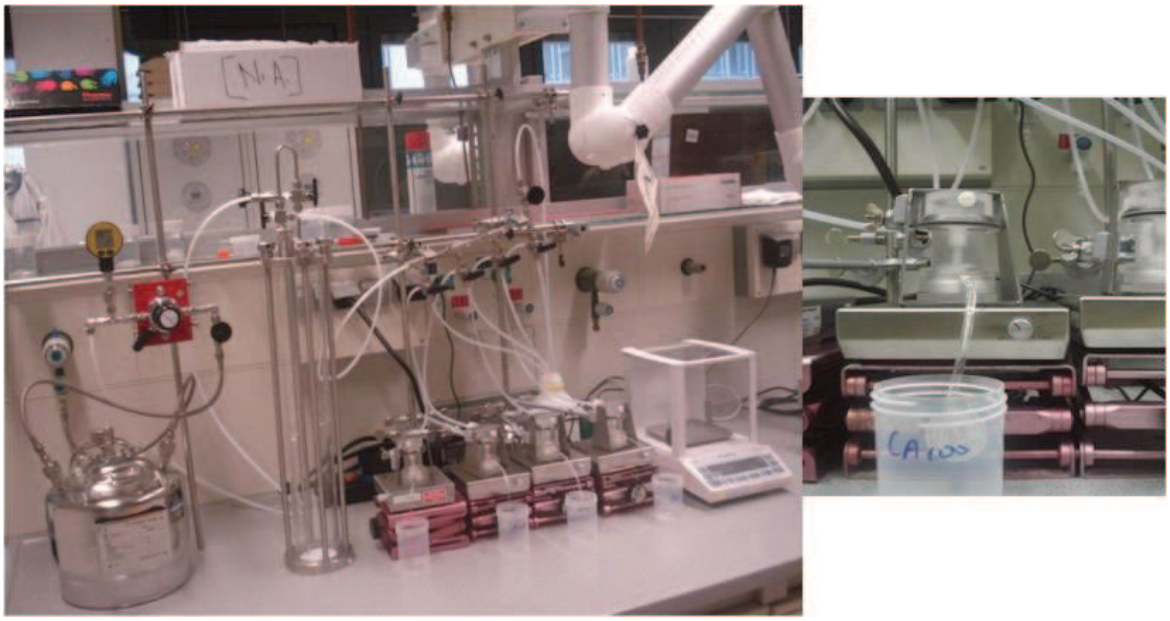

Figure 11: Overview of the in-house (designed and built) filtration setup

The in-house designed and built setup consists of up to four filtration cells in parallel. The filtration cell which can be used individually or simultaneously with the other ones is connected to a feed reservoir (~ 400 mL). During preliminary experiment, the set-up was used for membrane screening and selection. This is to ensure that samples with less variable water permeabilities (less than 5 %) are chosen for further experiments. In all experiments, representative results from minimum of three samples are analyzed and discussed. The

working pressure is provided by a high-pressure tank filled with nitrogen, with a gas pressure regulator. The tests were conducted at room temperature (21 ± 1 °C). Membrane pre-treatment has been earlier described (cf. Section 4.2). The membranes were first characterized by water permeability measurements. Prior to the measurement, the membrane was conditioned by filtering ultra-pure water at high pressure (mostly 4.5 bar) for at least 30 minutes. During this process, loss of flux was found over time due to the change in the membrane structure as a consequence of the applied pressure (compacting). Compaction was not done before solute rejection experiments because the membranes decompact when the pressure is relieved more rapidly with RC membranes. The water permeability measurements were done under DE stirring conditions at room temperature using the set-up shown in Figure 11. Water was pressurized with nitrogen and filtered through the membrane under stirring condition (300 rpm); the mass of permeate collected for 3 minutes was measured using a balance and the permeability was calculated according to Equation 4.16.

$$Permeability\ (L_P) = \frac{m}{\rho\ t\ A\ P}\ ,\ \left[\frac{L}{h\ m^2 bar}\right] \qquad (4.16)$$

m is the mass of permeate with density ρ collected for time t through membrane surface A at pressure P. Only membranes with flux deviation within 15 % were used for further characterization.

The other ultrafiltration studies were carried out in a stepwise process. The experiments involving single solutes (BSA, LYS and silica; 0.2 g/L), were performed at pH 8 and pH 12, respectively. Water flux measurements were carried out first, followed by the solute filtration until a certain amount of permeate was collected, after which water was again filtered to determine flux recovery (FR). The flux recovery and flux loss (FL) were calculated according to equations (4.17) and (4.18), respectively:

$$Flux\ recovery = \frac{J_f}{J_0} \tag{4.17}$$

$$Flux\ loss = \frac{J_0 - J_f}{J_0} \tag{4.18}$$

Where J_0 and J_f are initial and final water fluxes. For the calculation of observed rejection of single solute, equation (4.19) was used for the estimation.

$$Rejection = 1 - \frac{C_P}{C_R} \tag{4.19}$$

Where observed permeate and retentate concentrations are denoted C_P and C_R, respectively. In addition, membrane fractionation performance was tested with PES 300 kDa using silica nanoparticles (total mixture concentration of 0.2 g/L at pH 8) with sizes of 12 and 20 nm (supplier data) respectively and feed, permeate and rententate were analyzed (Zetasizer Nano, Malvern, UK) and the result shown in appendix 8.3 (A.5).

4.7.2 Critical flux determination

The critical flux (CF) was determined by measuring fluxes at different pressures. Selected experiments using 1 g/L BSA and mixture BSA/silica in buffer at pH 8 were performed. Fluxes were measured at pressure steps of 0.25 bar ranging from 0.1 to 3.0 bar, for 3 minutes each. The deviation from linearity of the flux vs. pressure curve was estimated to yield CF. The weak form of CF, found in this work, has been reviewed in detail [42]. The water flux (J_w) of the membranes was calculated using equation (3):

$$J_w = \frac{m}{\rho \times A \times t} \tag{4.20}$$

Where m is the weight of the collected permeate, ρ is the density of water, A is the membrane area and t is the time interval.

4.7.3 Adsorption experiments

For static adsorption experiments, a solution of BSA (1 g/L) was added to the cell containing the membrane sample. Thereafter, the active layer surface of the UF membranes was exposed for 1 hour without any flux at a stirring rate of 300 rpm. Then the test solution was removed and the membrane surface was rinsed two times by filling the cell with pure water (5 mL) and shaking for 1 minute. Water fluxes were measured before and after exposure to determine flux loss according to eq. (4.20).

4.7.4 Estimation of molecular weight cut-off

Molecular weight cut-off (MWCO) of the different membranes was determined by ultrafiltration of dextran mixture solutions in combination with gel permeation chromatography (GPC; see Section 4.6). Different dextran fractions (4, 10, 40, 70, 500 and 2000 kDa) were used and their corresponding feed concentrations (1.22, 0.54, 0.74, 0.34, 0.27 and 3.65 g/L) were prepared [171]. This dextran solution with total concentration of 1 g/L was ultrafiltered using stirred dead-end filtration cell with a membrane area of 4.16 cm^2. The filtration was performed at low flux (50 L/m^2h) condition at room temperature until 2 mL of permeate were collected from a starting feed volume of 10 mL. The permeate, retentate and feed were subsequently analyzed using GPC. The MWCO was directly analyzed using the obtained sieving curve at 90 % rejection for each molar mass according to equation 4.21.

$$S(M) = 1 - \frac{2\,C_P}{C_F + C_R} \tag{4.21}$$

Where C_F, C_P and C_R denote concentrations of feed, permeate and retentate solutions respectively.

4.7.5 Gold peptide filtration

The same procedure for model solute was followed during gold-peptide ultrafiltration (cf. 4.2.1). The concentration contains 10 mL solution, with 40 mM sodium phosphate buffer containing 20 µg/mL AuNP and 20 µM $CE_{12}W$. To purify the bio-conjugated gold nanoparticle-peptide solution from unbound free peptides, semi-continuous diafiltration was employed. The bioconjugate solution was purified by using dialysis buffer solutions with the same pH 8 and concentration. The starting solution volume was always 10 mL. After permeation of 5 mL, the permeated volume was refilled with washing buffer. One diafiltration volume (DV) was reached when the permeated volume equalled the starting volume (cf. 4.7.6). The diafiltration processes was continued to 3-6 DV, and permeate and retentate samples were subsequently analysed using UV- Vis spectroscopy (cf. Section 4.6).

4.7.6 Diafiltration experiments

For the mixtures (BSA/silica or LYS/silica), the same filtration steps as in single solute filtration (cf. 4.7.1) were performed but with total concentration of 0.4 g/L in 1:1 mass ratio. Similar fractionation steps were followed during gold peptide filtration (cf. Section 4.7.5). The number of diavolumes (DV) was determined according to equation (4.22)

$$\%\, Biomolecule\ removed\ = 1 - \ [\exp(DV\ \times T)^{-1}] \qquad (4.22)$$

Where DV, is the number of diafiltration volumes, and T is transmission$(1 - Rejection)$.

The purification using diafiltration was conducted in a continuous process. For example for the mixture (BSA/silica), the amount of feed to be purified, 10 mL containing 0.4 g/L of the mixture, was continuously washed with a known volume of K-Na-phosphate buffer at a constant flux. 1 DV is gravimetrically recorded, i.e. when the permeate volume reaches 10 mL. The feed, permeates and retentate samples were subsequently analysed using the methods described in Section 4.6.

5 Result and discussions

The experimental results and discussions are classified into four following parts:

(i) Membrane functionalization and characterization (sections 5.1, 5.2 and 5.3);

(ii) Properties of model colloids, mixture stability, analysis of model solutes (concentration determination), static adsorption of colloids (section 5.4 – 5.7);

(iii) Flux/pressure influence on model solute ultrafiltration (section 5.8); and

(iv) Rejection studies/evaluation of base and modified membranes separation performance, purification by diafiltration with model mixtures and gold-peptide bionanoconjugates (section 5.9 – 5.13).

5.1 Membrane surface functionalization

Here, results obtained from surface modification of PES UF membrane by photograft copolymerization are presented. The PES 300 was modified to confer hydrophilicity to the PES surface. The membrane modification via photo-initiated grafting-from co-polymerization is well controlled by altering irradiation time and/or monomer ratio. Irradiation time of 45 min and monomer ratio of 50/50 along with the effective irradiation intensity of 14 mW/cm² gave the required grafted amphoteric hydrogel layer of the modified PES membrane. Higher irradiation time yielded thicker grafted layer that gave no flux. However, variations in monomer ratios (53/47) only resulted in shift in IEP absolute values as shown in Figure 12. It is also, hypothesized that higher portions of DMAPAA possessing a basic functional group shift the IEP to higher pH values whereas AMPS that possesses an acidic group lowers the IEP. In the monomer ratio (50/50), the desired IEP and surface charge distribution and cut-off can be adjusted in a single modification step. The modification properties are well reproducible taking into account the fundamental variations of underlying commercial, base membrane properties.

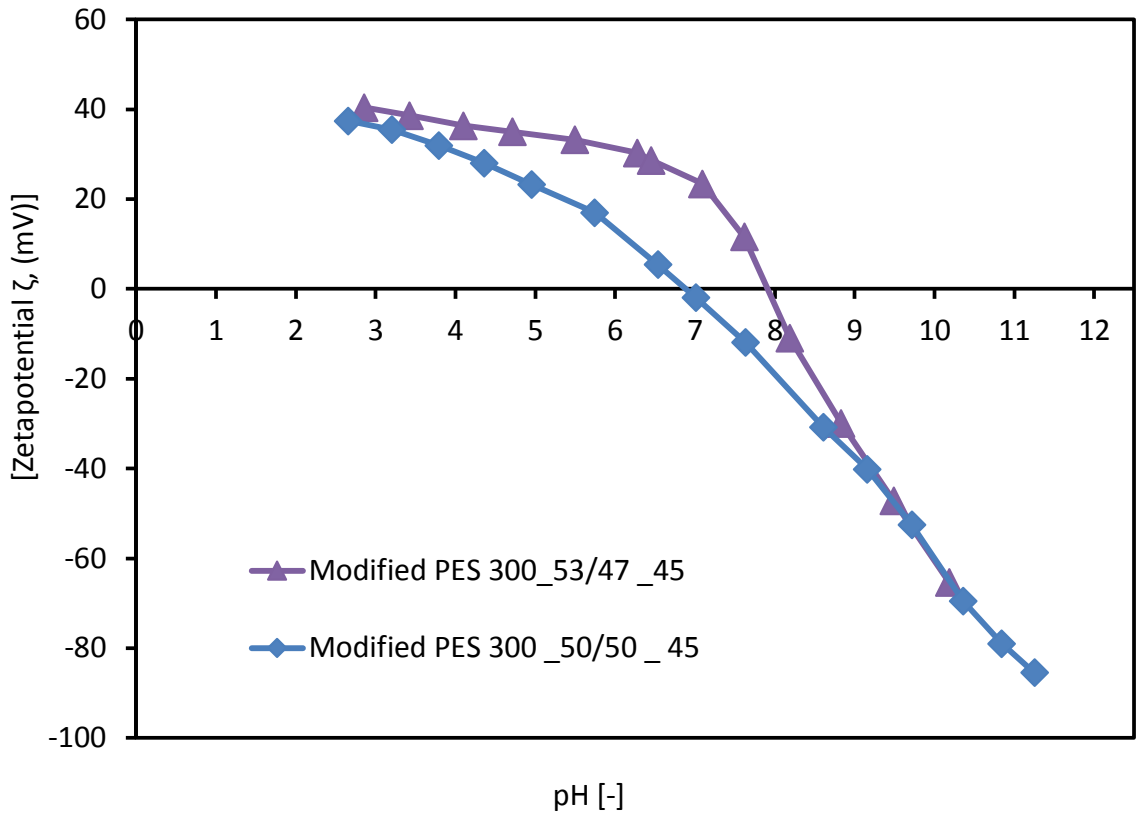

Figure 12: Zeta potential representation of the optimized modified PES 300 membrane obtained with a monomer ratio of 50/50.

The degree of grafting was used to quantify the amount of grafted polymer on PES membrane. The degree of grafting after UV-initiated functionalization according to previously optimized conditions (cf. also Section 4.3) was 305 ± 60 µg/cm^2. The thus H_{gel}F-PES 300 membrane showed reduced permeability. For example, at a transmembrane pressure of 0.3 bar, 90 % reduction in pure water permeability were measured compared to the unmodified membrane. Water flux generally represents the best flux that can be obtained with a membrane to monitor morphological changes within membrane pore/barrier surfaces. The loss of membrane permeability is linked to the blockage of membrane pores by the grafted polymer hydrogel. The PES water flux vs. pressure profile in comparison with the H_{gel}F-PES 300 is shown in Figure 13. The water flux (cf. Figure 13) for the H_{gel}F-PES 300 was much lower than unmodified PES 300. Importantly, the water permeability of the hydrogel composite membrane was similar to that for the membrane

PES 100. The relative deviation reflected as error bars (cf. Figure 13) are insignificant, they are less than 0.2% and within the range of experimental errors. One reason for this is that membranes of similar permeability are always selected for investigation.

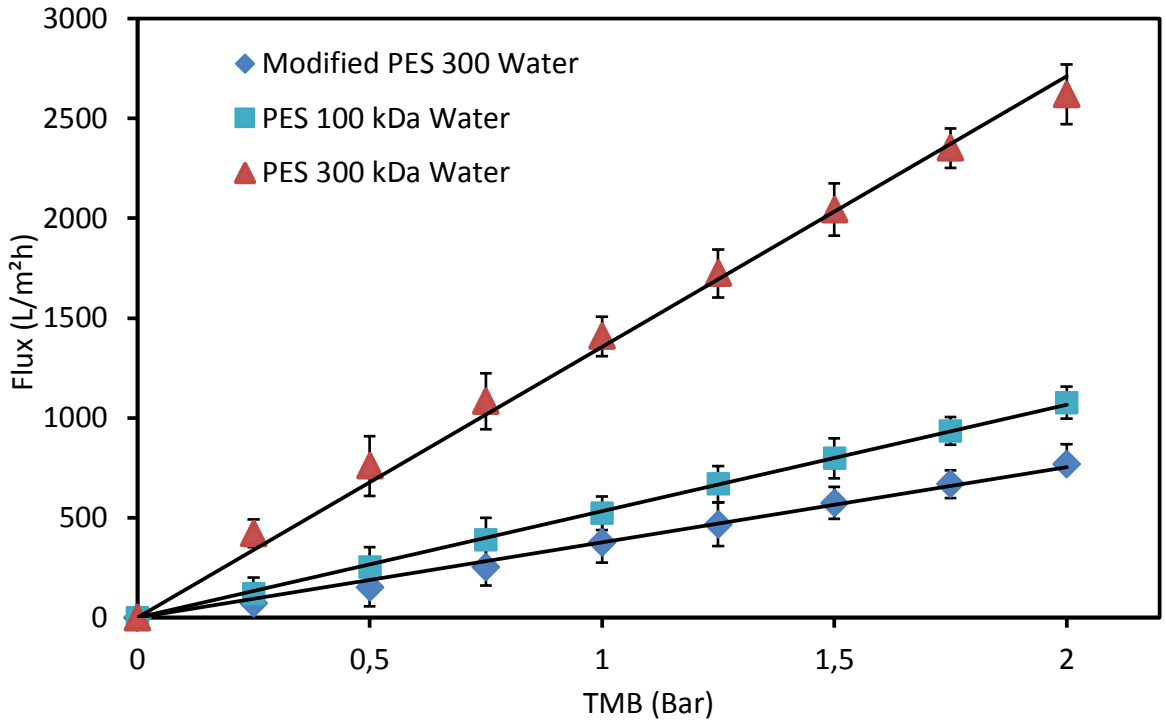

Figure 13: Relationship between applied transmembrane pressure and water flux for the PES membranes with the hydrogel-functionalized 300 kDa membrane.

In addition to the earlier mentioned reason, the grafted amphoteric hydrogel layer may foster increased hydrogen bonding between polymer chains in the grafted layer, which effectively reduces the availability of H-bonding sites for water-polymer interactions. Unless these interchain bonds are broken, the reduction in water-polymer H–bonding interactions might decrease water permeation through the membrane. This might be connected to the excessive loss of water flux for the grafted PES membrane.

5.2 Membrane characterization

It is fundamentally agreed that the performance of a UF membrane is very much influenced by its characteristics. Hence, it is important to know the characteristics of used membranes in this study. The membranes were characterized in terms SEM for morphology/porosity, membrane chemistry, contact angle to gain insight into hydrophilic and hydrophobic nature of the membranes and surface charge by zeta potentials.

5.2.1 SEM

SEM analysis of outer surface and cross-section of modified membranes was performed as supporting characterization in order to visualize changes caused by the applied UV irradiation and the grafted hydrogel layer. The SEM images of the base and hydrogel-functionalized PES 300 membrane are shown in Figure 14. The membranes exhibited an anisotropic structure with a dense top (“skin”) layer, a porous sub layer and sponge-like architecture at the bottom of both base and modified PES membranes Figure 14, image B, revealed a reduced surface porosity as compared to Figure 14 image A, obviously due to the grafted polymer. It should be noted that the grafted hydrogel layer is in a collapsed state during the SEM measurement. Thus, the observed smaller fraction of open pores on the surface clearly supports the reduction in hydraulic permeability. However, there are no significant changes between Figure 14, images C and D, which confirms that the overall pore morphology had been preserved and only a thin grafted hydrogel layer had been introduced in the barrier layer region of the membrane [172].

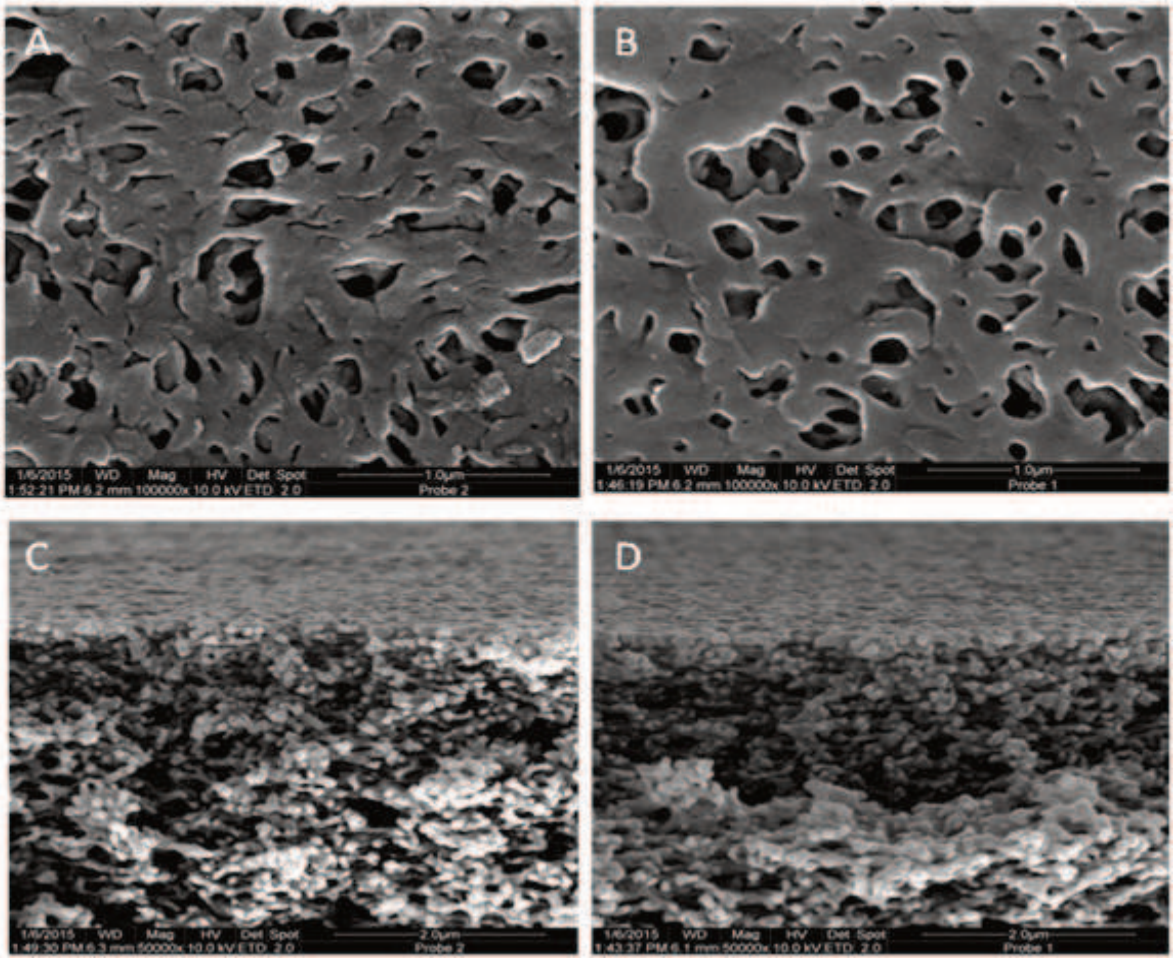

Figure 14: SEM images for outer surface (upper part) and cross-section of barrier layer (lower part) of membrane PES 300 kDa: A, C - unmodified, B, D - after functionalization with grafted hydrogel layer.

The pore structure from SEM analyses of the other membrane types is disclosed in Figure 15 and Figure 16. Membrane PES 100 possesses an analogous anisotropic property compared to PES 300 and larger surface pores in comparison to RC 100. The RC membrane also has anisotropic structure with a non-woven support and a more regular developed spongy morphology (cf. Figure 15)

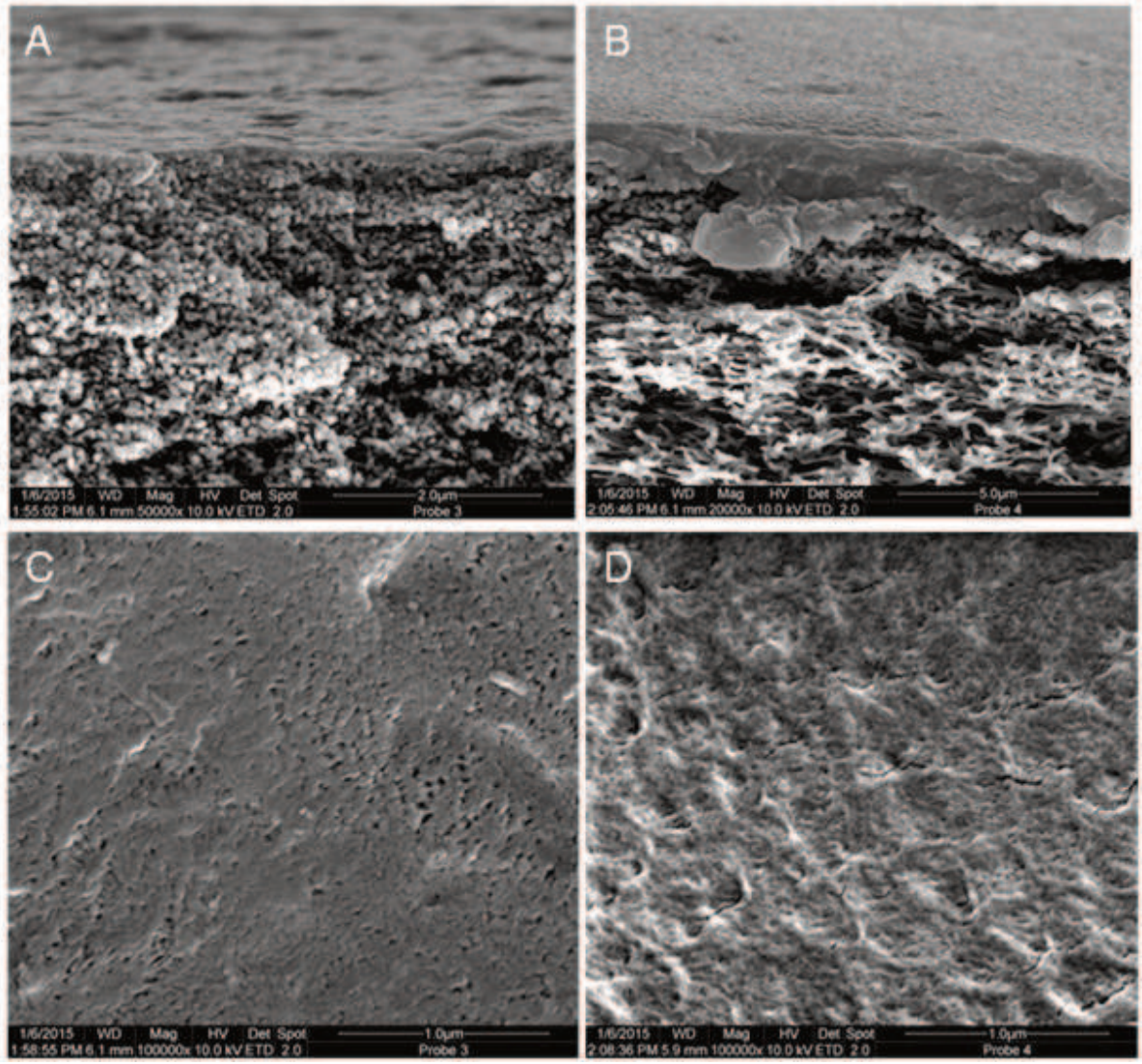

Figure 15: SEM pictures of cross-section of PES 100 kDa and RC 100 kDa (A and B) and outer surface of PES and RC (C and D), respectively.

In Figure 16, only the cross-section is shown for RC 30 and PES 30 kDa as the surface pores was not technically visible with SEM. However the PES 30 kDa reveal finger like structure which is clearly seen in Figure 16 image C. The finger-type structure can be the result of faster precipitation rate during membrane formation. Hence, membrane with similar chemistry can have sometimes different macro architecture.

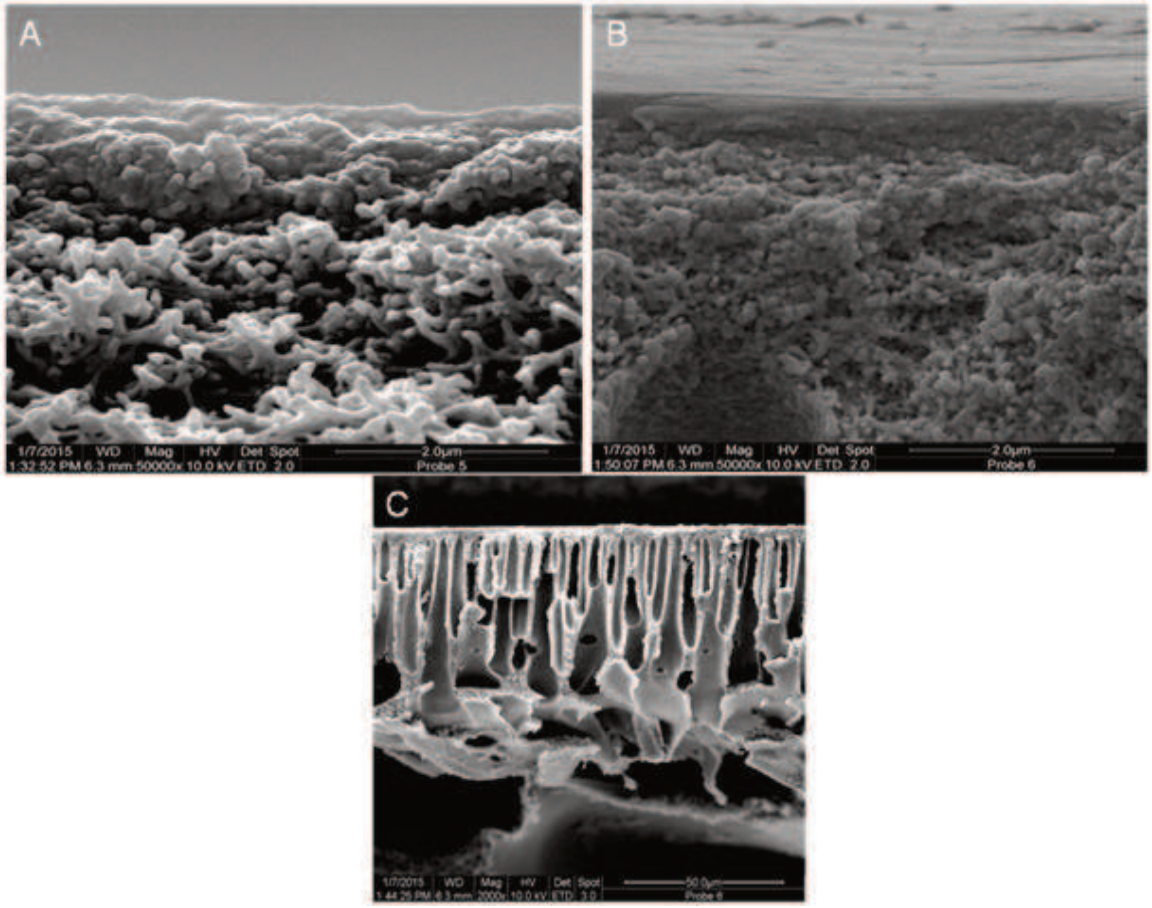

Figure 16: A and B are the cross-sections of RC and PES 30 kDa, C represents a cross-section of same PES 30 kDa membrane

5.2.2 Membrane chemistry

The FTIR analysis (see Figure 17) was done to elucidate the surface chemistry of the modified PES 300 membrane. As anticipated, all membranes showed typical spectra of PES, with bands at 1575 and 1480 cm^{-1} for C=C in benzene and band around 1240 cm^{-1} for aromatic ether. However, the IR spectra data confirmed also the band at 1040 cm^{-1} for sulfonic group as one characteristic peak for the grafted polymer [173, 174]. Although the tertiary amine group could not be identified in the IR spectra, energy dispersive x-ray spectroscopy (EDX) measurements in combination with SEM experiment revealed the presence of nitrogen in the grafted amine group of the polymer hydrogel on the outer membrane surface in small but significant fraction while no nitrogen could be found for the unmodified membrane (see Figure 18).

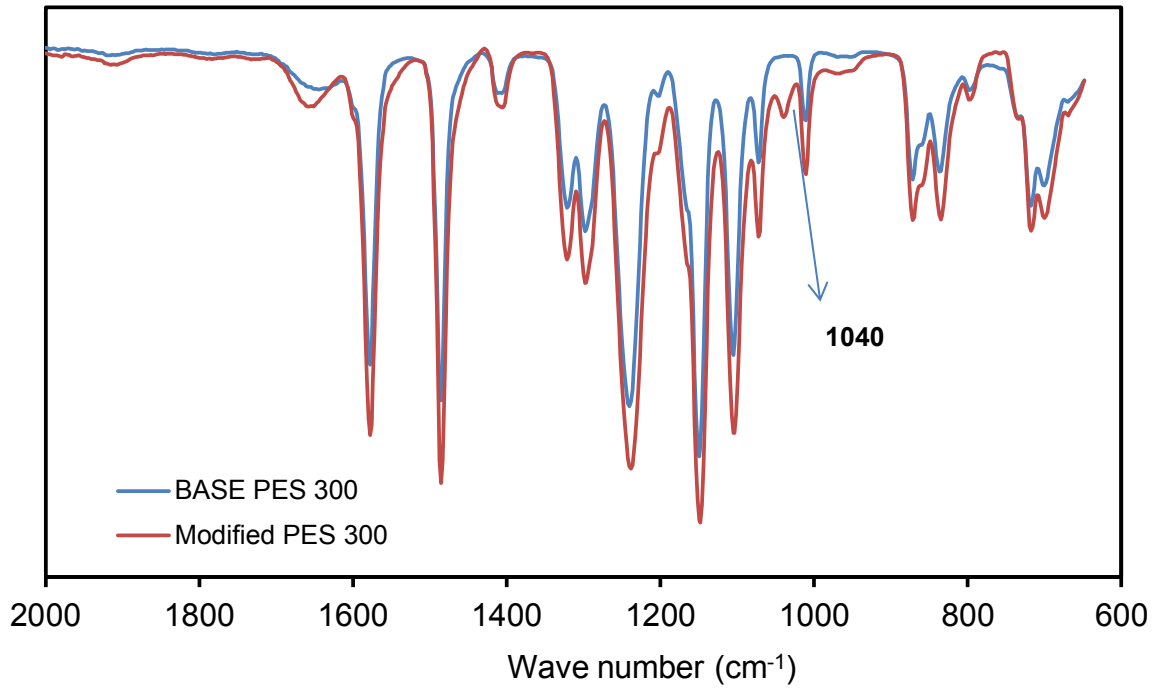

Figure 17: IR spectra showing grafted sulfonic group at 1040 wave number (cm^{-1}).

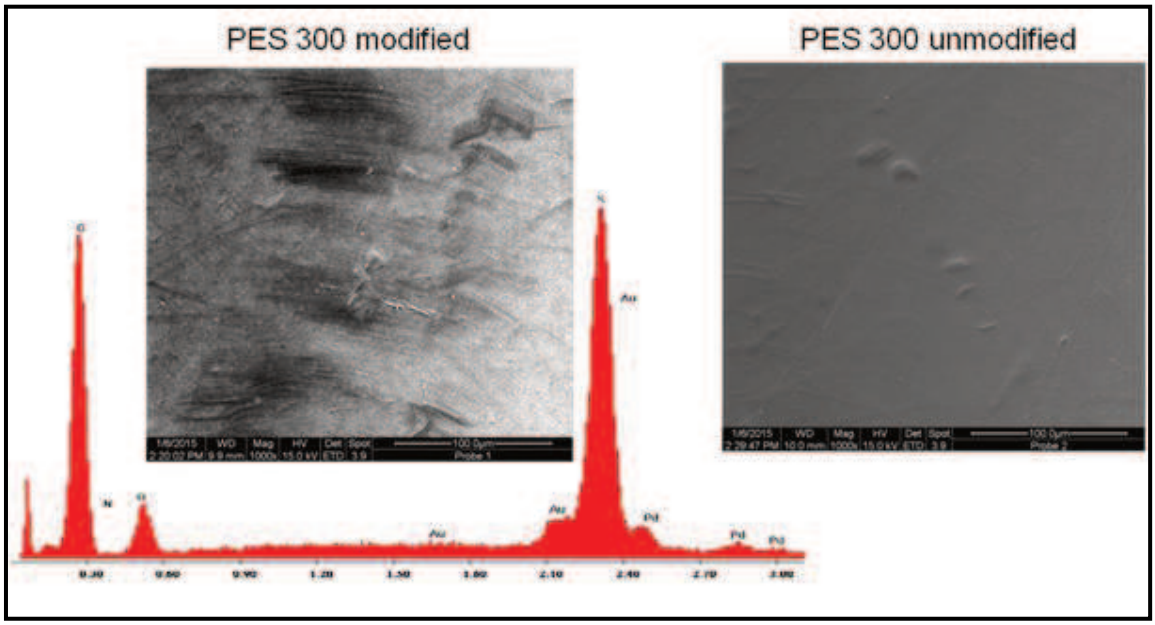

Figure 18: Energy dispersive x-ray spectroscopy /EDX) data revealing the presence of nitrogen from the grafted tertiary amino of the grafted polymer; quantitative data: modified N content 0.23 %, unmodified N content 0.0 %.

The observable changes in IR spectra and elemental analysis (cf. Figure 17) confirmed that the functional monomer has been photochemically grafted onto the based membrane even though some characteristics of IR adsorption of functional monomer peaks were not

observed after modification. The overlapping bands with those of PES base material could be the reason for the observed result.

5.2.3 Contact angle

One way to determine the relative hydrophilicity of a membrane is the contact angle (CA), which is a measure of the wettability of a surface. In this work, the hydrophilicity of the membranes was measured in term of CA using captive bubble method. The results for the different membrane types are shown in Table 4. The CA clearly showed that RC is more hydrophilic than the PES membrane due to its high water affinity. The CA of the hydrogel-functionalized PES reveal marked improvement in its wettability compared to the PES membrane, and it exhibited similar surface wettability to RC membrane. This is linked to the formation of a rigid hydration layer on the membrane surface caused by the water affinity of the functional groups which in neutral pH range should be ionized ($–SO_3^-$, $-NMe_2H^+$).

Table 4: Contact angles determined by captive (air) bubble method for unmodified and modified membranes equilibrated in water.

Membrane	Contact angle(°)
unmodified membranes	
RC 100	27 ± 3
PES 100	66 ± 2
PES 300	67 ± 4
PES 30	63 ± 5
RC 30	25 ± 4
modified membrane	
Hydrogel PES	30 ± 3

The hydrophilic character follows this order: RC 30 kDa > RC 100 kDa > Modified PES 300 kDa > PES 300 kDa > PES 100 kDa> PES 300 kDa.

5.2.4 Zeta potential

One of the aims of this study was to find alternative to the stability problems associated with cellulose base membrane by photografting a base PES membrane to hydrogel composite

membrane, which in turn will impact antifouling properties. Therefore, it is important to know the membrane surface charge. The surface charge of membrane was investigated by measuring streaming potential. Zeta potential was then calculated from streaming potential values at various pressures. This measure can also be very sensitive to changes of the surface properties. Tangential streaming potential was used because other technique, i.e. transmembrane streaming potential underestimates the ZP for UF membrane due to overlapping planes of shear [175, 176].

The result of the zeta potential (ZP) measurements as a function of pH for the different membranes are shown Figure 19. For the base membranes, as pH increased there was an increasing trend of the absolute zeta potential values (toward more negative values). Membrane RC 100 showed no isoelectric point (IEP) within the analyzed pH range, the PES membranes had an IEP in the range of 3.4 to 3.8. The relatively large negative ZP values for base RC and PES membranes underscore their ability for adsorption of electrolyte ions onto their surface. In agreement with contact angle results, there is a clear correlation that the less hydrophilic PES membranes adsorbed more anions (hydroxyl, chloride) [177, 178], leading to higher absolute zeta potential at higher pH values. For example at pH 8, the absolute ZP for the membranes with NMWCO 100 kDa from RC and PES were -52 mV and -66 mV, respectively.

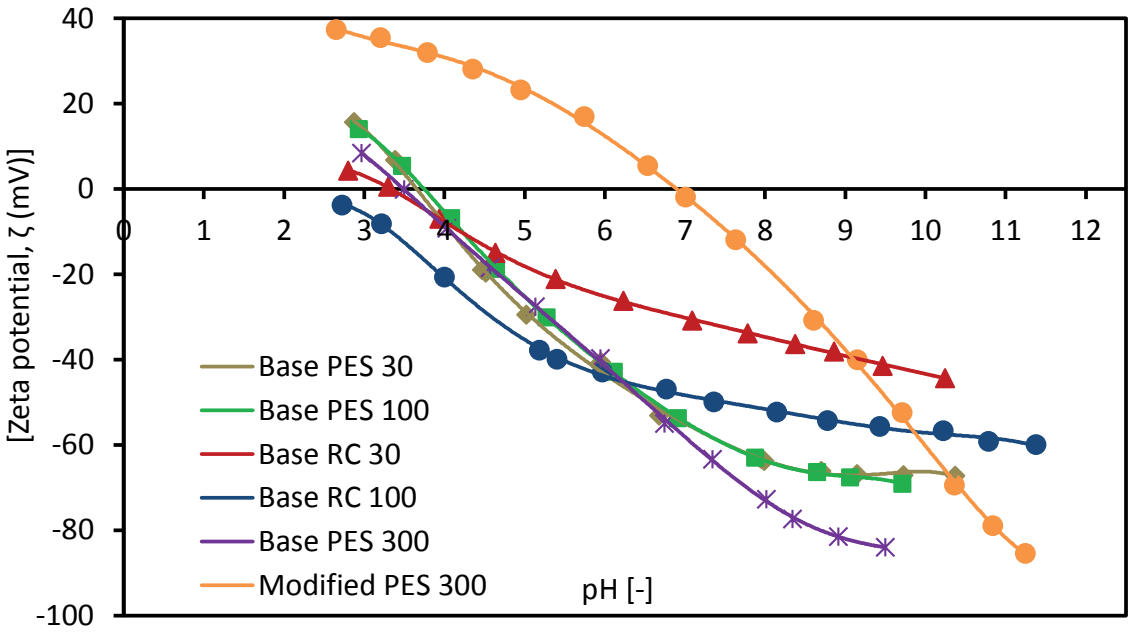

Figure 19: Zeta potential as a function of pH values for the membranes used in this study (1 mM KCl)

The macroscopically observed surface zeta-potential of the hydrogel-functionalized PES 300 is changed significantly through modification. The optimized monomer ratio used here resulted in the isoelectric point (IEP) of ~ 7. Similar shape (flat curve at low pH/positive zeta-potential and steeper curve at higher pH/negative zeta-potential) was observed, with an equimolar ratio of DMAPAA and AMPS. Additionally, the zeta-potential plateau at low pH values is raised. This might indicate that DMAPAA is more incorporated into the grafting layer since it carries a positive charge at low pH values. At high pH values (>9.5) the modified membranes exhibit an even more negative zeta-potential than the base membrane (PES 300). The sulfonic acid groups of grafted AMPS are deprotonated at high pH values carrying a negative charge that adds to the negative charge of the base membrane. At the same time DMAPAA is deprotonated as well, but as amine carrying no charge. The hydrogel-functionalized PES membrane displayed both relatively high positive and high negative zeta potential values. This is also consistent with the chemistry of the grafted hydrogel which possesses both tertiary amine and sulfonic acid groups. In one functionalization step, the

barrier pore size (cf. above) as well as the surface charge and the IEP can be designed by controlling the ratio of DMAPAA/AMPS. Considering the acid/base properties for alkyl sulfonic acid groups (pK_a ~ -1) and aliphatic tertiary amino groups (pK_a ~ 9), at pH 7, both groups should be fully ionized. Hence, the IEP may indicate that an equal fraction of anionic and cationic groups is in the grafted layer. And this would be in line with an equal reactivity of the two monomers which had been used in a 1:1 ratio (cf. Section 4.3). The absolute negative ZP values increase at increasing pH due to deprotonation of the tertiary ammonium groups. At high pH values (>10.5), this deprotonation is essentially complete, and the sulfonic acid groups of grafted AMPS are the only fixed charged groups on the surface. The negative surface charge density in this range was higher than that of PES 100, but saturation had not yet been achieved, apparently due to parallel anion adsorption. Below pH 7, the ZP values became positive, but the curved tended toward saturation (in analogy to the one for RC 100 kDa with increasing pH value). Considering the assumed equal ratio of negatively and positively charged fixed ionic groups, this effect would be due to preferential adsorption of electrolyte cations in this pH range. However, the detailed reasons for this behavior are still unclear. The obvious change in zeta potential due to grafting and the pH dependency, especially the shift of IEP toward to neutral conditions are evidence for successful incorporation of the amphoteric grafted hydrogel with approximately equimolar ratio of the two monomer units (DMAPAA/AMPS) on the surface of PES UF membrane. The pH-responsive hydrogel-functionalized membrane can impact antifouling properties probably in neutral pH range as well as additional influence on separation selectivity (by charge repulsion; for negative colloids at high, and for positive colloids at low pH [179, 180]).

5.2.5 Degree of swelling (of bulk hydrogel)

In other to have more insight, supporting experiment to measure the swelling degree of the bulk hydrogel in water as well chemical resistance (section 5.2.6) of the modified membrane was then performed (see section 4.3.1 and 4.3.2).

The bulk hydrogel of interest swells more as NaCl concentration decreases (Figure 20). The dependency is most pronounced on pH at 20 mM PB without NaCl. The average DS is 14.4. The maximum deviation from the average DS is +16 % ($\mathrm{DS} = 16.7$). Generally, the change in DS is rather low (standard deviation $\sigma_{rel} = 6\ \%$).

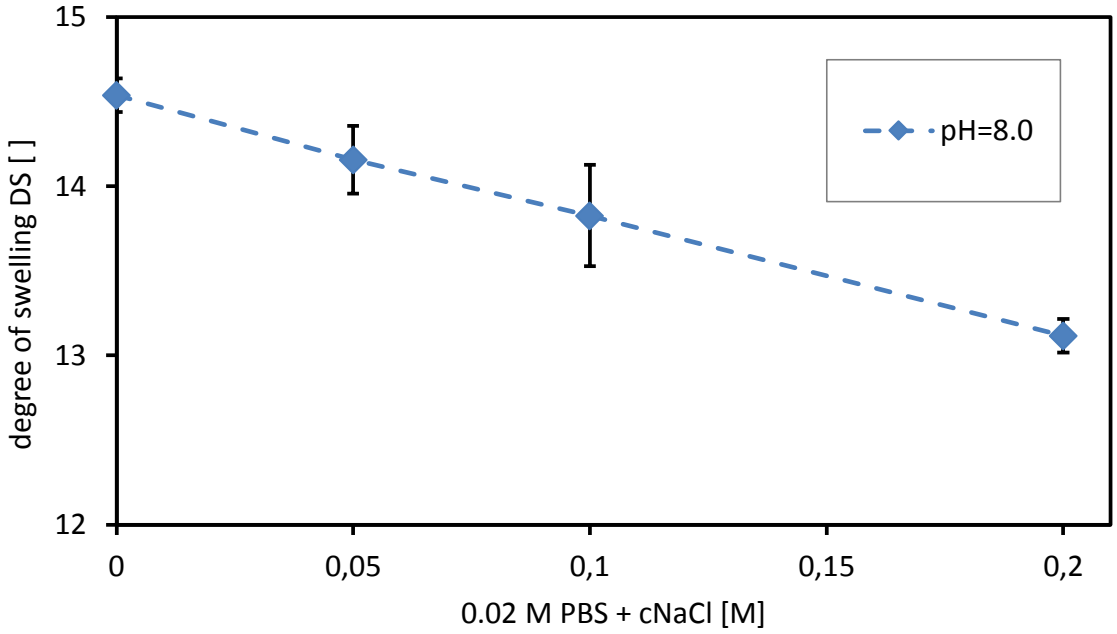

Figure 20: Degree of bulk hydrogel swelling depending on pH and salt concentration

As the ionic strength (addition of salts) is increased the repulsive forces are weakened by possible ion pairing (decreasing the net charge) and ion shielding (shorter Debye length results in weaker Coulomb-Coulomb interaction. In the tested pH, negative charges along the polymer chains dominate resulting in a repulsion of the chains. This gave insight into the high hydration of the grafted hydrogel layer as the formation of “structured” or “tightly

bound" water close to the surface is thought to be responsible for their low interactions with protein molecules.

5.2.6 Chemical resistance of modification

Figure 21 shows the DG_{grav} and permeability as measures to assess the chemical resistance of the modification against exposure to 0.1 M NaOH. It must be noticed that even the *"DG_{grav}"* of the unmodified PES 300 varies from 0 to about 60 illustrating the uncertainty of this type of measurement. For modified PES 300 the initial DG_{grav} is highest, but afterwards underlies quite high variations. In contrast, the values of permeability show rather smooth trends for both, unmodified and modified PES 300, at the beginning of exposure rising distinctly and later increasing further but only very slightly. Anyway, the permeabilities of unmodified and modified PES 300 differ at any stage by a factor of 5 or more. Thus, the modification is considered to be fundamentally stable and furthermore, effective for at least 7 days of exposure (equaling more than 1000 cleaning cycles of 10 minutes).

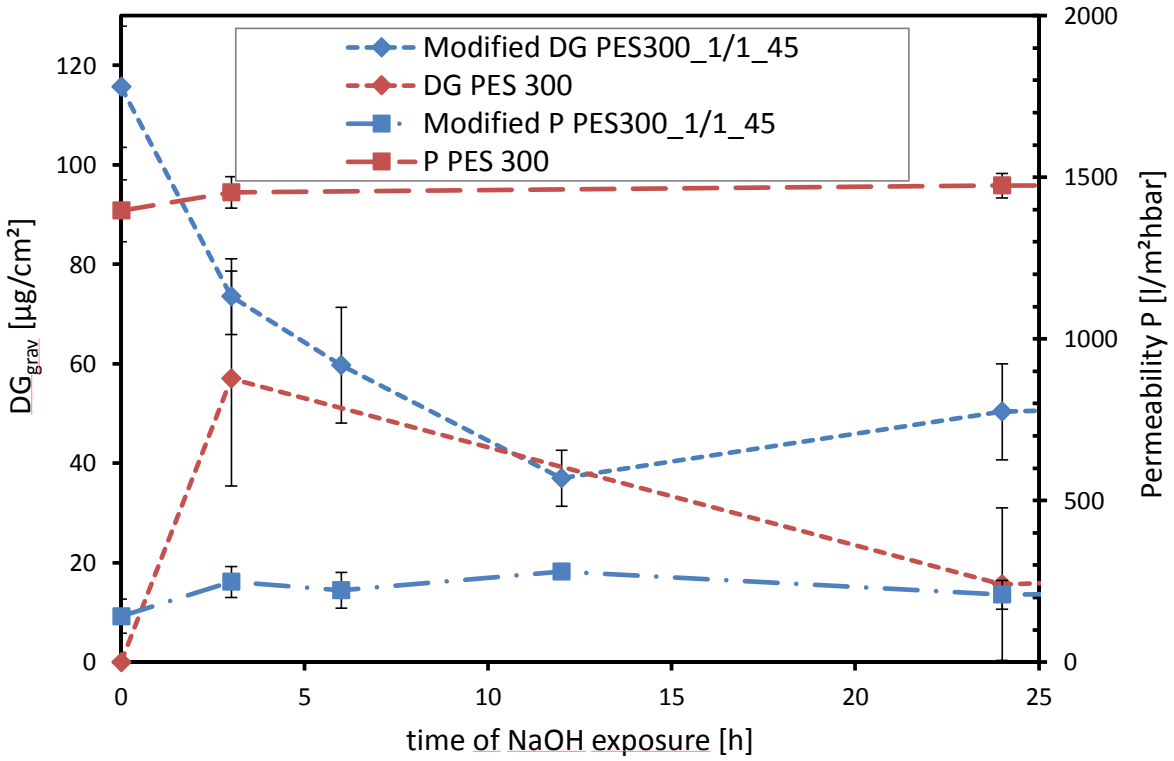

Figure 21: DG_{grav} and permeability as function of NaOH exposure time

There is no evidence that this would not be true for even a much longer period. In addition, IR spectroscopy definitely indicates the presence of AMPS after 7 days of exposure.

The most probable reason for loss of polymer from the modification layer is wash-out of non-bonded polymer chains that have been formed by chain transfer during radical polymerization. Since the polymer chains are rather long they may be wrapped or coiled and thus not removed by washing with water. It seems that only at high pH values the repulsion of the chains gets strong enough to unwrap and wash out the polymer. In contrast, basic hydrolysis of the peptide bond probably plays only a minor role for polymer loss because the peptide bond can be considered stable at room temperature [181]

5.3 Water permeability and molecular weight cut-off

Water permeability could show changes in membrane morphology of the separating layer that result from surface modification. Membrane sieving or rejection is one of the important characteristics for UF membrane. This characteristic will determine selectivity of UF membrane. An overview on the UF membranes with their nominal MWCO, measured water permeability and experimentally determined MWCO using dextran is provided in Table 5.

An established correlation between the molecular weight of dextran and its size in solution was used to calculate the barrier pore diameter from nominal or experimental MWCO [182].

Pure water permeabilities for membranes PES 100, RC 100 and hydrogel-functionalized PES 300 membrane (cf. Section 5.8.1) were very similar. For the two 100 kDa commercial membranes, these experimentally determined MWCO values were larger than the nominal MWCO values provided by the manufacturer. On the other hand, experimental data for PES 100 was smaller than data from earlier studies on the same PES membrane from this manufacturer (MWCO 350 kDa [183]). Comparable results were also found for the PES and

30 kDa with PES 30 having higher water permeability and the measured MWCO (dextran) (cf. Table 5).

Table 5: Pure water permeability, experimentally estimated cut-off from ultrafiltration of dextran and GPC and correlation between MWCO and barrier pore size for the UF membranes used in this study.

	Membrane				
Membrane sample	Company provided NMWCO (kDa)	Estimated pore diameter using [182] (nm)	Water permeability (L/hm^2bar) [a]	Measured MWCO for dextran (kDa) [a]	Estimated pore diameter using [182] (nm) [a]
PES	300	23	1430 ± 120	nr [b]	nr [b]
hydrogel PES [c]	-	-	360 ± 80	184	17
PES	100	13	530 ± 10	180	17
RC	100	13	400 ± 15	133	15
RC	30	6	127 ± 2	7	3
PES	30	6	174 ± 8	11	4

[a] determined in this work
[b] no significant rejection observed for the used feed mixture
[c] prepared from PES 300 kDa

In case of PES 300 there was no significant size selectivity observed with the used dextran mixture (average molecular weight of the largest fraction 2000 kDa); thus no MWCO could be determined. This effect may be connected to this membrane's large pore sizes as observed in SEM (cf. Figure 15). On the one hand, rather large discrepancies between nominal and measured MWCO and also difference for experimental data for different batches of the same membrane are typically observed for ultrafiltration membranes. One may also conclude that measurement conditions (cf. Section 4.7.4), namely filtrate flux (to minimize concentration polarization) and dextran size range, might still need further optimization. However, most important for this study, a direct comparison of the three membranes used later on was possible. And it was found that the MWCO and hence barrier pore size of the two commercial membranes (PES 100 and RC 100) with similar water

permeability was very similar (also in line with their similar surface porosity and pore sizes seen in SEM; (cf. Figure 15), and the experimental MWCO of the hydrogel composite PES membrane based on PES 300 was identical with the values determined for PES 100. The reduction in MWCO (cf. Table 5) is in agreement with the effects of the grafted hydrogel layer on effective barrier pore size of the PES 300 membrane, and this is analogous to findings in earlier studies (cf. [183]). Considering that the preserved base PES membrane pores are covered with a swollen hydrogel layer (cf. Section 5.1), a direct comparison and the evaluation of the effect of the post-functionalization on separation performance are possible.

5.4 Properties of model colloids

5.4.1 DLS and TEM

As UF separation principle is based on size, it is imperative that the size of the dispersed components are determined based on our experimental conditions. The sizes of the model proteins (BSA, LYS) and the silica nanoparticles from literature and own experiments using DLS and TEM as well as other relevant data are summarized Table 6.

Table 6: Physical properties of model colloids used in the study

Property	SiO_2 NP	BSA	LYS
Molecular weight (kDa)	-	67[a]	14.3[a]
Isoelectric point	< 3,5[a]	4.9[a]	11.0[a]
Molecular dimensions (nm)	-	14 × 4[a]	4.5 × 3[a]
Diameter (nm)	20[b]; 35[c]; 26[d]	7[a]; 9[c]	4[a]; 5[c]

[a] Literature data [184]; [b] manufacturer data; [c] from DLS (pH = 8), determined in this work; [d] from TEM, determined in this work

BSA and LYS analyzed by dynamic light scattering at pH 8 and 1 g/L in aqueous solution showed particle sizes similar to literature data [184], and also in agreement with the "molecular dimensions" (cf. Table 6) which are taken from the crystal structure. The slight differences for the colloidal diameter in comparison to literature data might be related to

different measurement conditions. The size distribution for BSA is shown in Figure 22. (cf. Table 6).

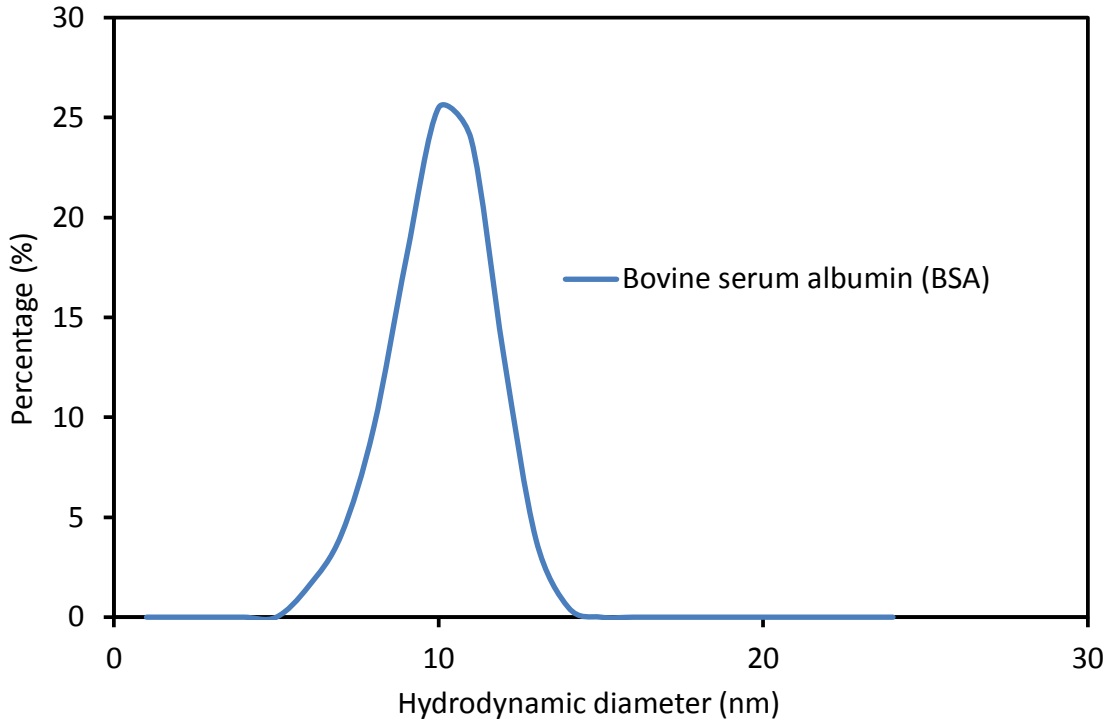

Figure 22: BSA hydrodynamic particle size distribution

The influence of concentration on the BSA hydrodynamic particle size measured at pH 8 is depicted in Figure 23. Some factors affecting DLS measurement are experimental conditions as well as temperature, solvent properties (pH, viscosity), concentration and interparticle interactions. It can be seen (cf. Figure 23) that the tested concentration has no significant impact on the apparent or observed BSA particle size. In addition, there was no further ionic strength other than that from the buffer solution (20 mM) which enhances the "salting-in" effect. The concentration was too low to perturb or alter strongly the size of BSA particles. In addition the samples have monomodal size distributions which are monodisperse (cf. Figure 22). Polydispersity can be very low with spherical particles which were assumed in the case with our model solute. The degree of polydispersity (cf. Figure 23) is below acceptable range from 1 g/L. It is considered to be satisfactory as long as the standard deviation on

$Dt\ or\ on\ d_h \leq 15\ \%$. [185]. The high polydispersity with concentration of 0.2 and 0.5 g/L may be due to temporary aggregates caused by pressure from long-range electrostatic interactions from the more diluted solution samples. As proteins often tends to aggregate in polar solvents, especially in aqueous solution. Another possible reason could be just due to aggregation or contamination from dust particles/large particles from the sample solution.

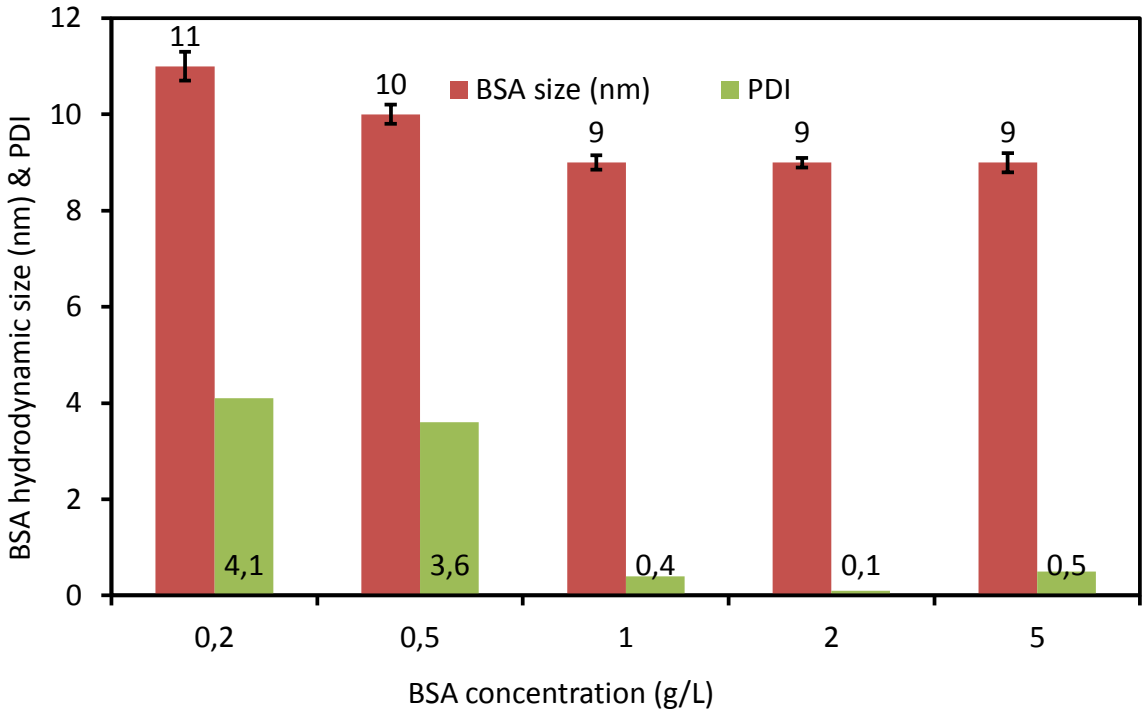

Figure 23: Influence of concentration on BSA hydrodynamic size in relation to polydispersity index (PDI)

The relatively higher hydrodynamic particle size at the lowest concentration can as well be related to full particle hydration with water molecules. As the concentration of the particle is increased there is less individual particle hydration, thus the DLS measurement shows less hydrodynamic particle size.

The observed variation with silica nanoparticles size (cf. Table 6,) is connected to a hydration layer which is absent in the investigation with TEM. However, the TEM result disclosed a distribution in the particle size of silica as shown in Figure 24, so that the values

determined by DLS are definitely only average values. The size distribution for SiO_2-NP with DLS is shown in Figure 25 (cf. Table 6).

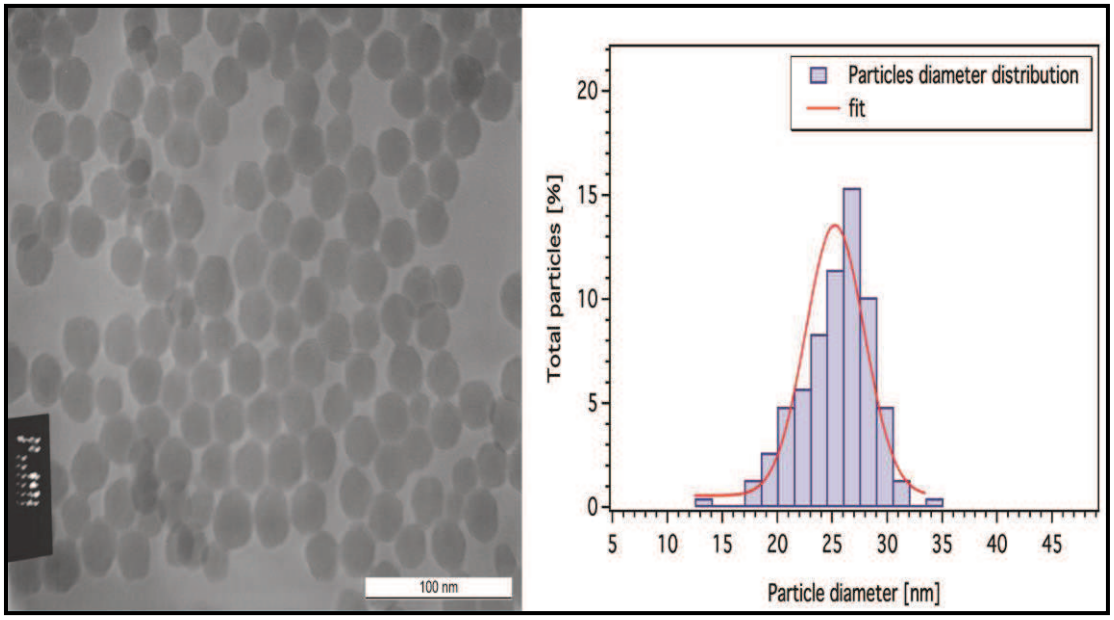

Figure 24: TEM image of the silica nanoparticles and size distribution obtained from this analysis. The distribution was determined by manually measuring size of all the single particles in the TEM image with the 100 nm scale bar as reference

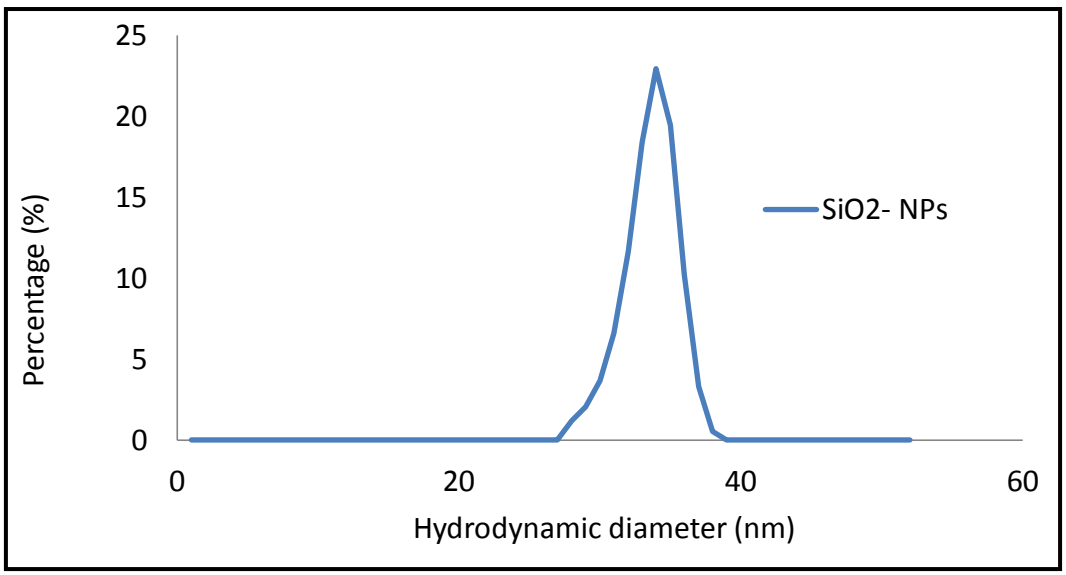

Figure 25: SiO_2-NP Hydrodynamic particle size distribution.

The effects of concentration on the SiO_2-NP hydrodynamic particle size measured with DLS at pH 8 is depicted in Figure 26. Aside the concentration at 0.2 g/L the SiO_2-NP size and the

polydispersity are stable within the tested concentration. This is in line with monodisperse sample were particles are identical in size and shape.

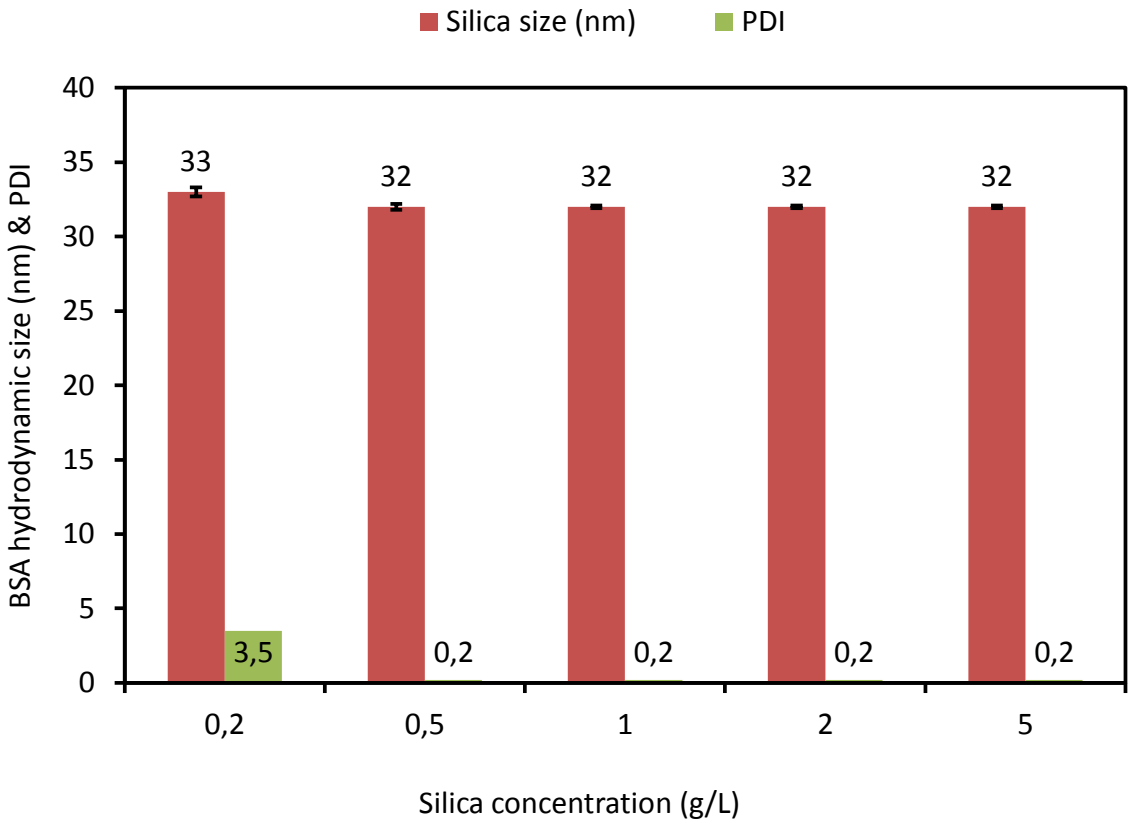

Figure 26: Influence of concentration on SiO_2-NP hydrodynamic size in relation to polydispersity index (PDI)

In the above case (cf. Figure 26), we have the evidences that suggest the pH 8 (buffer concentration of 20 mM) has no shading effect on the interparticle interactions. Thus the pH as well as the increasing concentration of SiO_2-NP merely increases the surface charge. This will reduce the intermolecular distances between the SiO_2-NPs, causing some natural and induced repulsion between particles, thus stabilizing the dispersion. As a result, the apparent size decreases therefore maintaining the particle size and PDI. The large PDI at 0.2 g/L could be related to contamination (e.g. dust particles) or artifacts from measurement background at low concentration.

5.5 Mixture stability

Purification of nanoparticle dispersion is the principal goal of this work. For practical purification to be possible the colloidal nanoparticles should be in single stabilized form, i.e. clear and free of agglomerations that precede sedimentation. Different pH conditions were tested and the result of the best suitable condition necessary to effect separation later in the work (cf. section 5:10) is shown in Figure 27.

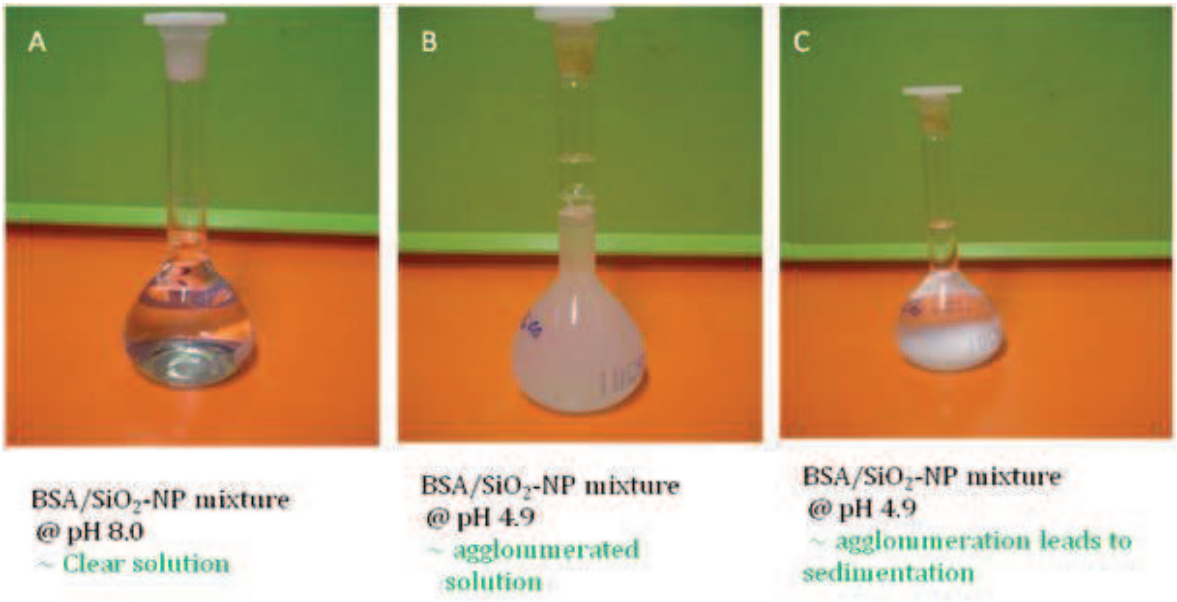

Figure 27: Mixture stability test for BSA/ SiO_2-NP at pH 8 and 4.9.

The SiO_2-NP has IEP below 3, at this pH the particles are positively charge. At pH 4.9 which is about the IEP of BSA the net charge is zero. There is strong attraction between the positive part (amine group) of the protein and the SiO_2-NP which is now net negative at pH 4.9. Therefore the cloudy phenomenon observed in (cf. Figure 27(B)) is rapid agglomeration and resultant sedimentation (cf. Figure 27(C)). Thus the clear solution at pH 8 (cf. Figure 27(A)) confirms electrostatic stabilization through solution pH manipulation which implies the possibility of fractionation/separation of the model mixture. Similar phenomenon was observed for LYS/SiO_2-NP mixture, at pH of 12 which is one unit above the IEP of LYS (cf. Table 6), the mixture has a net negative charge with clear and stable dispersion without

agglomeration or precipitation. Thus investigations with LYS/SiO2-NP were performed at solution pH of 12.

5.6 Analysis (concentration determination)

In other to ascertain the fractionation abilities and purification efficiency of the studied membranes, quantification of the feed, permeate and retentate concentration were necessary. The model mixtures require analytical techniques that are devoid of interferences and high selectivity. For the protein/silica mixtures, the test tube procedure of the Micro BCA™ Protein Assay Kit has been expanded to quantify the concentration of proteins in the mixture. On the other hand, AAS has been established to determine the silica concentration in the mixture. The calibration curve to quantify the amounts of BSA or LYS after UF and as well as in the presence of silica is shown in Figure 28 (cf. section 4.6) The calibration of the proteins in the mixture was only shown (cf. Figure 28). The correlation, that is R^2, was found to be ≥ 99.5.

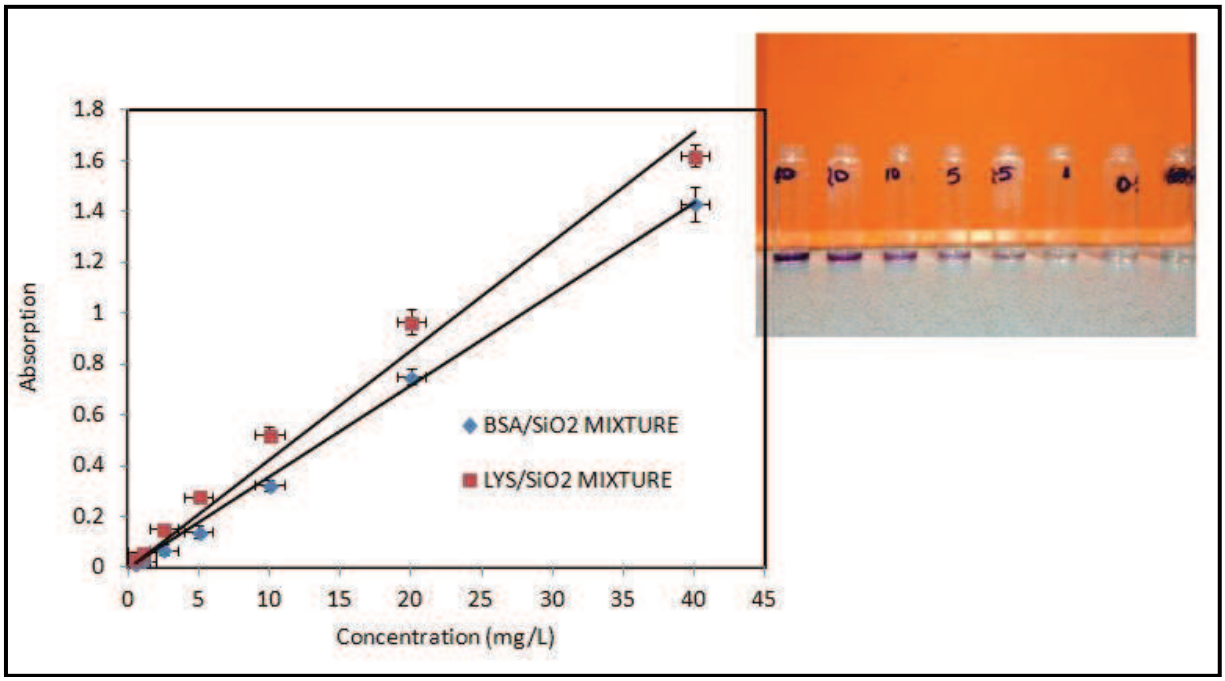

Figure 28: Calibration to quantify the amount of BSA or LYS in the mixture with SiO_2-NP using Micro BCA™ Protein Assay Kit.

The suitability of this method, i.e. no interference of silica on protein quantification, is depicted in Figure 29.

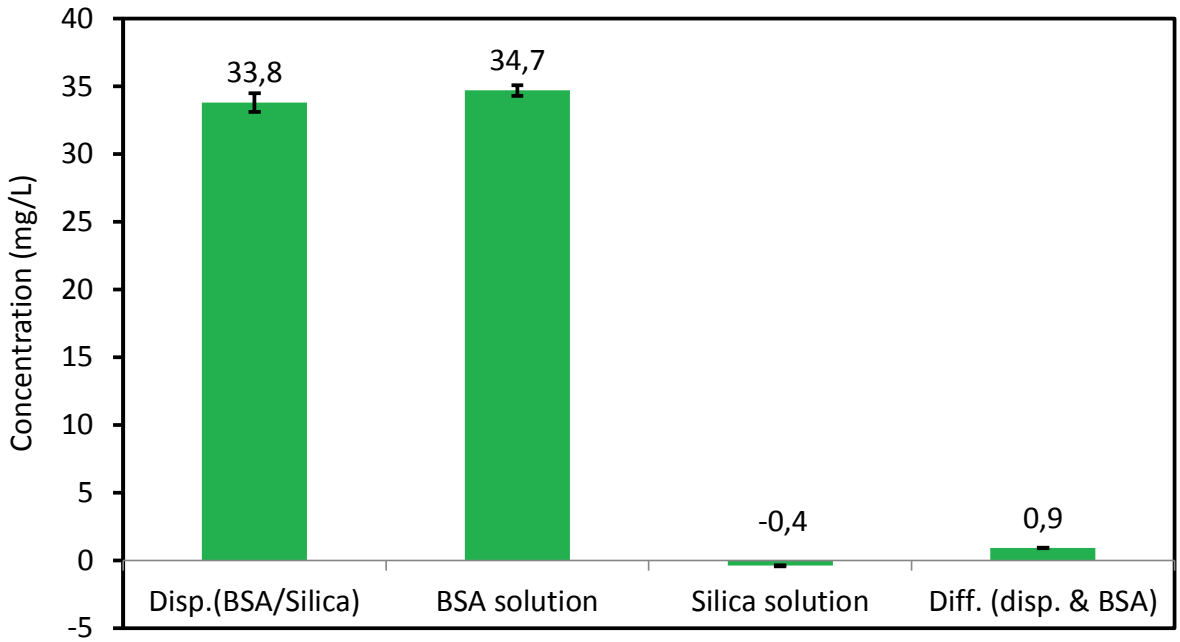

Figure 29: Method suitability test to establish the use of Micro BCA assay to determine BSA concentration in BSA/silica mixtures (concentration of silica 200 mg/L).

The very slight negative value for silica dispersion implies no reaction with BCA assay components. The experimental error was less than 3 %. Similarly Colloidal silica was detected quantitatively by AAS method (cf. section 4.6) with protein mixture. This was a novel alternative for the model mixture (concentration determination) after the silica calorimetric method (Heteropoly Blue method) failed because of weak reactive nature of SiO_2-NPs used. The presence of BSA, LYS and/or K-Na-phosphate buffer (20 mM) did not have significant influence on the measurement as the flame lamp used was specific to silica atoms. The calibrations with AAS to emphasize the above mentioned no interference and to determine the concentration in various mixtures is shown in Figure 30. The single silica particles and the samples containing either LYS or BSA gave similar results with correlation of R^2 found to be above 99.8. Other single calibrations and comparison for both methods of analyses is shown in appendix 8.3 (A.1-A.3 and A.4).

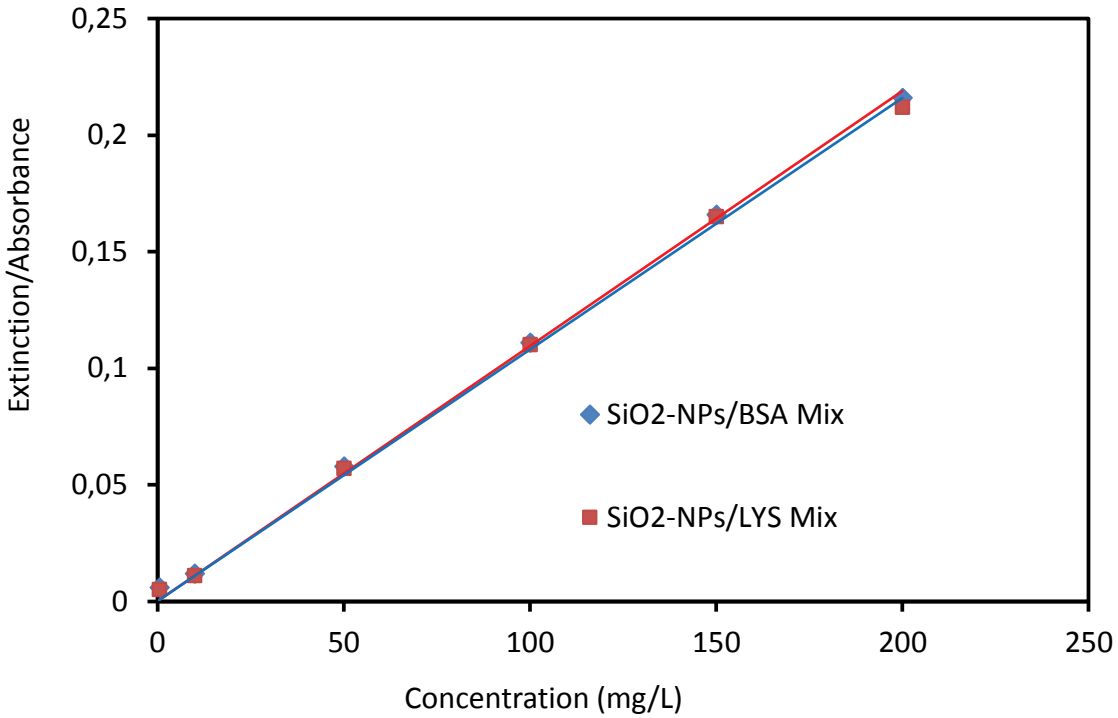

Figure 30: AAS calibrations to show no influence of BSA or LYS concentration in the mixture of BSA/SiO2 and LYS/SiO2

5.7 Static adsorption of colloids

UF fouling is strongly influenced by membrane–solute interactions. Therefore, protein–membrane interactions were investigated. In order to assess the adsorptive fouling by BSA, analyses of the loss of water permeability due to contact with BSA solution without filtration had been done and shown in Figure 31. The results demonstrate that this fouling phenomenon is significant for unmodified PES 100 and 30 kDa membranes were hydrophobic solute-membrane interactions dominate. In contrast, the RC membranes were least fouled by the protein. This is analogous to results of earlier studies with focus on the comparison between PES and RC ultrafiltration membranes [52]. The hydrogel-modified PES membrane has obviously much higher resistance to BSA adsorption and fouling compared to unmodified PES; the water permeability loss was within the range of error identical to the value for the RC 100 membrane.

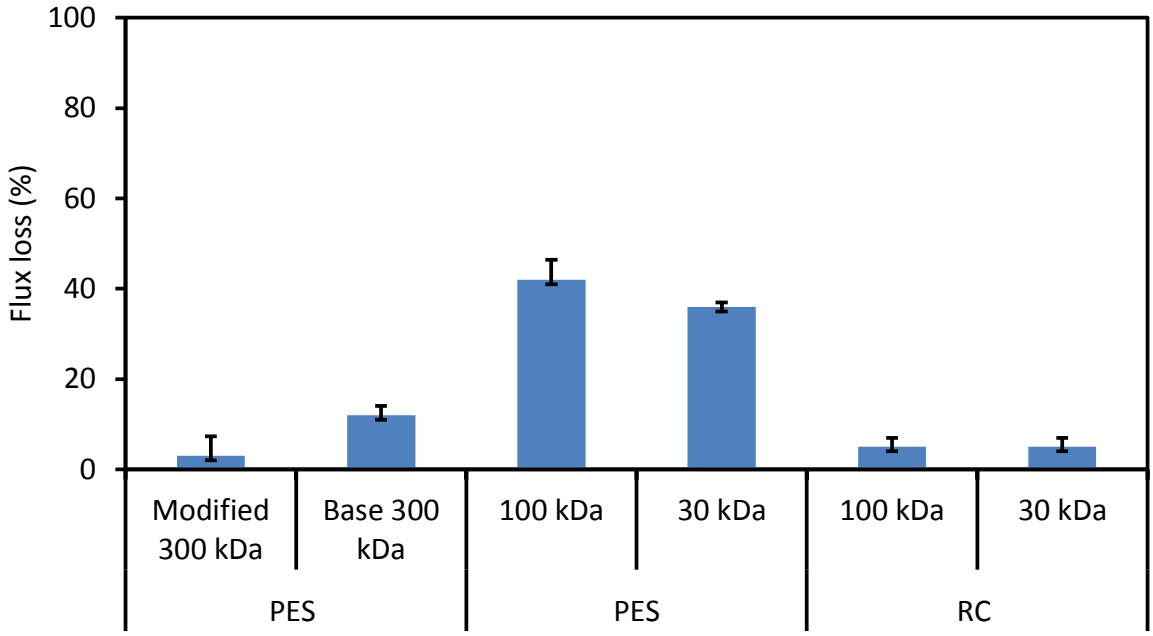

Figure 31: Flux loss after BSA static adsorption at pH 8, concentration of BSA 1 g/L, for 1 hour with all the studied membranes.

The lower flux loss for the base membrane PES 300 compared to PES 100 could be due to its larger barrier pore size (cf. Table 5).

5.8 Flux and ultrafiltration separation performance

5.8.1 Water flux

Flux and selectivity are important UF performance parameters that can influence choice of membrane for a particular application. Water flux can reflect transitioning from dry state to a compacted and water-swollen state as well give insight to changes in overall membrane morphology that result from surface modification. The water flux versus TMP for all the studied base membranes and hydrogel-functionalized PES 300 membrane is shown in Figure 32. All membranes showed linear response to the applied pressure. Three samples were run in parallel and their deviations are within experimental errors (relative deviation was less than 0.1 %).

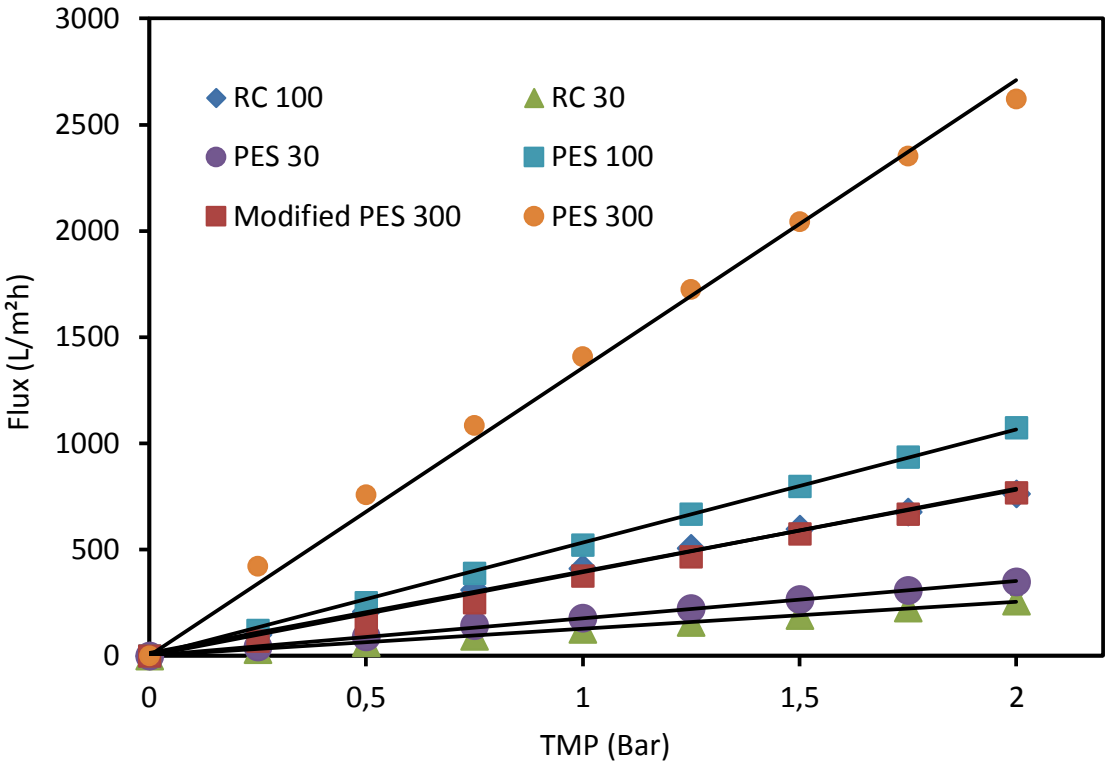

Figure 32: Water flux versus TMP for the studied membranes.

Hydrogel-functionalized PES 300 membrane showed how the grafted layer affected the flux of the separating layer after surface modification. Moreover, H_{gel}F-PES 300 has similar flux with RC 100. In general the PES membrane has higher flux responses than the RC membrane which is connected to the larger surface pores according to by *Hagen-Poiseuille's* law and MWCO (cf. Table 5).

5.8.2 Influence of pressure with BSA and BSA/silica mixture

Ultrafiltration experiments were conducted to know the performance of modified membrane from a practical application point of view in comparison to base membrane with similar MWCO (cf. Table 5). It is important to note that BSA solution (1 g/L, pH 8.0) was used to evaluate the three membranes types under pressure. Further investigation involving BSA filtration was expressed in terms of permeate flux/initial water flux ratio and critical flux for

the studied condition was determined. Flux versus pressure profiles of the three different membrane types are shown in Figure 33.

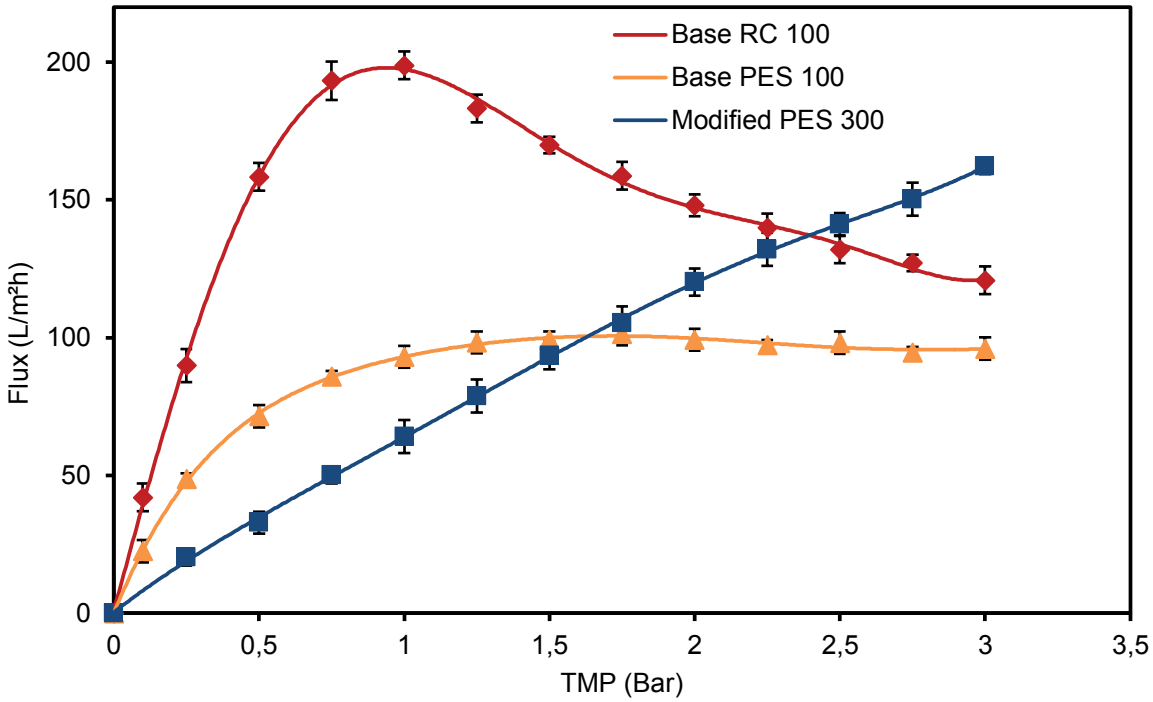

Figure 33: Relationship between applied transmembrane pressure and permeate flux using BSA solution concentration of 1 g/L in phosphate buffer at pH 8.

The permeability during BSA ultrafiltration with PES 100 is lower in comparison to pure water permeability. For example, at 0.75 bar the BSA filtrate and the pure water permeability are 86 and 530 (L/m^2hbar), respectively. The characteristic curve for membrane PES 100 is similar to what is normally observed for a flux pressure profile, e.g. in situations where the solute particle size is larger than the membrane pore size, i.e. when there is complete size exclusion. Beginning with low pressure, shear and lift forces are sufficient to minimize BSA deposition, enabling the flux to increase linearly with pressure. As the BSA starts to deposit on the membrane due to convective flow, the effect of pressure on flux is decreased. Additional increase in pressure will only increase the thickness of the rejected BSA layer without corresponding increase in flux. The increase in convective transport of BSA

toward the membrane will lead to corresponding increase of diffusive back transport of BSA into the bulk phase, thus reaching steady state. Alternatively, there could be gradual BSA adsorption at the onset of filtration with BSA solution. This is responsible for low flux effect even at increasing pressure, thus reaching limiting flux at low pressure (i.e., also after short ultrafiltration time because the experiment had been done by step-wise increasing the pressure; cf. below). The stable limiting flux might be due to monolayer adsorption coverage and subsequent convective flux of BSA will lead to bulk diffusion.

Membrane RC 100 shows the largest increase of flux in response to pressure, in the range up to 0.75 bar. The filtrate flux in comparison to pure water flux is shown in Figure 34.

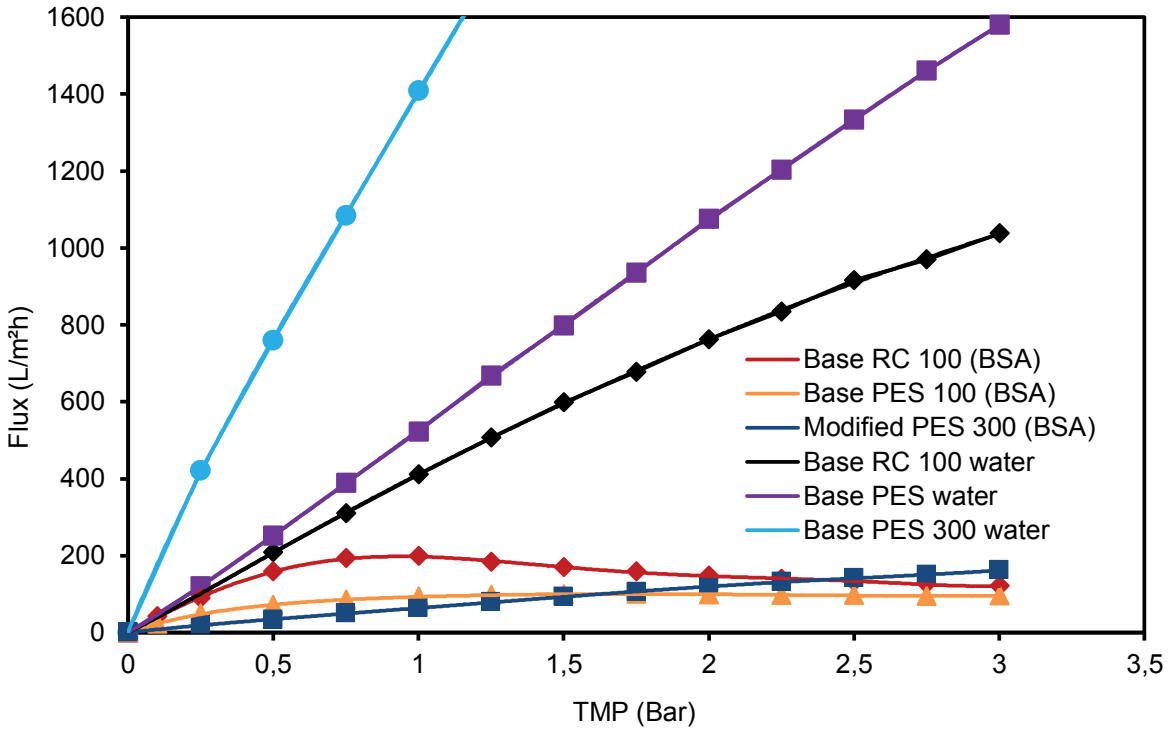

Figure 34: Relationship between applied transmembrane pressure and permeate flux using BSA solutions at a concentration of 1 g/L in phosphate buffer at pH 8, in comparison with pure water flux.

As expected, the permeability during BSA ultrafiltration is lower than pure water permeability. At the same transmembrane pressure of 0.75 bar the BSA filtrate and the pure water permeability are 258 and 411 (L/m^{2}hbar), respectively. The BSA filtrate flux (cf. Figure

33) reached a maximum at around 1 bar and decreased as pressure further increased. One possible reason for this behavior could be the neutral and low fouling properties of RC membrane which have enhanced the convective transmission of BSA considering its molecular weight (cf. Table 5 and Section 5.3) during the initial increase in pressure and the attendant flux response. In addition as pressure is further increased there is rapid membrane compaction which not only reduces transmission but cause concentration polarization (CP) from the former, inducing more particle interactions that increased the intrinsic rejection as was later observed during BSA purification (cf. Section 5.9). This coupled effect summarizes one reason for the flux decrease phenomenon seen with membrane RC 100 (cf. Figure 33). Another explanation relating to this behaviour could be the result of relatively high concentration of BSA retained on the membrane due to the increasing pressure. The concentrated layer near the membrane is less permeable for the permeable substance (water), hence affecting flux in comparison with an unaltered solution operated under subcritical fixed flux. The BSA concentration at the membrane interface will change into a gel with additional resistance. The second resistance coupled with possible induced osmotic pressure at the membrane barrier, could interpret the decreasing flux in UF of BSA using RC 100 kDa (cf. Figure 33).

The hydrogel-functionalized PES 300 membrane has the lowest flux among the three membranes in the low range of flux versus pressure profile (cf. Figure 33). However, it has shown linearly increased flux with increasing transmembrane pressure. This obvious BSA fouling resistance can be related to the grafted hydrogel layer with hydrophilic and neutral properties which were also evident in the contact angle and the zeta potential streaming data (cf. Section 5.2.3 and 5.2.4).

To look more into the details of the behavior of the two more promising membranes, the hysteresis for RC 100 and hydrogel-functionalized PES 300 membrane is shown in Figure 35. After step-wise increase of transmembrane pressure until 3 bar, the pressure was subsequently decreased step-wise, again for 3 minutes intervals per point. The very large hysteresis for RC 100 is characterized by a pronounced plateau region in the range where flux decreased during the pressure stepping (PS) part of the experiment and a sharp decline below about 0.5 bar and ~ 60 L/m^{2}h during the pressure destepping part (PDS). Therefore, the behavior for the PS part can be explained by gel layer formation and compaction. More so, during PDS the consolidated BSA layer may not have been removed by the shear forces emanating from the dead end filtration process. The hydrogel-functionalized PES 300 membrane revealed much less hysteresis as compared to RC 100 membrane. The hydrogel-grafted membrane's resistance to fouling is the main reason for this behavior.

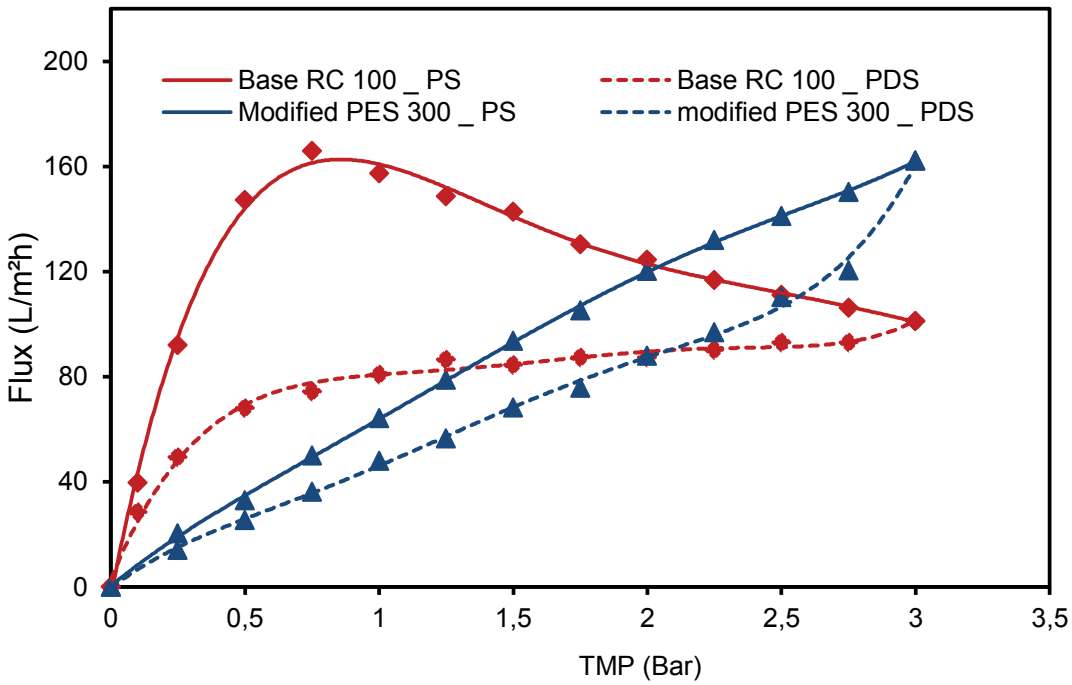

Figure 35: Relationship between applied transmembrane pressure and flux using a BSA solution with a concentration of 1 g/L in phosphate buffer at pH 8; (solid line: pressure stepping /PS/; dashed line: pressure destepping /PDS/).

In this work 50 L/m²h critical was chosen based on the preliminary tests with the intention to operate below critical flux (CF). During the investigation the weak form of critical flux was observed. This was calculated through direct deviation from the initial slope at the onset of filtration although linearity was maintained until a particular transmembrane pressure (TMP) was reached. This was attributed to the viscosity of the feed solution.

The critical fluxes determined through deviation from initial slope (i.e. assuming weak form of critical flux; cf. [42] for RC and PES 100 kDa membranes were calculated to be 90 and 50 L/m²h, respectively; the value for the hydrogel-functionalized PES 300 membrane was larger than 150 L/m²h (see appendix 8.4 for details (A.7-A.9 and Table A.2)). Relative flux versus time during ultrafiltration of BSA and of BSA/silica mixtures for the three different membrane types with similar MWCO (cf. Table 5) is depicted in Figure 36.

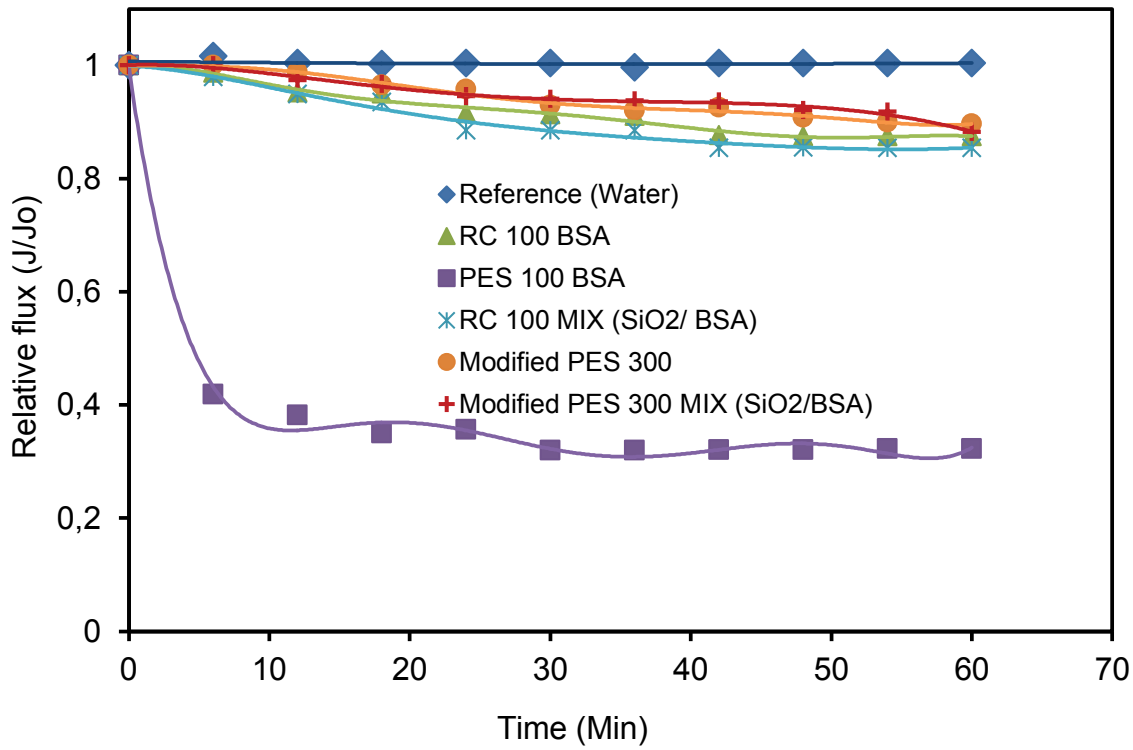

Figure 36: Flux versus time to determine fouling resistance; using initial flux ~ 50 L/m²h, phosphate buffer at pH 8, BSA and mixture (BSA/SiO2) concentration of 1 g/L

The evidence of large fouling tendency is clearly seen with PES 100 membrane. In contrast, the RC 100 membrane showed good filtration performance and fouling resistance for both BSA and the dispersions mixture (BSA/SiO2).

The hydrogel-functionalized PES 300 membrane showed even slightly higher fouling resistance in comparison to the RC 100 membrane. This improved ultrafiltration performance for the modified PES is connected to the grafted hydrogel layer as discussed above and in Section 5.2. For both RC and amphoteric hydrogel-grafted PES membranes, the tight surface hydration, i.e. a water layer which is not easy to be replaced by any kind of adsorbed solutes, are responsible for the anti-fouling performance.

To evaluate the importance of sustainable flux operation, i.e. at minimal or only modest degree of fouling, ultrafiltration at subcritical flux (the value for PES 100, the lowest among the three membranes /cf. above/, had been used) and higher fluxes have been carried out; the result is shown in Figure 37.

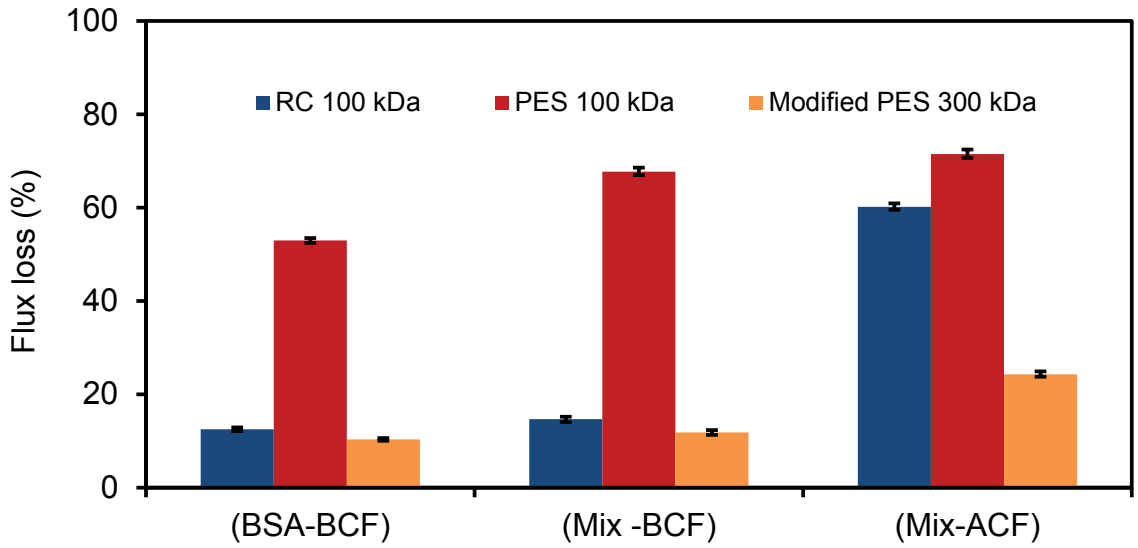

Figure 37: Effects of subcritical and high flux operations on flux loss after ultrafiltration for 1 hour. BCF: below critical flux, i.e. ~ 50 L/m²h, ACF: above critical flux, i.e. ~ 100 L/m²h; BSA and BSA/silica mixture at concentration of 1 g/L in phosphate buffer at pH 8.

Membrane permeability was reduced by at least 50 % for the PES 100 membrane. The low water flux losses (not more than 10 %) show that RC and the hydrogel-functionalized PES 300 membrane have similar filtration performance for both single BSA and BSA/silica mixture filtration below critical flux of ~50 L/m²h. Above the critical flux, the permeability loss was much larger for the RC 100 membrane. And this may be related to the fouling observed in the pressure-stepping experiment (cf. Figure 35 and Figure 36). In contrast, the hydrogel-functionalized PES 300 membrane showed better performance at the higher flux, and this is in line with the much higher critical flux for this membrane (cf. above). One can conclude that sustainable flux through sub-critical flux operation can minimize CP and fouling but not completely eliminate it.

5.9 Model solute ultrafiltration and membrane selection (unmodified base membranes)

Rejection measurements were carried out to evaluate the performance of the commercial membranes, and then finally to select those, that show better selectivity and minimal fouling. The rejection abilities of the different base membranes using the model solutes (BSA and SiO_2-NP) with two analytical techniques are described Table 7. Single silica rejection for the RC 30 and 100 membranes was 100 % for both analytical methods. With exception of fluorescence spectroscopy which yielded 96 % for PES 100, other PES membrane types were ≥ 99 %.

With respect to the two analytical techniques, AAS is more sensitive as the detection limits under the used conditions were determined as 1 mg for AAS and 5 mg for fluorescence spectroscopy (see Appendix 8.3 for details (Table A.1 and A.4)). The different analytical sensitivity may explain the slight differences obtained with both techniques.

Table 7: Rejection and water flux recovery, obtained in batch UF of single silica and BSA dispersions/solutions; initial concentration 0.2 g/L in phosphate buffer pH 8, initial flux ~50 L/m²h.

	SiO_2-NP rejection (%)			
	RC 100 kDa	PES 100 kDa	RC 30 kDa	PES 30 kDa
Fluorescence Spectroscopy (Fl. Spec.)	100 ± 2	96 ± 1	100 ± 1	99 ± 2
Atomic Absorption Spectrometry (AAS)	100 ± 0.4	99 ± 0.1	100 ± 0.4	99 ±0.4
Water flux recovery (%)	100 ± 2	87 ± 3	100 ± 2	96 ± 4
	BSA rejection (%)			
UV-Vis Absorption Spectroscopy	58 ± 3	100 ± 1	100	100
Water flux recovery (%)	99 ± 2	70 ± 2	100 ± 2	98 ± 2

The very high rejection can be related to the membrane barrier pore sizes (cf. Sections 5.3) which are smaller than the silica size (cf. Table 5). Moreover, the high rejection is also associated to the high negative zeta potentials of SiO_2-NP (-50 mV) and the membrane surface at pH 8 (around -60 mV; cf. Section 5.2.4). While the former may arise due to direct dissociation or ionization of surface group, the later is caused by preferential adsorption of ions in solution. All membranes showed good flux recovery after silica ultrafiltration, but RC membranes performed much better than PES membranes. The repulsive interactions coupled with low flux operation have reduced protein/colloid adsorption and concentration polarization effects, thus promoting excellent (for RC) and relatively high (PES) water permeability recovery.

The observed BSA rejection for PES 100 was 100 % while only 58 % was found for RC 100 membrane (cf. Table 7). For RC and PES 30 kDa, the rejection is highly due to size exclusion mechanisms. With PES 30 kDa, BSA adsorption is less significant as indicated with high water

flux recovery. However, the single solute filtration results (cf. Table 7) reveal that further separation is not possible with RC and PES 30. PES 100 has high BSA adsorption and fouling tendency (cf. Section 5.7), leading to significant pore blocking, while fouling is low for the RC membrane. As also observed in earlier studies [186], separation performance of PES UF membrane is compromised not only by loss of flux but also by loss of selectivity due to protein fouling. This is related to hydrophobic interactions and surface roughness (cf. Figure 15) in comparison to RC 100 kDa. Another contribution for the complete BSA rejection with PES 100 could also be related to the mild filtration conditions like low flux, and pH strength. Here the phosphate buffer concentration was diluted to 20 mM and no additional ionic strength e.g. NaCl was added that could cause protein salting out effects. In contrast, significant protein transmission in combination with quantitative rejection for silica (as single substances), as well as high water flux recovery, suggest that membrane RC 100 could be used for the ultrafiltration separation of BSA from the silica nanoparticles. Therefore experiments were further performed with RC 100 (cf. section 5.11), H_{gel}F-PES 300 (cf. section 5.10) in comparison with PES membranes.

5.10 Model solute UF with hydrogel-functionalized PES in comparison with base PES

Here, model solute UF with hydrogel-functionalized PES 300 membrane in comparison with base PES membrane are presented. In addition to the studies carried out in section 5.7.2, rejection studies were also carried out with hydrogel-functionalized PES membrane. The H_{gel}F-PES 300 fractionation performance as well as its antifouling resistance will be key for further separation and purification studies. Ultrafiltration results for silica at different pH values for the hydrogel-functionalized PES membrane in comparison with its base membrane and the PES 100 membrane (having the same molecular weight cut-off like the hydrogel-PES membrane; (cf. Table 5) are shown in Table 8.

Table 8: Silica rejection and flux recovery with hydrogel-functionalized PES compared to the two other PES membranes at pH 8 and 12 with solution/dispersion concentration of 0.2 g/L, initial flux ~50 L/m²h.

Silica rejection (%)						
	PES 300 kDa		PES 100 kDa		Modified PES 300 kDa	
	AAS	Fl. Spec.	AAS	Fl. Spec.	AAS	Fl. Spec.
pH 8	93 ± 2	92 ± 5	99 ± 0.5	96 ± 1	99 ± 1	99 ± 1
pH 12	88 ± 1	40 ± 2	99 ± 0.5	93 ± 6	99 ± 1	99 ± 1
Flux recovery (%)						
pH 8	91 ± 2		79 ± 2		94 ± 3	
pH 12	98 ± 1		76 ± 5		99 ± 1	

In general, the negative membrane surface charge and the silica particle's negative surfaces played a significant role for the observed high rejections. This is particularly true for results of membrane PES 300 at pH 8 were low rejection was expected considering its high MWCO. However, the case is different for this membrane at pH 12, where significantly higher transmission of silica had been observed.

It is suggested that some dissolution of silica under these alkaline conditions occurs, which causes permeation of silica across the membrane barrier, thus lowering observed rejection. The only partial dissolution can be related to the relatively low NaOH concentration or a less reactive form of the used silica. Moreover, the difference in rejection observed with "fluorescence" could be linked with the particle scattering effect. At this pH, the signal intensity was found to be decreased.

For PES 100 membrane, rejection was almost quantitative, in line with the much smaller barrier pore size, and no clear effects of pH value were observed. The hydrogel-functionalized PES membrane showed high silica rejections of ≥ 99 % at pH 8 and 12. The high rejection is mostly due to size exclusion and the repulsive interactions of both solute and the grafted membrane surface. In addition, reduced permeability was experienced

during filtration at pH 12. These effects can be ascribed firstly to the structural changes from a more amphoteric (positive and negative) to a polyanionic (only negative) hydrogel. At low salt concentration, the latter (polyanion) will be more swollen than the first (amphoteric) state. The resulting electrostatic repulsion among the negative charge groups causes the extension of the grafted AMPS chains which blocks the pore of the membranes.

Secondly, the low permeability observed during filtration at pH 12 could also be partly linked to solution viscosity. For example, the membrane permeability for modified PES 300 membrane at pH 8 and 12 are 54 ± 1 and 17 ± 0.8 respectively. The viscosity effect correlates with differences in ion mobility which was deduced from conductivity measurement with the same ionic strength of 20 mM. The conductivity at pH 8 and 12 are 3.22 and 1.24 mS/cm.

The water flux recovery for the modified PES membrane showed better performance over the PES 100 (cf. Table 8). The large MWCO of the PES 300 base membrane may have compensated for similar water recovery in comparison to the modified PES 300.

The single solute rejection data for BSA and the second studied model protein LYS at different pH values with hydrogel-functionalized PES membrane and the two PES membranes is shown in Figure 38.

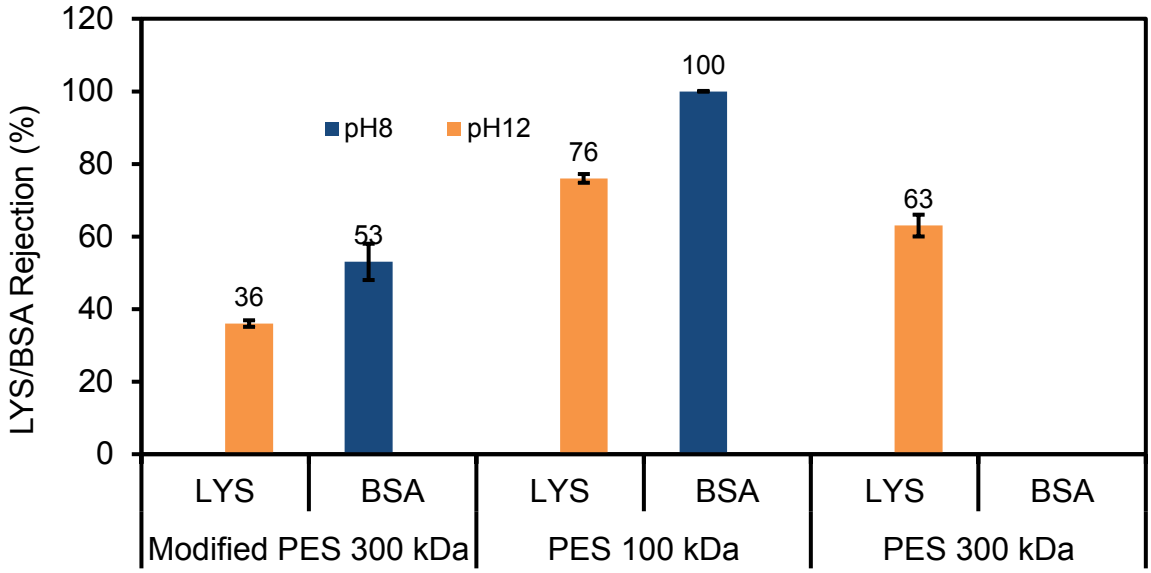

Figure 38: Single BSA and LYS rejection; protein concentration 0.2 g/L, pH 8 or 12; initial flux 50 L/m²h.

The larger BSA (IEP 4.9) has a modest negative charge at pH 8 while the smaller LYS at pH 12 is relatively close to its IEP (11.0). The hydrogel-functionalized PES membrane had the lowest protein rejection compared to the other ones, the value with LYS at pH 12 (36 %) was the lowest. Aside the small molecular weight of LYS, the high transmission was enhanced through the hydrophilicity of the grafted hydrogel layer. This had minimized surface and pore wall adsorption due to the high repulsive net negative charge of LYS above IEP and the membrane surface charge. The diffusion coefficient for LYS which has been earlier reported to be larger than BSA increases with intermolecular repulsion aiding LYS transmission [187, 188].

The water flux recovery showed improved performance for hydrogel-functionalized PES membrane. For example, at pH 12 (LYS) and pH 8 (BSA) the modified membrane water recovery were 98 and 91 %, while for base PES 100 yielded 49 and 70 % water recovery at pH 12 and 8 respectively. LYS fouling was less significant with the modified in comparison to PES 300 base membrane, which was significantly prone to adsorption with the attended

higher rejection. The membrane surface adsorption and size exclusion are the reasons for the highest rejection observed with PES 100 at pH 12. In addition Figure 38 and Table 8 shows that PES 300 membranes showed no useful selectivity as both LYS and silica were transmitted across the membrane. And use of PES 100 membrane for fractionation was impossible for BSA from silica because of observed 100 % rejection for both colloids (in line with single colloid data) while the selectivity for LYS removal was much lower than for the hydrogel-functionalized PES membrane. The rejection of BSA with hydrogel-functionalized PES membrane at pH 8 was 53 %, a value even lower than for the RC membrane (58 %; cf. Table 7). Hence, for both low-fouling membranes, based on single colloid rejection results separation of the model proteins from silica dispersion should be feasible.

5.11 Separation performance for mixed (compared to single) solutes

The results from section 5.9 and section 5.10 clearly show that RC 100 and hydrogel-functionalized PES has better fractionation/selectivity as well as antifouling resistance, thus further separation will be focused on the above mentioned membrane. The selection of solution pH values of 8 or 12, for BSA or LYS, respectively, was necessary for stable dispersions without agglomeration between the two different colloids. The IEP values of both proteins are lower at these pH values (cf. Table 6). The resultant net negative surface charge leads to repulsive interactions with silica nanoparticles which are also negatively charged at both pH values. It is important to mention again that all membrane types possess negative surface charge at these solution pH values. The rejections for the components of the mixed colloid systems (LYS/silica and BSA/silica) for the RC and hydrogel PES membranes are depicted in Figure 39.

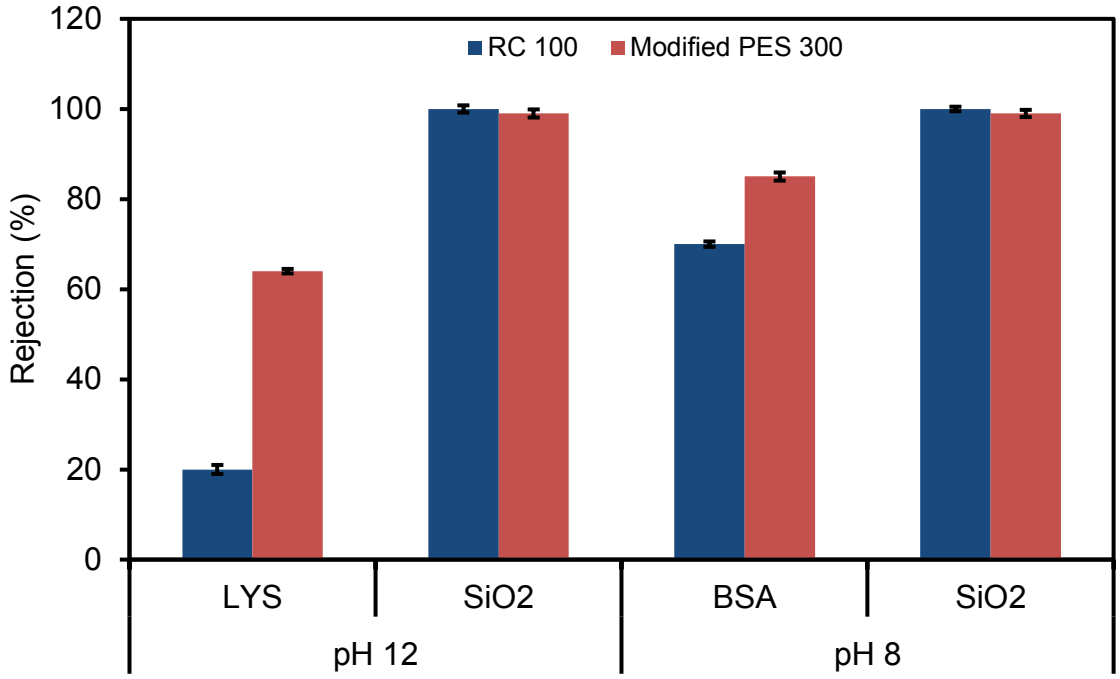

Figure 39: Mixture ultrafiltration with RC 100 membrane and hydrogel-modified PES; pH 12 (LYS/silica mixture) pH 8 (BSA/silica mixture); total colloid concentration 0.4 g/L, phosphate buffer pH 8; initial flux ~ 50 L/m²h.

For both membranes, silica rejection had been quantitative and ≥ 99 % selectivity. For the RC membranes, the LYS rejection in the mixture (LYS/silica) was slightly higher compared to single LYS ultrafiltration. The former observation may have been due to additional hindrance by silica in the mixture, but more important the very high protein transmissions were due to low fouling property of the RC membrane and the much smaller size of LYS (5 nm from DLS; cf. Table 6) and compared to membrane barrier pore size (15 nm; cf. Table 5). The larger size of BSA (5 nm from DLS; cf. Table 6) and the competitive influence of the second colloid (silica) were crucial for the higher rejection observed with BSA in the mixture (70 %) compared to single protein ultrafiltration. Concentration polarization layer of rejected silica seemed to hinder the transmission of the protein significantly. More importantly, the water flux recovery followed single filtration of BSA and silica with 99 % water flux recovery (cf. Table 7). The increase in protein rejection was more pronounced in both cases (LYS and BSA) for the hydrogel-functionalized PES membrane. This could be related to a somewhat

stronger fouling tendency compared to the RC membrane. However, the water flux recovery after the colloid mixture ultrafiltration showed marked improvement over unmodified PES membrane (cf. Figure 40). The water flux recovery values (cf. Figure 40) with hydrogel-functionalized PES membrane for LYS/silica or BSA/silica were 99 or 80 % respectively.

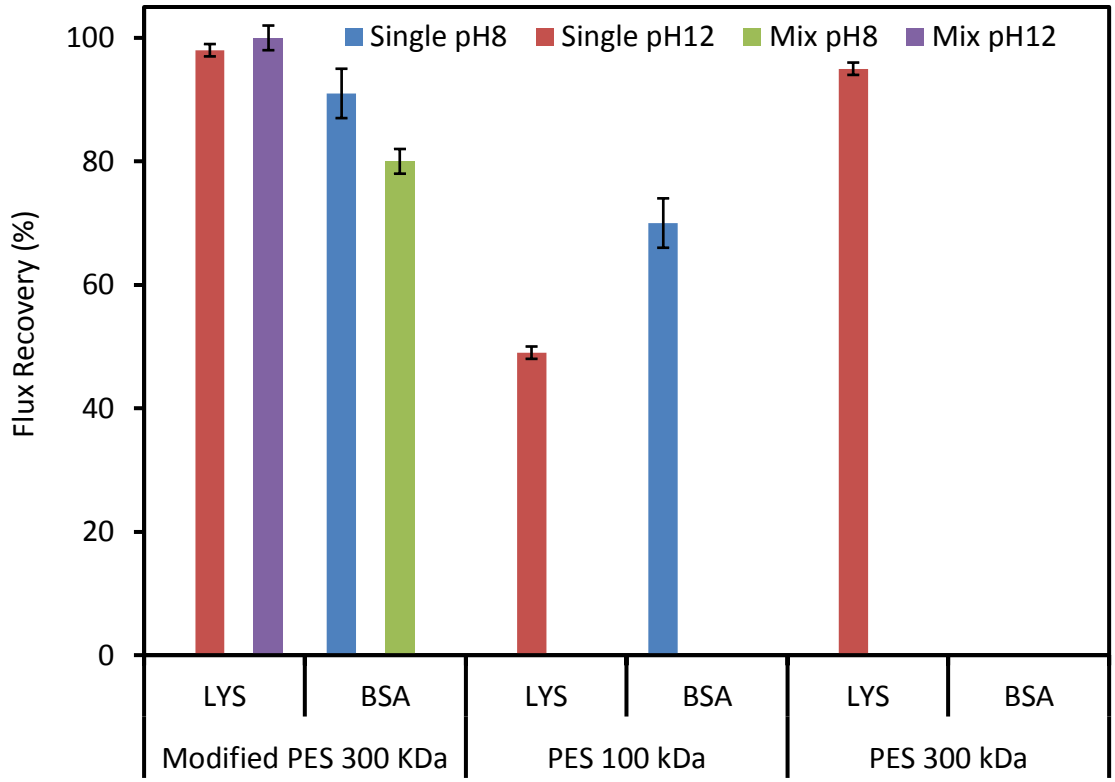

Figure 40: Water flux recovery for the mixtures in comparison to single solute filtration: Single BSA, LYS with protein concentration 0.2 g/L, pH 8 or 12); and pH 8 (BSA/silica mixture); pH 12 (LYS/silica mixture) with total colloid concentration 0.4 g/L, phosphate buffer pH 8; initial flux ~ 50 L/m²h.

This is another proof for successful and functional suitability of the grafted amphoteric hydrogel layer on PES ultrafiltration membranes. And fractionation seems possible for both LYS and BSA in the mixture, considering the transmission of 36 % and 15 %, respectively, in the batch dead end process. Because purification was not sufficient in a single batch ultrafiltration, continuous diafiltration should be employed for further purification of LYS and BSA from the mixture with silica. Using equation (4.22) (cf. Section 4.7.6) and based on

protein rejection from batch ultrafiltration of the mixtures (cf. Figure 39), theoretical number of diafiltration volumes (DV) to obtain ≥ 99.7 % removal from mixtures with silica was 6 for LYS and 10 for BSA for the RC 100 membrane. Likewise, for the hydrogel-functionalized PES membrane the theoretical removal using 6 and 10 DV for BSA and LYS were 89 and 78 % respectively. This calculated theoretical DV numbers was used as reference during purification with diafiltration (see Section 5.12). It is clear from Figure 39 that RC membrane has higher protein transmission compared to the hydrogel-functionalized PES membrane.

5.12 Diafiltration for colloid mixture separation

Since intrinsic sieving, i.e. the significant passing of BSA or LYS through the membrane to the permeate stream, have been achieved with RC 100 and hydrogel-functionalized PES membrane, further separation step is needed for complete protein removal. Here, the diafiltration (DF) which is most often used to exchange product into a desired buffer (e.g., from an elution buffer into a final formulation buffer) was employed for purification. The diafiltration option is suitable because of its additional washing buffer configuration (cf. Figure 7).

RC 100 and hydrogel-functionalized PES membrane with similar MWCO (cf. Table 5) were evaluated, because unmodified PES membranes were expected to be not suitable based on the previous results. The colloid mixture which was pH stabilized (cf. Section 5.5) and contained a total colloid concentration of 0.4 g/L and a 1:1 ratio between protein and silica. A feed volume of 10 mL was diafiltered at constant retentate volume by continuously dosing the buffer solution. The content of silica nanoparticles was expected to remain constant and the one of protein to be decreasing. The flux was maintained at ~50 L/m²h, because of the low-fouling properties of the membranes and the subcritical flux conditions, this was

possible at constant transmembrane pressure. Permeate and retentate concentrations were determined using AAS for silica and BCA assay for the proteins.

The purification of LYS and BSA from their mixtures with silica nanoparticle dispersions at solution values pH 12 and 8, respectively, for RC 100 and hydrogel-functionalized PES membrane is presented in Figure 41 and Figure 42, respectively. Using membrane RC 100, the removal of LYS from the mixture with buffer solution of pH 12 was 91.4 % with 6 diafiltration volumes within a total time of 2.4 h. This corresponds to 1.84 mg protein from the 10 mL feed containing 2.0 mg of LYS using 6 DV equivalent to 60 mL of buffer.

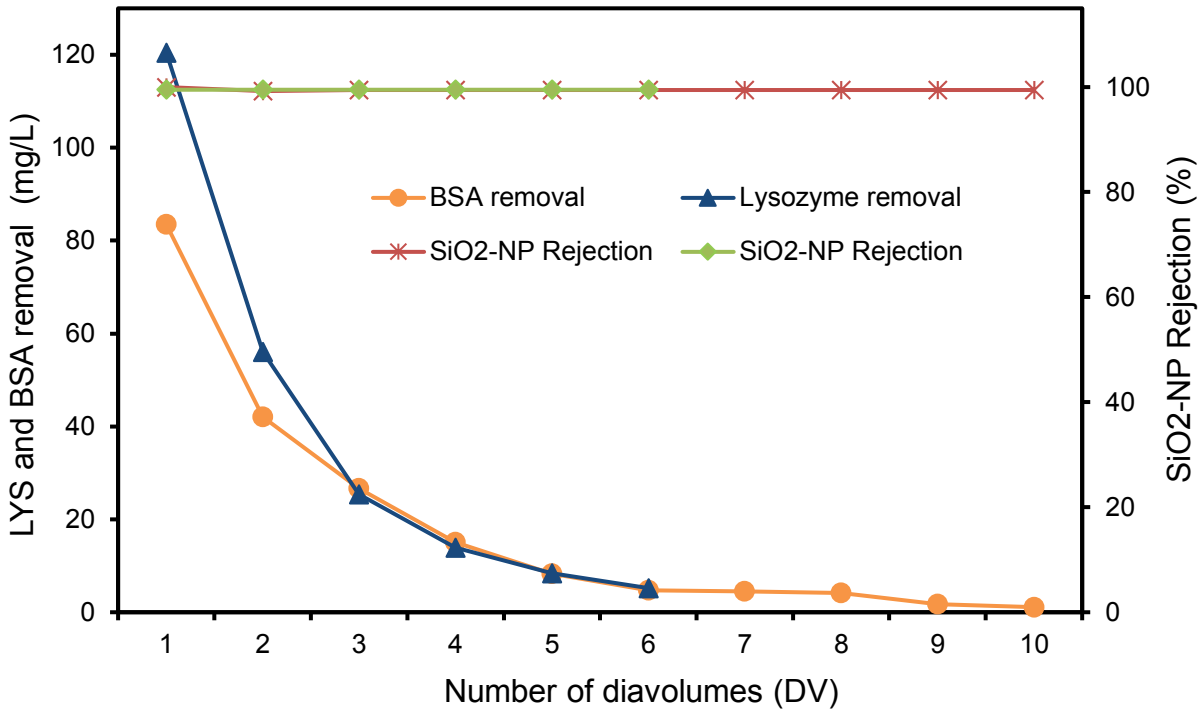

Figure 41: Continuous diafiltration with RC 100 membrane for purification of BSA and LYS from mixtures of BSA/silica and LYS/silica; total colloid concentration 400 mg/L (1:1 wt. ratio protein/silica), at pH 8 and 12; initial feed volume of 10 mL; flux ~ 50 L/m²h; protein removal expressed as permeate concentration.

BSA removal with buffer solution of pH 8 was 84 % using 10 DV within 5.5 h. This amounted to 1.68 mg from the feed of 2.0 mg. For both cases, silica rejection was ≥ 99 %. The presence of silica, inducing concentration polarization, has obviously reduced the efficiency and

caused incomplete removal of LYS and BSA in comparison with the theoretical value of 99.7 % (cf. Section 5.11). It is important to note that the theoretical removal was calculated based on the assumption of constant transmission (that is without CP and fouling). This in reality is challenging with mixture dispersions due to CP of the rejected SiO_2-NP, possible adsorption and the non-recycling of the retentate stream. The purity which was determined by the amount of protein left in the retentate was 95 % and 96 %, after removal of LYS (pH 12) and BSA (pH 8), respectively. The relationship below was used to estimate the mass loss:

$$m_F = m_P + m_R + m_{loss} \qquad (5.23$$

Where the masses m_i correspond to feed (F), permeate (P), retentate (R) and lost mass (loss). The loss mass yielded 4.4 % (i.e. 8.7 mg/L) for BSA and 0.4 % (i.e. 1.23 mg/L) for LYS.

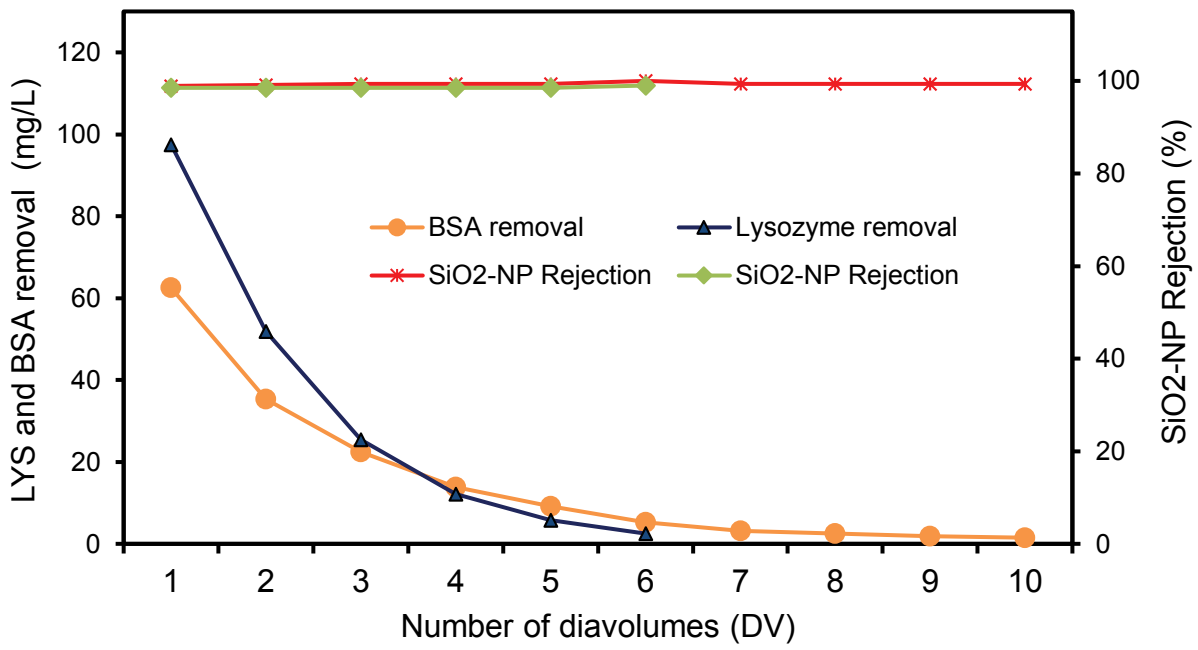

Figure 42: Continuous diafiltration with hydrogel modified PES for the purification of BSA and LYS from mixtures of BSA/silica and LYS/silica; total solute concentration is 400 mg/L (1:1 wt. ratio protein/silica), at pH 8 and 12; initial feed volume of 10 mL; flux ~ 50 L/m²h; protein removal expressed as permeate concentration.

The hydrogel-functionalized PES membrane with buffer solution of pH 12 has shown 82 % LYS removal from the feed mixture using 6 DV within 4 h. This corresponds to 1.64 mg from the 10 mL feed containing 2.0 mg of LYS. 1.50 mg of BSA was washed to the permeate side with buffer solution of pH 8 using 12 DV within 6.8 h. The silica NP purity after diafiltration was 90 % at solution pH 12 and ≥ 99 % at solution pH 8.

The high purity may be due to protein adsorption to the membrane surface as the purity calculation was based on the amount of protein detected to be left in the retentate after purification. This could be linked to the indications of more pronounced fouling compared to the RC membrane, obtained from the mixture ultrafiltrations experiments (cf. Section 5.10). The loss yielded 10.5 % (i.e. 20.8 mg/L) for BSA and 4.4 % (i.e. 12.3 mg/L) for LYS, thus substantiating the less fouling superiority of the RC 100 membrane.

Comparing all results, especially the ones for the solution pH 8 which may be more attractive to industrial application, RC 100 showed more protein removal and less diafiltration time compared to the hydrogel-functionalized PES membrane. However the latter membrane type which is expected to be more stable than RC has also significant potential; and using this will be addressed by further optimization of the surface functionalization. A fine adjustment of the sieving properties and the membrane permeability as well as incorporating stability to the modified membranes can be enhanced by addition of suited crosslinker monomers in appropriate ratio to the reaction mixture. An example is a hydrophilic cross-linker, N, N'-methylenbisacrylamide (MBAA), which can as well improve the fouling resistance via reducing the membrane−solute interactions. We envisage that, when MBAA is added, the poly/DMAPAA/AMPS chains get simultaneously crosslinked during their growth. Thus, grafted hydrogels crosslinked with MBAA will exhibit much tighter structure. In addition the use of cross-linker will promote size exclusion effect

of solute from the membrane surface and as a result we can expect that the solute (e.g., protein) will not easily reach the substrate surface to be adsorbed.

5.13 Gold-peptide separation by ultrafiltration

In this part purification of gold-peptide conjugates from excess unbound peptide using RC 30 and 100 kDa UF membranes were investigated. Here the successful purification of BSA and LYS (cf. Section 5.11) from silica mixtures is applied to gold-peptide dispersion. The particles sizes include: mean gold nanoparticle ~ 5.2 ± 1.2 nm (by TEM), peptide ~ 4 nm (by DLS), and bioconjugated gold nanoparticle ~ 8.5 nm (by DLS). The main sub-parts include:

i) Colloid stability and best suitable ultrafiltration conditions,

ii) Single solute gold and peptide UF rejection studies,

iii) Purification of gold nanoparticle peptide bioconjugates using DF, and

iv) Comparison of UF to centrifugal filtration.

5.13.1 Peptide and gold colloid stability and ultrafiltration conditions

In order to perform successful ultrafiltration with maximum separation selectivity, the interactions with the membrane must be understood and the stability of the peptide and gold colloid solution must be retained. Therefore, the stability of peptide solution and gold (80 µg/mL) colloids were evaluated in different concentrations of sodium phosphate buffers at pH 8 in the range of 0.1-100 mM. Increasing buffer concentration leads to presence of counter ions which can cause reduction of repulsive particles-particle and peptide-peptide interactions by charge screening. Samples were ultrafiltered using RC 100 kDa membrane. The flux of about 50 L/m^{2}h was also employed here too with the intention to operate below the critical flux. Representative results for filtration of peptide solutions are shown in Figure 43. All flux data recorded during separate filtration of both solutes/colloids and water fluxes before and after ultrafiltration reveal no significant fouling effects. The flux during peptide

filtration seemed to decrease slightly with increasing salt concentration, but this effect is not significant due to relatively large statistical error.

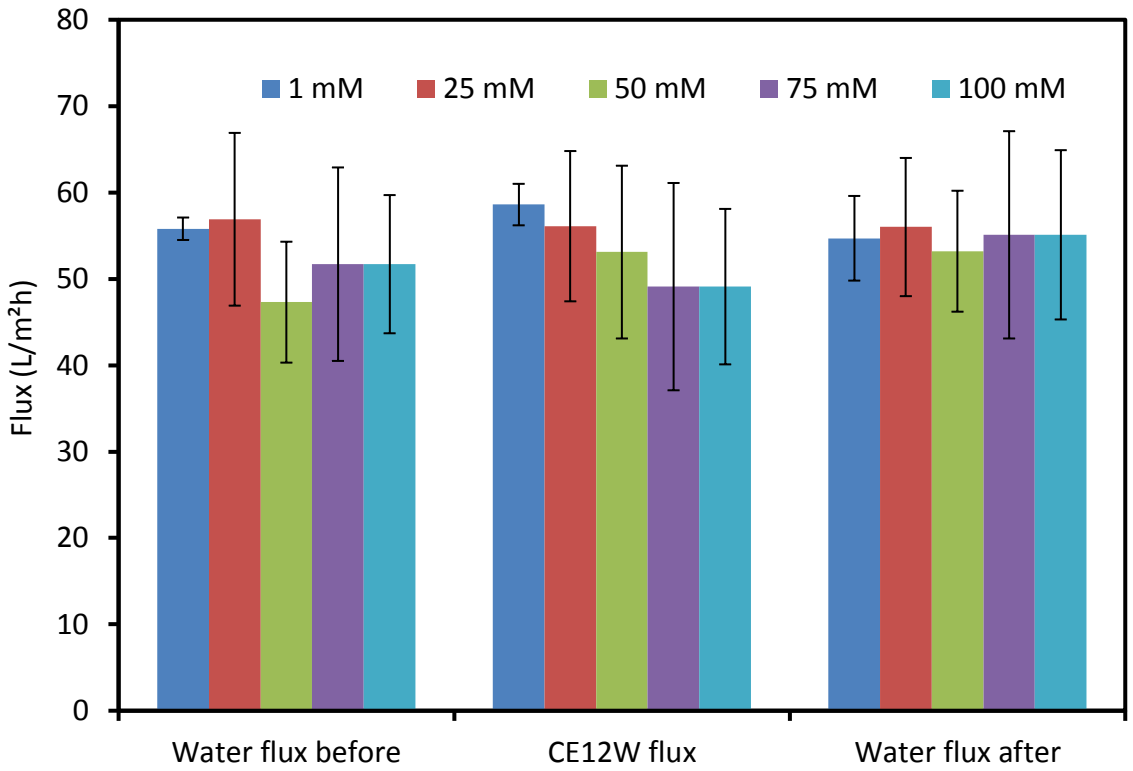

Figure 43: Ultrafiltration of peptide ($CE_{12}W$ without AuNP) at pH 8.0 and different salt concentrations (membrane RC 100 kDa; trans-membrane pressure 0.15 bar). Additionally, the flux of water before and after the respective peptide filtration is shown.

The rejection during peptide filtration with different salt concentrations is shown in Figure 44. The decreasing peptide rejection with increasing ionic strength may be due to the presence of counter ions which screen negative charges of the membrane and the peptide [189]. This phenomenon is caused by less peptide hydration and solubility as salt concentration increases, inducing shrinking hydration layer dimension and solute size and consequently increasing transmission through the membrane.

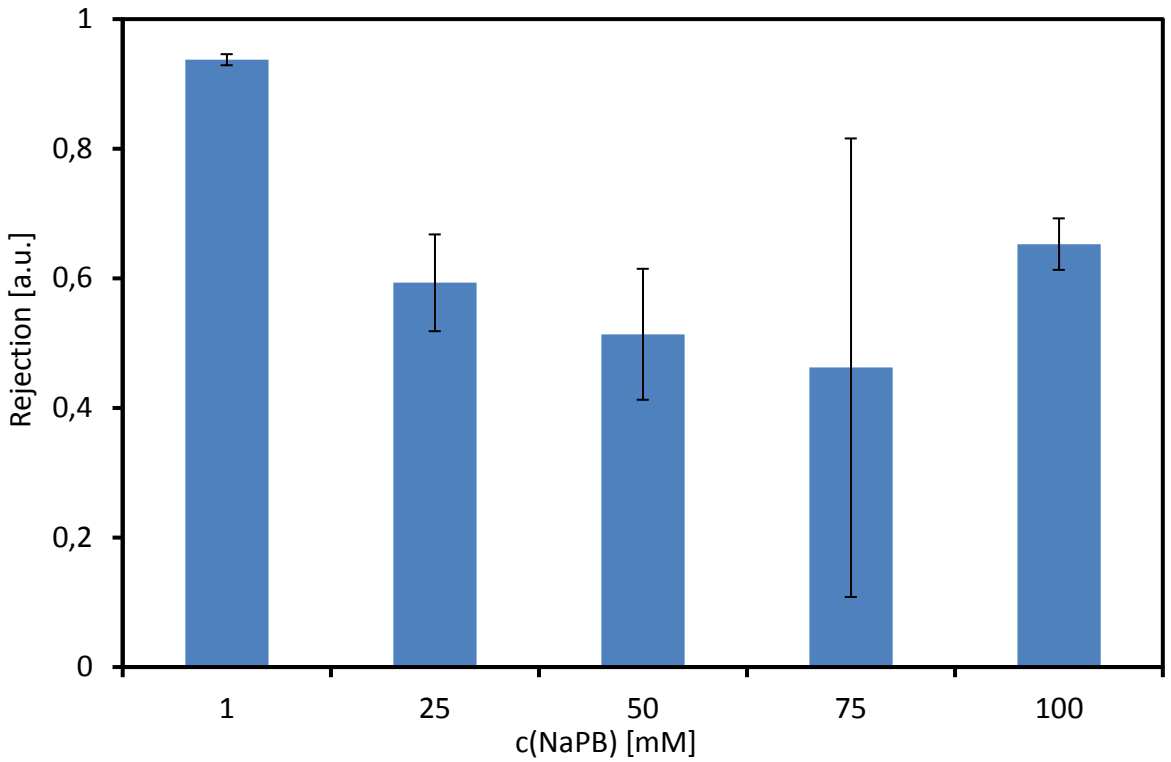

Figure 44: Rejection of the peptide ($CE_{12}W$ without AuNP) during the single solute ultrafiltration at different concentrations of sodium phosphate buffer from 1.0 – 100 mM (membrane RC 100 kDa, 0.15 bar; cf. Figure 43).

Figure 44 also revealed a critical salt concentration that reverses this trend. The increase in rejection after 75 mM could be caused by peptide precipitation, thus decreasing transmission through the membrane. The best-suited salinity for the peptide was chosen to be 50 mM because of the large error of data at 75 mM (cf. Figure 44). At this salinity, the transmission of unbound free peptides should be close to the maximum. Considering the barrier layer pore size estimated for RC 100 kDa membrane (cf. Table 5), it is highly probable that the observed negative zeta potential of the membrane (cf. Section 5.2.4) contributes to the rejection of the also negatively charged peptide (having a size of only 3-4 nm). Many examples for ultrafiltration membranes exploiting the combination of size- and charge-based selectivity in a dedicated way have been reported [190]. Hence, the decrease of rejection with increasing salt concentration in this study (cf. Figure 44) could also be caused by the reduced contribution of Donnan exclusion to rejection. Similar filtration conditions (cf.

Figure 44) were also applied for gold nanoparticles using salt concentrations ranging from 0.1 mM to 5 mM yielding a 100 % rejection for each condition. The convective transport of AuNP to the membrane surface seemed to form a porous polarized layer that had only minimal impact on the flux. However, the peptide-free AuNP became colloidal unstable and precipitated at salinities greater than 1 mM; hence no further tests were conducted for AuNP above this concentration. The water flux recovery of 98 ± 2 % (deduced from water flux after vs. before colloid filtration; cf. Figure 44) was identical for both AuNP and peptide ultrafiltrations. This already indicated that the RC membrane may be well suited for the intended separations.

5.13.2 Single solute gold nanoparticle and peptide ultrafiltration

Single solute gold nanoparticle and peptide ultrafiltration at varied pH value and with two different membranes are presented here. Ultrafiltration using stirred dead end cell was used to test the rejection of single solute of gold and peptide (80 µg/mL), using RC 100 kDa membrane, the single solute filtration of gold nanoparticles and peptide molecules at different pH values (pH 4, 5, and 8) carried out with a buffer concentration of 1 mM where naked gold nanoparticles were still electrostatically stabilized revealed little or no flux decline or water permeability loss during or after the ultrafiltration, respectively. This membrane was also tested to assess the individual selectivity for both AuNP and peptide during UF and depicted in Figure 45.

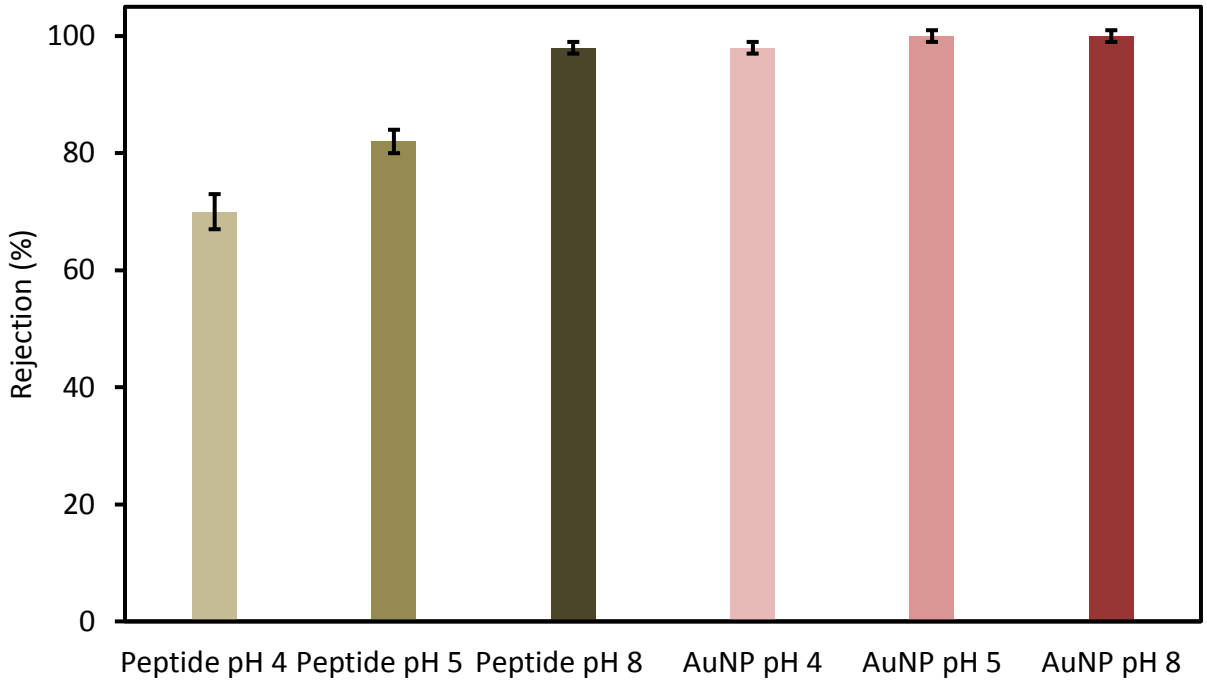

Figure 45: Rejection of the peptide ($CE_{12}W$) and AuNP (both with 1 mM NaPB) during the single solute ultrafiltration at different pH values (RC 100 kDa, 0.15 bar, ~ 50 L/m^{2}h).

Results for a representative, stepwise UF process are shown in Figure 46. The very good performance, in the pH range from 4 to 8, is obtained because of the chosen relatively low flux of ~ 50 L/m²h and of the well-known low fouling characteristics of RC membranes.

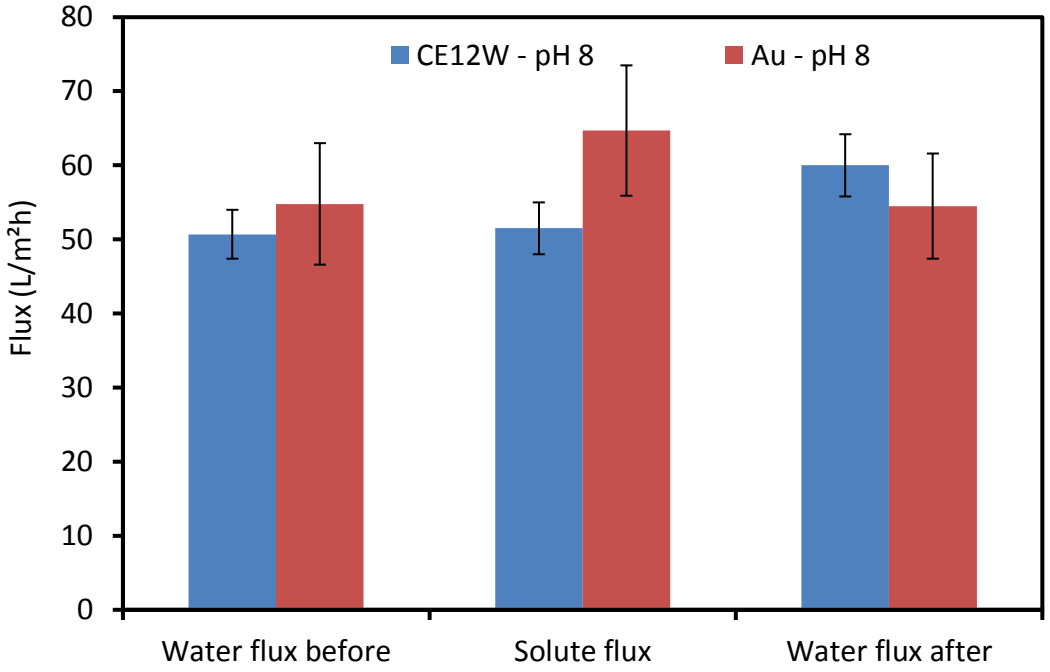

Figure 46: Representative data for ultrafiltration of single solute gold nanoparticle (without peptide) and peptide (without AuNP), here at pH 8 (membrane RC 100 kDa, 0.15 bar). Additionally, the flux of water before and after the respective solute filtration is shown.

Significant transmission for peptide (rejection 0.70) and gold nanoparticles (rejection 0.98) was observed at pH 4 (cf. Figure 45). Hence, at this pH value, about 2 % of AuNP (at a feed concentration of 80 µg/mL) was ultrafiltered through the RC 100 kDa membrane. This incomplete rejection is due to the barrier pore size of the UF membrane, as the average hydrodynamic diameter of AuNP according to DLS was 7 nm. At this low pH value which is close to the isoelectric point of the membrane (cf. Section 5.2.4), there is reduced electrostatic repulsion between the nanoparticle and the membrane surface. In this case, an initial deposition on the membrane surface is favorable thus enhancing transmission through permeation drag. On the other hand, strong double layer repulsion exists between retained gold nanoparticles and the approaching dispersed gold nanoparticles. Therefore the rejection is still rather high considering the estimated barrier pore size of 13 nm (cf. Section 5.3). The extent of colloidal gold triggered membrane fouling is hypothesized to depend on the interplay between double layer repulsion and permeation drag. Since a low UF flux has

been used, the double layer repulsion may overcome the opposing permeation drag, thus minimizing fouling as evidenced in a high water flux and recovery after the solute filtration.

At pH 8, the transmission of the peptide was reduced compared to the experiment at pH 4 (rejection 0.97; (cf. Figure 45)). No transmission of AuNP could be observed, but potential separation selectivity was obviously low. However, another important parameter was also strongly influenced by the pH value, the loss of gold nanoparticles when making up the mass balance of gold applied in the feed and gold found in permeate and retentate. At pH 4, this loss was of 85 % (feed 458 µg, found 70 µg), while for pH 8, the loss was only 35 % (feed 503 µg, found 325 µg). Obviously, pH 4 induces a destabilization of the nanoparticles. This was also confirmed by observation after ultrafiltration in the stirred cell: A much darker zone with deposit was found in the center of the membrane; an accumulation of particle agglomerates in the middle of the membrane had been obviously aided by the stirrer (see details in Appendix 8.3 (A.6)). Such effect was only very weakly seen at pH 8.

Figure 47 shows the rejection for peptide (salinity of 50 mM) and gold nanoparticles at pH 8 (salinity of 1 mM) with the membranes RC 100 kDa and RC 30 kDa. As both solutes and membranes are highly negatively charged, strong double layer repulsion forces exist between the particles and the membrane surface. The large negative zeta potential (cf. Section 5.2.4) played a role in the extent of particle deposition and subsequent particle aggregation on the membrane.

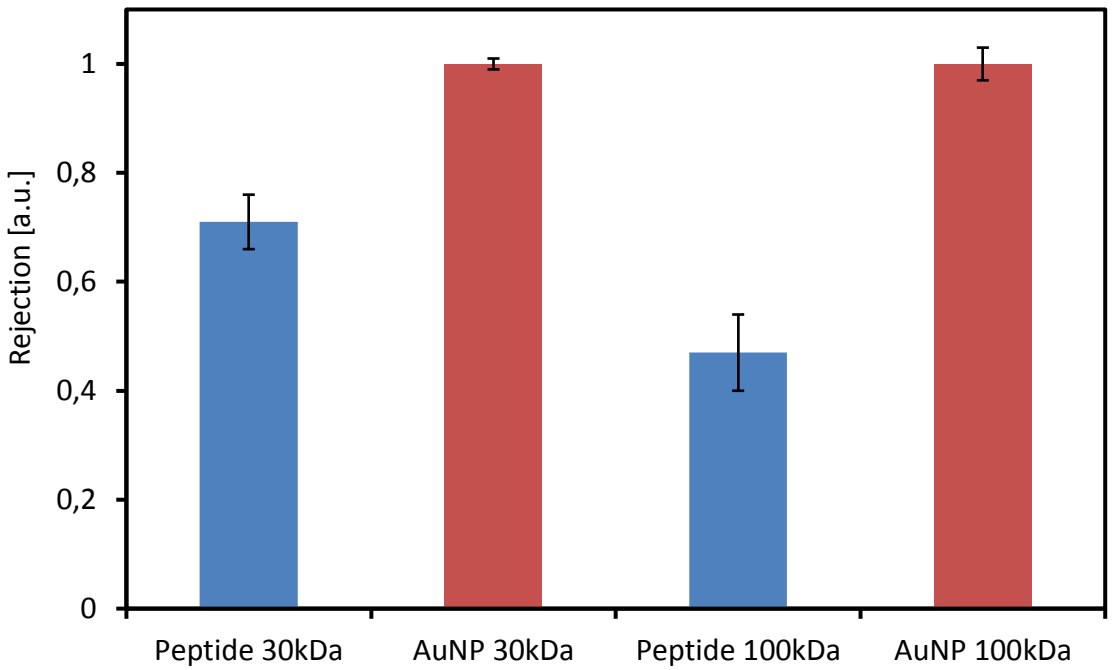

Figure 47: Representative ultrafiltration rejection data for single solute gold nanoparticle (without peptide) and peptide (without AuNP) filtration at pH 8 (0.15 bar, ~ 50 l/m^{2}h) with optimized salinity of 50 mM for the peptide for both RC membranes with different NMWCO.

This interplay between double layer repulsion coupled with the employed low permeate flux is depicted in the high rejection for gold nanoparticle and the low fouling tendency (cf. Figure 44 and Figure 46). For the peptide rejection, the permeation drag, the salting out effect which can result in double layer compression as well as the UF sieving properties contributed to peptide transmission across the membrane. However, the relatively low peptide transmission indicates that a multi-step process will be needed for purifying mixtures containing peptides and AuNP bioconjugates.

5.14 Purification of gold nanoparticle-peptide bioconjugates using diafiltration

The purification of gold nanoparticle bioconjugates (average hydrodynamic diameter of 8.5 nm measured by dynamic light scattering) using semi-continuous diafiltration at pH values 4, 5 and 8 was studied. It is important to mention that the salinity test (cf. Section 5.13.1) which was only done for the optimization of UF parameters has no significant effect on the colloidal stability of the bioconjugated gold nanoparticles dispersion. According to mass balance, there was a high loss of the bioconjugate product AuNP-$CE_{12}W$ at pH 4 and 5 using three diafiltration volumes with membrane RC 100 kDa. For the bioconjugate, the loss at pH 4 was 85 % (feed 200 µg, found 31 µg). At pH 5, there was a loss of 75 % (feed 200 µg, found 51 µg). Further reasons for the high loss including those already stated (cf. Section 5.13.2) could be unstable bioconjugated gold nanoparticles, and the screening of the repulsive double layer leading to high adsorption and aggregation. The reduced peptide's net-charge at lower pH, which was already determined yielded -1 and -5 at pH 4 and 5, respectively, also contributes to the higher loss. In comparison, the net charge of the ligand at pH 8 is -12 which is much higher electrostatically stabilizing AuNP. This means that the peptides at pH 4 and 5 are not totally extended and the electrostatic repulsion is much lower compared to pH 8. On the other hand, AuNP bioconconjugates can be transmitted through the membrane (for example at pH 5, 36 µg conjugated gold nanoparticles from 200 µg in the feed passed the membrane) because they are more stable than the naked AuNP and less interaction with the functional groups of the RC membranes are established. These high losses and transmissions of gold nanoparticle bioconjugates at low pH, which is similar to the results obtained for naked nanoparticles (but without fouling), directed further experiments continued at pH 8. The diafiltration results from bioconjugated NP prepared (AuNP: 20

µg/mL, $CE_{12}W$: 20 µM, NaPB: 40 mM) with RC 100 kDa membrane and three diafiltration volumes indicated a transmission of 10.1 ± 1.6 % (20.3 µg ± 2.6 µg) of the bioconjugate per diafiltration volume.

Although the $CE_{12}W$ peptide carries a tryptophan exhibiting an UV absorbance at 278 nm, it is not possible to quantify the amount of bound ligands in the presence of gold nanoparticles because of the interband absorbance of AuNP interfering with the peptide peak in the UV range. This scenario together with the high dilution during permeation reaching concentrations close to limit of detection made it difficult to quantify the unbound ligands in the permeate. Although the free peptide showed promising removal with RC 100 kDa (cf. 5.12.2), the unavoidable transmission of bioconjugated NP complicates the interpretation of the results. The permeation can be related to changes in surface properties of the bioconjugated NP which affects interactions with the membrane. Compared to the results with naked gold nanoparticles, where they were found to adhere to the membrane surface, the conjugated particles are more stable and less repulsive and therefore can pass the pores of a 100 kDa membrane. To eliminate the AuNP transmission problem, the RC 30 kDa membrane was used aiming at improving the bioconjugate rejection due to smaller pores (Additional SEM images of RC 100 and RC 30 kDa are provided in Appendix 8.5 (A.10)). The flux during the diafiltration is shown in Figure 48.

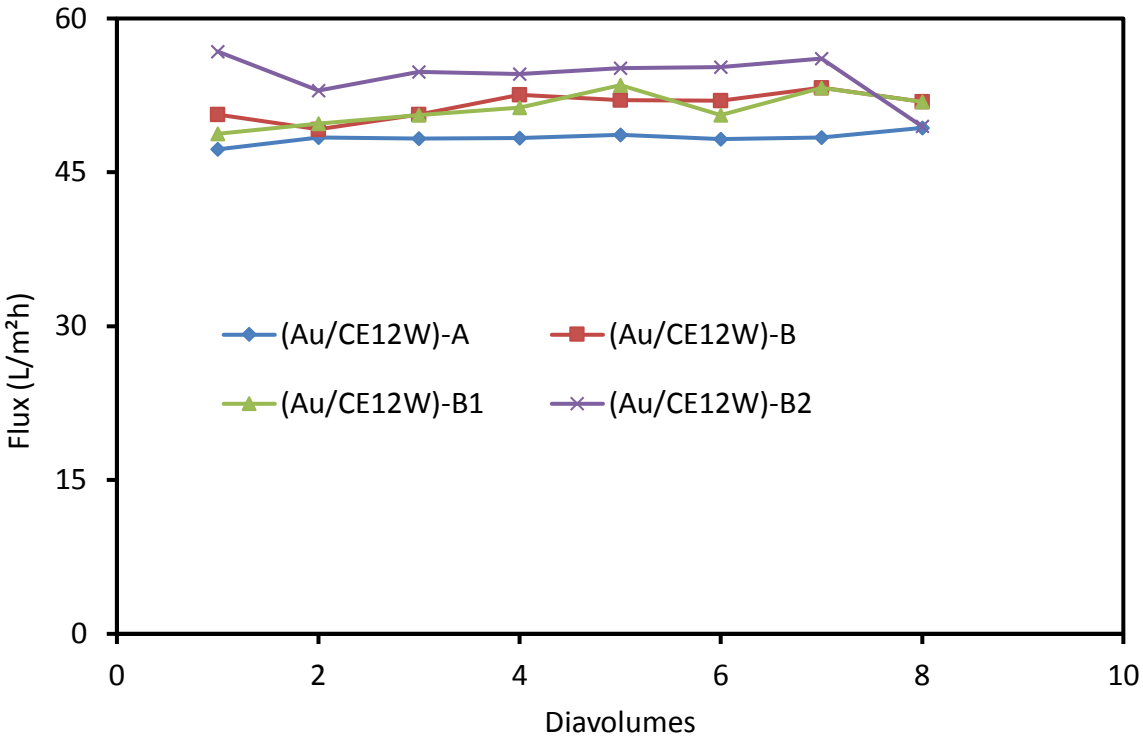

Figure 48: Flux data during the purification experiments of AuNP-peptide bioconjugates: "A" indicates single use of membrane sample; "B" indicates new membrane sample; "B1" & "B2": same membrane sample as "B" (RC 30 kDa, 0.35 bar, ~ 50 L/m^{2}h). The first and the last points correspond to the water fluxes before and after semi-continous diafiltration.

The membrane samples A, B and the reused samples B1 and B2 showed no flux loss. Aside the many contributing factors, i.e. filtration conditions (low transmembrane pressure, low flux; cf. Section 5.13.1), and membrane characteristics as shown by zeta potential and contact angle (cf. Sections 5.2.3, 5.2.4), the semi-continuous diaflitration mode also played a significant role with respect to the stable flux during the purification process. The stopping of the filtration in order to refill the diafiltration buffer allows for relaxation and or removal of the concentration polarization layer. Also the low flux used enabled fast relaxation and redispersion of any concentration polarization layer formed which can be traced to stabilizing electrostatic interactions between the particles. It can be envisioned that the particles remained as individual entities in the CP layer because of the low concentration and are also kept apart due to double layer repulsion. Resumption of the diafiltration process

caused reorganization of the concentration polarization and/or deposition on the membrane surface thus repeating the cycle. In addition, pore blocking is not significant because of the differences on the shape and the relative size of the particles and pores.

Another additional reason is the fact that greater amount of the separation was achieved in the first three diafiltration cycle (cf. Figure 50), hence separation load subsequently decreases with increasing number of diafiltration volume.

The UF sieving mechanism is used to wash out the free ligands from the bioconjugate colloid. As the free peptide ligands migrate toward the membrane surface by convective process they are transmitted through the membrane because they are: (1) small enough to pass and (2) adsorption does not happen quickly or strongly enough [191]. As indicated by Fane et al., particles not held in a structured layer could flow tangentially across the membrane if subjected to adequate shear, or could permeate based on the mentioned conditions.

The loss of bioconjugated gold NP compared to the number of usages of the membrane and the ultrafiltration efficiency for unbound peptide after six diafiltration volumes is summarized in Table 9.

Table 9: Bioconjugated gold nanoparticle loss and free peptide removal efficiency with RC 30 kDa membrane after 6 diafiltration volumes

Membrane sample	Bioconjugated AuNP loss (%)	Peptide removal (%)
A	17.7	53.9
B	17.2	59.1
B1	14.6	68.4
B2	11.7	62.2

The results indicate that the loss of bioconjugated gold nanoparticles during the six diavolumes becomes lower when the membrane is used several times. However, the filtration efficiency of the peptide molecules shows no influence with respect to the reuse of

the membrane. This could be due to some adsorption on the surfaces of both the filtration cell and the membrane material. The UV-Vis spectra to determine the feed, retentate and permeate concentrations are shown in Figure 49. The amount of peptide ligands was determined via absorbance at 278 nm and the one of gold in bioconjugated AuNP at 380 nm, respectively. As targeted by the experiment, there was no gold nanoparticle bioconjugate peak in the permeate, so that it could be concluded that it contained only unbound free ligands. This is in line with the expectation that the membrane RC 30 kDa should definitely reject the nanoparticles, completely (cf. Figure 47).

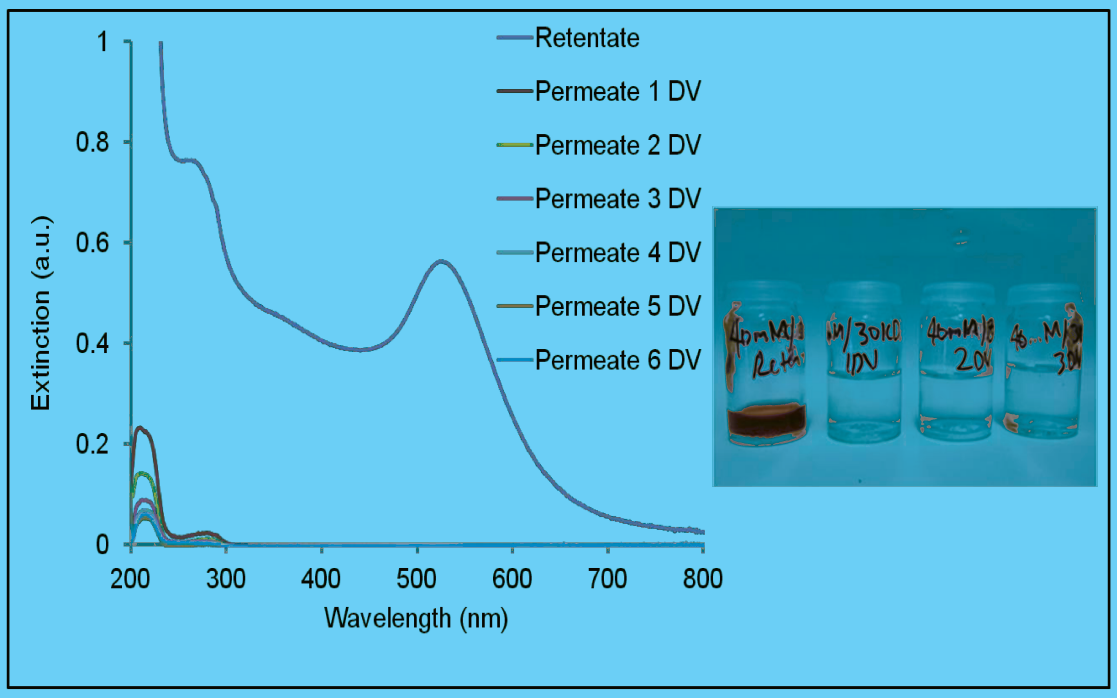

Figure 49: UV-Vis spectra to determine the feed, retentate and permeate concentrations during diafiltration. Peak in UV range corresponds to the peptide, and peak at ~ 520 nm to the gold. Inset: Picture of retentate (first to the left) and permeate (right) samples.

The summary of the bioconjugated AuNP purification efficiency with respect to the removal of unbound peptide in each filtration step is presented in Figure 50. The data show the average of four experiments, with the standard deviation, obtained with the membranes also mentioned in Table 9. The minimum displayed value is 3.1 % of initial $CE_{12}W$ in the

permeate per diavolume. These results indicate a stepwise peptide removal per diavolume, this fractional removal reaches a steady value after 4 DV. The average filtration efficiency which is a measure of the unbound peptide removal is 60.9 %.

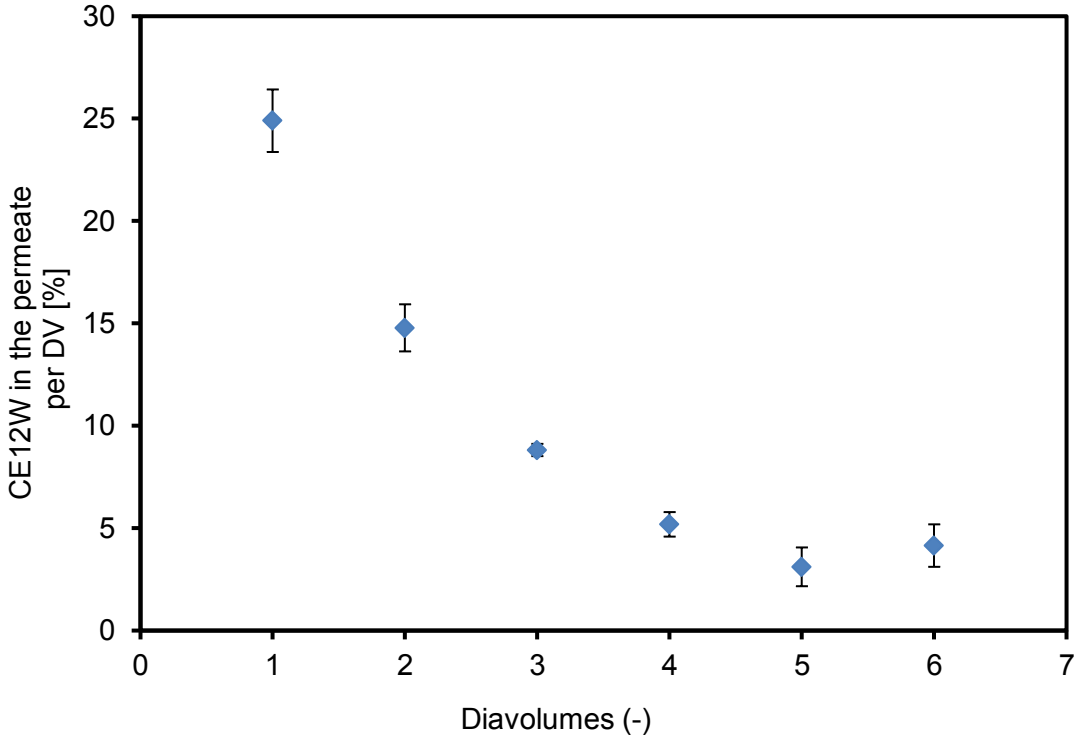

Figure 50: Profile for unbound peptide removal per diavolume using membrane RC 30 kDa (0.35 bar, ~ 50 L/m^{2}h).

In order to finally judge about the quality of the separation, the conjugation efficiency which is not directly accessible must be estimated. Considering the initial concentration of 20 µM $CE_{12}W$ and a particle size of 5 nm at the used AuNP concentration and solution volume, 10.4 % of the added ligands (7.8 µM) were found to be bound on the nanoparticles to form a monolayer. This concentration corresponds to a surface coverage of 297±51 ligands per nanoparticle (629 pmol/cm²), leading to a footprint of 0.26 nm² for the negative $CE_{12}W$ peptide on monomodal 5 nm gold nanoparticles. This surface coverage differs strongly from the value found in literature for this peptide which is, e.g., 100 pmol/cm² and was only estimated from zeta potential data [192]. Hence, one can conclude that, while adding the

peptide in excess to the nanoparticles, a densely packed peptide monolayer can be build up on the nanoparticles. Since this peptide is not that strongly charged as oligonucleotides are, a footprint below 1.1 nm² [193] seems to be realistic. Finally, the surface coverage formed by this peptide is comparable with small ligands like dodecanthiole (0.2 nm²) or citrate (0.3 nm²) [194]. The recovery of purified gold nanoparticle bioconjugate in the retentate was 87.4 % (in average 17.5 µg/mL, with a feed of 20 µg/mL) of their initial concentration.

The limiting factor is the barrier pore size of the membrane RC 30 kDa which is similar to the peptide molecular size. Potentially higher UF efficiencies could be reached with the RC 100 kDa membrane. However high transmission of valuable bioconjugated gold NP product, observed to be 10.1 ± 1.6 % (20.3 ± 2.6 µg) of the bioconjugate per diafiltration volume, has to be considered. On the other hand, a higher number of diavolumes 6 DV is needed for the complete removal of the unbound free peptide using RC 30 kDa membrane.

5.15 Comparison of ultrafiltration to centrifugal membrane filtration*

Here, the well-established separation method of ultrafiltration in diafiltration mode which is easily scalable to very large volumetric throughput, is compared to another filtration method that is already often used in nanoparticle purification processes in small (laboratory) scale, which is the centrifugal membrane filtration. In this method, the driving force is not applied pressure as in UF but the centrifugal force whose value depends only on the rotor speed and geometry of the used centrifuge. However, centrifugation in general stresses colloidal particles by shear forces and causes temperature increase, with only the latter being compensated in expensive centrifuges. The shear forces and forced sedimentation is well known to support nanoparticle aggregation [195], bearing the risk of compromising colloidal

* Experiments on centrifugal membrane purification had been performed by L. Gamrad and co-workers (AK Barcikowski).

quality and redispersability or yield. Nevertheless, this method is very easy in handling and can be routinely applied.

The used membranes were also made of regenerated cellulose and had a nominal molecular cut-off of 30 kDa (but from another manufacturer). This makes it possible to very well compare the centrifugation experiments to the ones shown before with pressure-driven ultrafiltration (cf. Section 5:13).

The gold nanoparticle-$CE_{12}W$ conjugate was filtrated six times and for every step the amount of peptide removed per diavolume was determined. The results show the same tendency as it was found in the ultrafiltration experiments: The amount of peptide decreased exponentially with an increasing number of diavolumes reaching a minimum of 3.4 % which is similar to what was reached using ultrafiltration (cf. Figure 51). Moreover, the first filtration step showed the separation of 16.6 % of the peptide molecules for the centrifugal filtration which is 8.3 % less than it was found for the ultrafiltration. This already indicated the higher effectivity of the ultrafiltration and is confirmed by the overall separation of only 44.6 % (centrifugal filtration) instead of 60.9 % (ultrafiltration). Considering the slightly different parameters of the initial particle and peptide concentration (40 µM $CE_{12}W$, 50 µg/mL AuNPs) the separation by centrifugal filtration leads to the conclusion that 337 peptide ligands were bound to one nanoparticle, this is in the same order of magnitude as the surface coverage found by ultrafiltration. A footprint of 0.23 nm^2 had been calculated which is also similar to the result from the diafiltration measurement. Additionally, referring to the results made by ultrafiltration, it has to be considered that more unbound ligands can still be present in the colloid after centrifugal filtration which could not be efficiently separated due to e.g. a smaller membrane surface.

Additionally to the filtration efficiency, the properties of the conjugates were controlled in order to ensure that the conjugates were not destabilized during the process. According to this, the mass loss of gold was found to be 7.3 %.

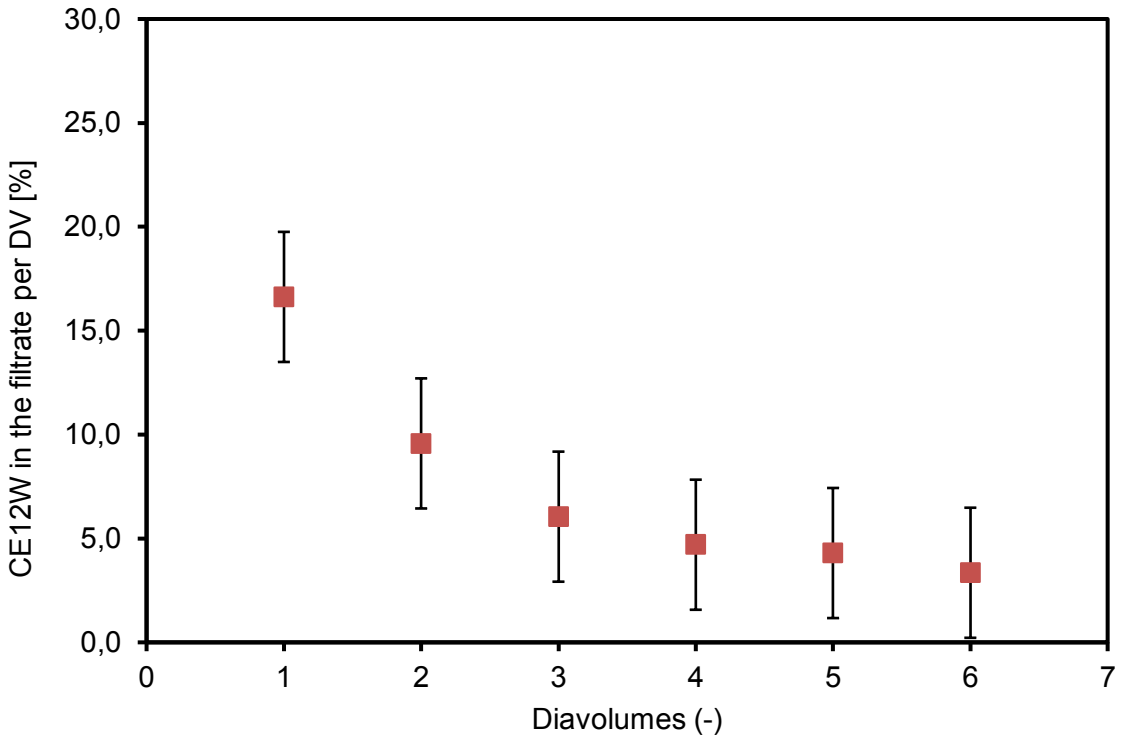

Figure 51: Fraction of unbound peptides found in the filtrate per diavolume using centrifugal membrane filtration tubes at 2701 g for 40 min in each step.

Finally, for the better comparison of the ultrafiltration process to the centrifugal filtration, the parameters of these processes were summarized in Table 10. The material and the pore size of the membranes used for the two filtration methods were the same which makes them comparable. Having a look to the two parameters that are most important for the classification of the methods, the loss of gold nanoparticles and the separation efficiency, it is not possible to easily identify one of the process as the most suitable one for nanoparticle purification. In the case of ultrafiltration, the loss of gold is relatively high with up to 17.7 % compared to centrifugal filtration (7.3 %) while the separation efficiency is 16.3 % higher

than it is for centrifugal filtration. Hence, if a 10 % higher nanoparticle mass loss is acceptable and product´s quality is in the primary aim of the purification step, the 16 % higher separation efficiency would render ultrafiltration most suitable. In addition, larger colloid volumes would be quite difficult to handle with centrifugal filtration, whereas UF processes are shown to be easily scalable [11]. Taking the results from the both lab-scaled methods described in this work for assuming scale-up values, purification of 1 liter (throughput) of nanogold bioconjugate would take 2 days in UF, and nearly 14 days in centrifugal filtration using only the filtration and centrifugation time for calculation. In contrast, the centrifugal filtration is the best choice for small volumes and less effective purification.

Table 10: Comparison of ultrafiltration and centrifugal filtration.

	Ultrafiltration	Centrifugal filtration
Membrane material	RC	RC
NMWCO	30 kDa	30 kDa
Membrane area	4.16 cm^2	2 x 3.8 cm^2
Number of Diavolumes	6	6
Sample Volume	10 mL	1.5 mL
Loss of Gold	11.7 % - 17.7 %	7.3 %
Separation effectivity	60.9 %	44.6 %
Throughput time (purification of 1 liter nanogold bioconjugate)	2 days	14 days

6 Conclusion and outlook

In this study, it has been shown that it possible to employ the sieving properties of UF membranes to remove proteins from metal oxide nanoparticle dispersions by proper choice of membrane properties (MWCO, hydrophilicity, surface charge) and UF conditions (operation below critical flux). Process conditions were found where rejection of silica nanoparticles (diameter 26 nm) was quantitative while the proteins could pass the membrane. In this work, BCA assay/AAS has been established to determine BSA/SiO2-NP concentration in both mixtures. In the studied model system the membrane RC 100 kDa was found to be suited for fractionation/purification of the dispersion. With an unmodified PES membrane with NMWCO 100 kDa, the separation was not feasible because of too high protein rejection due to strong fouling. The RC membrane showed excellent performance, while the amphoteric polymer hydrogel-functionalized PES membrane exhibited largely improved capability for the separation of proteins from silica dispersion compared to unmodified PES membrane. Membrane modification via UV-initiated “grafting-from” achieved the desired target objectives: IEP of 7, amphoteric property and with good reproducibility. Using continuous diafiltration, RC 100 membrane demonstrated best purification efficiency, i.e., larger removed protein mass at the same number of diavolumes in shorter filtration time compared with the hydrogel-functionalized PES membrane. Although RC and hydrogel-modified PES membranes showed similar hydrophilicity and antifouling properties when analyzed during static protein adsorption tests, they have different interfacial structures. While the RC surface is a swollen cellulose network, the

grafted hydrogel layer on the PES surface consists of flexible linear chains, and this may be the reason for the deterioration of antifouling properties during ultrafiltration. Hence stability improvement of the grafted amphoteric polymer hydrogel layer on the PES surface through cross-linking during the graft functionalization will be subject for further studies.

For the application to purification of functional NP-bioconjugates, the membrane RC 30 kDa was suitable. The fractionation and purification process were carried out using batch semi-continuous diafiltration mode. The RC 100 kDa membrane enabled high removal of unbound free peptides per three diafiltration volumes but experienced loss of gold nanoparticle conjugates up to 30 % through transmission across the membrane and possible adsorption. In contrary, RC 30 kDa membrane enabled total rejection of the bioconjugated gold nanoparticles. With RC 30 kDa membrane, the total recovery and removal of unbound free peptide molecules was 96.3 % and the yield of purified gold nanoparticle bioconjugate was 87.4 %. This result also proof that both valuable educts, the conjugate and the ligand, could be recovered. This effect is of high interest for recovery of very costly ligands used during nanoparticle functionalization, such as the aptamer ligand class gaining high application potential in biomedicine and drug targeting [196, 197]. The comparison to a commonly used bench top filtration method for nanoparticle purification showed that although centrifugal filtration has a 10 % higher nanoparticle yield, the method of ultrafiltration is about 16 % more efficient in the separation of unbound ligands from conjugated ones to nanoparticles. The scalability is also more realistic with UF membrane process than with centrifugal filtration. More so, the UF process has higher throughput.

This work further strengthens the fact that appropriate membrane type and size coupled with optimized filtration parameters and solution chemistry, UF membranes and in particular regenerated cellulose will be dependable in the purification of bioconjugated

nanoparticle dispersions. Moreover the Loss of bioconjugated gold NP by fouling can be further reduced through a more controlled diafiltration process.

Overall, this work has significantly expanded the knowledge about the use of membrane based separation methods for nanoparticle fractionation as well as removal of residual reactants. The latter could also be used for reducing agents, typically added in large excess during wet chemical metal and metal oxide (TiO_2 or ZnO) nanoparticle synthesis, and the efficient removal by diafiltration would greatly minimize reducing-agent-mediated aggregation [198] and post-synthesis ripening problems during handling and storage. Thus, both biomedical application of nanoparticles and their downstream processing after synthesis would benefit from colloid purification by membrane-based separation technologies.

7 References

[1] R.W. Baker, Ultrafiltration, in: Membrane Technology and Applications, John Wiley & Sons, Ltd, 2004, pp. 237-274.

[2] R. van Reis, A. Zydney, Bioprocess membrane technology, Journal of Membrane Science, 297 (2007) 16-50.

[3] M. Cheryan, Ultrafiltration and Microfiltration Handbook, Technomic Publishing Company Inc., Pennsylvania, 1998.

[4] L. J. Zeman, A.L. Zydney, Microfiltration and Ultrafiltration: Principles and Applications., Marcel Dekker Inc., New York, 1996.

[5] Y. Wan, Z. Cui, R. Ghosh, Fractionation of Proteins Using Ultrafiltration: Developments and Challenges, Developments in Chemical Engineering and Mineral Processing, 13 (2005) 121-136.

[6] Y. Zhang, R. Huang, X. Zhu, L. Wang, C. Wu, Synthesis, properties, and optical applications of noble metal nanoparticle-biomolecule conjugates, Chin. Sci. Bull., 57 (2012) 238-246.

[7] I. Limayem, C. Charcosset, H. Fessi, Purification of nanoparticle suspensions by a concentration/diafiltration process, Separation and Purification Technology, 38 (2004) 1-9.

[8] P. Beck, D. Scherer, J. Kreuter, Separation of drug-loaded nanoparticles from free drug by gel filtration, Journal of Microencapsulation, 7 (1990) 491-496.

[9] K.E. Sapsford, K.M. Tyner, B.J. Dair, J.R. Deschamps, I.L. Medintz, Analyzing Nanomaterial Bioconjugates: A Review of Current and Emerging Purification and Characterization Techniques, Analytical Chemistry, 83 (2011) 4453-4488.

[10] R. Ghosh, Protein separation using membrane chromatography: opportunities and challenges, Journal of chromatography. A, 952 (2002) 13-27.

[11] J.G. Crespo, I.M. Coelhoso, R.M.C. Viegas, Encyclopedia of Separation Processes, Academic Press, San Diego, 2000, pp. 3303 - 3311.

[12] G. Amy, J. Cho, Interactions Between Natural Organic Matter (NOM) and Membranes: Rejection and Fouling, Water Science and Technology, 40 (1999) 131-139.

[13] M. Zhou, H. Liu, J.E. Kilduff, R. Langer, D.G. Anderson, G. Belfort, High-Throughput Membrane Surface Modification to Control NOM Fouling, Environmental Science & Technology, 43 (2009) 3865-3871.

[14] H.-C. Kim, B.A. Dempsey, Effects of wastewater effluent organic materials on fouling in ultrafiltration, Water Research, 42 (2008) 3379-3384.

[15] M. Kabsch-Korbutowicz, Ultrafiltration as a method of separation of natural organic matter from water, Materials Science Poland, Vol. 26, No. 2 (2008) 459-467.

[16] H. Susanto, M. Ulbricht, Photografted Thin Polymer Hydrogel Layers on PES Ultrafiltration Membranes: Characterization, Stability, and Influence on Separation Performance, Langmuir, 23 (2007) 7818-7830.

[17] H. Strathmann, Membrane separation processes, Journal of Membrane Science, 9 (1981) 121-189.

[18] S.P. Nunes, K.V. Peinemann, eds., Membrane Technology in the Chemical Industry, Wiley-VCH, Weinheim, Germany (2001).

[19] A.K. Pebby., S.H.S. Rizvi, A.M.S. Requena, eds., Handbook of Membrane Separations. Chemical, Pharmaceutical, Food, and Biotechnological Applications, CRC Press, Boca Raton, FL (2009).

[20] M. Mulder, Basic Principles of Membrane Technology, second edition, Kluver Academic Publishers, 1996.

[21] W.J. Koros, Y.H. Ma, T. Shimidzu, Terminology for membranes and membrane processes (IUPAC Recommendation 1996), Journal of Membrane Science, 120 (1996) 149-159.

[22] W.S.W. Ho, K.K. Sirkar, Membrane Handbook, Van Nostrand Reinhold, New York. 1992.

[23] K.V. Peinemann, S.P. Nunes, eds., Membranes for Water Treatment. Volume 4, Wiley-VCH Verlag, Weinheim, Germany, 2010.

[24] H.P.G. Darcy, Les Fontaines Publiques de la Ville de Duon, Victor Dalmont, Paris, 1856.

[25] H. Strathmann, Introduction to Membrane Science and Technology, Wiley-VCH Verlag Co. KGaA, Weinheim, Germany, 2011.

[26] K.S. Spiegler, O. Kedem, Thermodynamics of hyperfiltration (reverse osmosis): criteria for efficient membranes, Desalination, 1 (1966) 311-326.

[27] O. Kedem, A. Katchalsky, Thermodynamic analysis of the permeability of biological membranes to non-electrolytes, Biochimica et Biophysica Acta, 27 (1958) 229-246.

[28] G. Jonsson, Boundary layer phenomena during ultrafiltration of dextran and whey protein solutions, Desalination, 51 (1984) 61-77.

[29] J.G. Wijmans, S. Nakao, J.W.A. Van Den Berg, F.R. Troelstra, C.A. Smolders, Hydrodynamic resistance of concentration polarization boundary layers in ultrafiltration, Journal of Membrane Science, 22 (1985) 117-135.

[30] J.G. Wijmans, S. Nakao, C.A. Smolders, Flux limitation in ultrafiltration: Osmotic pressure model and gel layer model, Journal of Membrane Science, 20 (1984) 115-124.

[31] A.D. W.F. Blatt, A.S. Michaels, L. Nelsen, Solute polarization and cake formation in membrane ultrafiltration: causes, consequences, and control techniques, in J. E. Flinn (ed.), Membrane Science and Technology, Plenum Press, New York, 1970, pp. 47-97.

[32] P. Dejmek, Concentration polarization in ultrafiltration of macromolecules, Ph.D. Thesis, Dept. Food Engineering, Lund Univ., 1975.

[33] E. Matthiasson, Macromolecular adsorption and fouling in ultrafiltration and their relationships to concentration polarization, Ph.D. Thesis, Dept. Food Engineering, Lund Univ., 1984.

[34] M. Al-Ahmad, F.A.A. Aleem, A. Mutiri, A. Ubaisy, Biofuoling in RO membrane systems Part 1: Fundamentals and control, Desalination, 132 (2000) 173-179.

[35] A.G. Fane, C.J.D. Fell, International Symposium on Synthetic Membrane Science and TechnologyA review of fouling and fouling control in ultrafiltration, Desalination, 62 (1987) 117-136.

[36] H. Susanto, Fouling Study in Ultrafiltrtaion: Mechanism and Control via Membrane Surface Modification, Dissertation, Universität Duisburg-Essen, Essen (2007).

[37] A.-S. Jönsson, G. Trägårdh, Fundamental principles of ultrafiltration, Chemical Engineering and Processing: Process Intensification, 27 (1990) 67-81.

[38] N. Hilal, O.O. Ogunbiyi, N.J. Miles, R. Nigmatullin, Methods Employed for Control of Fouling in MF and UF Membranes: A Comprehensive Review, Separation Science and Technology, 40 (2005) 1957-2005.

[39] I.H. Huisman, P. Prádanos, A. Hernández, The effect of protein–protein and protein–membrane interactions on membrane fouling in ultrafiltration, Journal of Membrane Science, 179 (2000) 79-90.

[40] S.T. Kelly, A.L. Zydney, Mechanisms for BSA fouling during microfiltration, Journal of Membrane Science, 107 (1995) 115-127.

[41] M.C.V. Vela, S.Á. Blanco, J.L. García, E.B. Rodríguez, Analysis of membrane pore blocking models applied to the ultrafiltration of PEG, Separation and Purification Technology, 62 (2008) 489-498.

[42] P. Bacchin, P. Aimar, R.W. Field, Critical and sustainable fluxes: Theory, experiments and applications, Journal of Membrane Science, 281 (2006) 42-69.

[43] P.D.Peeva, Dissertation, University Duisburg-Essen, Germany, 2011.

[44] S. De, J.M. Dias, P.K. Bhattacharya, Short and long term flux decline analysis in ultrafiltration, Chemical Engineering Communications, 159 (1997) 67-89.

[45] L. Song, Flux decline in crossflow microfiltration and ultrafiltration: mechanisms and modeling of membrane fouling, Journal of Membrane Science, 139 (1998) 183-200.

[46] J. Hermia, Constant pressure blocking filtration laws—application to power-law non-Newtonian fluids, Trans. Inst. Chem.Eng., 60, 183–187, V 60 (1982) 183-187.

[47] W.R. Bowen, J.I. Calvo, A. Hernández, Steps of membrane blocking in flux decline during protein microfiltration, Journal of Membrane Science, 101 (1995) 153-165.

[48] D. Wu, J.A. Howell, R.W. Field, Critical flux measurement for model colloids, Journal of Membrane Science, 152 (1999) 89-98.

[49] S. Metsämuuronen, J. Howell, M. Nyström, Critical flux in ultrafiltration of myoglobin and baker's yeast, Journal of Membrane Science, 196 (2002) 13-25.

[50] J.A. Howell, Sub-critical flux operation of microfiltration, Journal of Membrane Science, 107 (1995) 165-171.

[51] R.W. Field, D. Wu, J.A. Howell, B.B. Gupta, Critical flux concept for microfiltration fouling, Journal of Membrane Science, 100 (1995) 259-272.

[52] H. Susanto, S. Franzka, M. Ulbricht, Dextran fouling of polyethersulfone ultrafiltration membranes—Causes, extent and consequences, Journal of Membrane Science, 296 (2007) 147-155.

[53] N.A. Ochoa, M. Masuelli, J. Marchese, Effect of hydrophilicity on fouling of an emulsified oil wastewater with PVDF/PMMA membranes, Journal of Membrane Science, 226 (2003) 203-211.

[54] D. Möckel, E. Staude, M.D. Guiver, Static protein adsorption, ultrafiltration behavior and cleanability of hydrophilized polysulfone membranes, Journal of Membrane Science, 158 (1999) 63-75.

[55] C.-C. Ho, A.L. Zydney, Effect of membrane morphology on the initial rate of protein fouling during microfiltration, Journal of Membrane Science, 155 (1999) 261-275.

[56] K.L. Jones, C.R. O'Melia, Protein and humic acid adsorption onto hydrophilic membrane surfaces: effects of pH and ionic strength, Journal of Membrane Science, 165 (2000) 31-46.

[57] S. Salgın, Effects of Ionic Environments on Bovine Serum Albumin Fouling in a Cross-Flow Ultrafiltration System, Chemical Engineering & Technology, 30 (2007) 255-260.

[58] L. Palacio, J.I. Calvo, P. Prádanos, A. Hernández, P. Väisänen, M. Nyström, Contact angles and external protein adsorption onto UF membranes, Journal of Membrane Science, 152 (1999) 189-201.

[59] P. Ramesh Babu, V.G. Gaikar, Membrane characteristics as determinant in fouling of UF membranes, Separation and Purification Technology, 24 (2001) 23-34.

[60] K.-J. Kim, V. Chen, A.G. Fane, Ultrafiltration of Colloidal Silver Particles: Flux, Rejection, and Fouling, Journal of Colloid and Interface Science, 155 (1993) 347-359.

[61] M.R. Mackley, N.E. Sherman, Cross-flow cake filtration mechanisms and kinetics, Chemical Engineering Science, 47 (1992) 3067-3084.

[62] W. Yuan, A.L. Zydney, Humic acid fouling during microfiltration, Journal of Membrane Science, 157 (1999) 1-12.

[63] H. Chen, A.S. Kim, Prediction of permeate flux decline in crossflow membrane filtration of colloidal suspension: a radial basis function neural network approach, Desalination, 192 (2006) 415-428.

[64] M. Ulbricht, Advanced functional polymer membranes, Polymer, 47 (2006) 2217-2262.

[65] R. van Reis, A. Zydney, Membrane separations in biotechnology, Current Opinion in Biotechnology, 12 (2001) 208-211.

[66] E. Ostuni, R.G. Chapman, R.E. Holmlin, S. Takayama, G.M. Whitesides, A Survey of Structure−Property Relationships of Surfaces that Resist the Adsorption of Protein, Langmuir, 17 (2001) 5605-5620.

[67] M. Ulbricht, M. Riedel, U. Marx, Novel photochemical surface functionalization of polysulfone ultrafiltration membranes for covalent immobilization of biomolecules, Journal of Membrane Science, 120 (1996) 239-259.

[68] M. Ulbricht, H. Matuschewski, A. Oechel, H.-G. Hicke, Photo-induced graft polymerization surface modifications for the preparation of hydrophilic and low-proten-adsorbing ultrafiltration membranes, Journal of Membrane Science, 115 (1996) 31-47.

[69] C. Geismann, M. Ulbricht, Photoreactive Functionalization of Poly(ethylene terephthalate) Track-Etched Pore Surfaces with “Smart” Polymer Systems, Macromolecular Chemistry and Physics, 206 (2005) 268-281.

[70] M. Ulbricht, A. Oechel, C. Lehmann, G. Tomaschewski, H.-G. Hicke, Gas-phase photoinduced graft polymerization of acrylic acid onto polyacrylonitrile ultrafiltration membranes, Journal of Applied Polymer Science, 55 (1995) 1707-1723.

[71] M. Ulbricht, Photograft-polymer-modified microporous membranes with environment-sensitive permeabilities, Reactive and Functional Polymers, 31 (1996) 165-177.

[72] M. Ulbricht, M. Riedel, Ultrafiltration membrane surfaces with grafted polymer 'tentacles': preparation, characterization and application for covalent protein binding, Biomaterials, 19 (1998) 1229-1237.

[73] M. Ulbricht, H. Yang, Porous Polypropylene Membranes with Different Carboxyl Polymer Brush Layers for Reversible Protein Binding via Surface-Initiated Graft Copolymerization, Chemistry of Materials, 17 (2005) 2622-2631.

[74] M. Ulbricht, K. Richau, H. Kamusewitz, Chemically and morphologically defined ultrafiltration membrane surfaces prepared by heterogeneous photo-initiated graft polymerization, Colloids and Surfaces A: Physicochemical and Engineering Aspects, 138 (1998) 353-366.

[75] D. He, H. Susanto, M. Ulbricht, Photo-irradiation for preparation, modification and stimulation of polymeric membranes, Progress in Polymer Science, 34 (2009) 62-98.

[76] C.-M. Chan, Polymer surface modification and characterization, Carl Hanser Verlag, München, 1994.

[77] K. Ohlrogge, K. Ebert, (editors), Membranen. Grundlagen, Verfahren und industrielle Anwendungen, WILEY-VCH Verlag GmbH Co. KGaA, Weinheim, Germany, 2006.

[78] H. Yamagishi, J.V. Crivello, G. Belfort, Development of a novel photochemical technique for modifying poly (arylsulfone) ultrafiltration membranes, Journal of Membrane Science, 105 (1995) 237-247.

[79] S.-i. Kuroda, I. Mita, K. Obata, S. Tanaka, Degradation of aromatic polymers: Part IV—Effect of temperature and light intensity on the photodegradation of polyethersulfone, Polymer Degradation and Stability, 27 (1990) 257-270.

[80] C. Geismann, F. Tomicki, M. Ulbricht, Block Copolymer Photo-Grafted Poly(Ethylene Terephthalate) Capillary Pore Membranes Distinctly Switchable by Two Different Stimuli, Separation Science and Technology, 44 (2009) 3312-3329.

[81] A. Friebe, M. Ulbricht, Controlled Pore Functionalization of Poly(ethylene terephthalate) Track-Etched Membranes via Surface-Initiated Atom Transfer Radical Polymerization, Langmuir, 23 (2007) 10316-10322.

[82] A. Friebe, M. Ulbricht, Cylindrical Pores Responding to Two Different Stimuli via Surface-Initiated Atom Transfer Radical Polymerization for Synthesis of Grafted Diblock Copolymers, Macromolecules, 42 (2009) 1838-1848.

[83] M. Zhou, H. Liu, J.E. Kilduff, R. Langer, D.G. Anderson, G. Belfort, High-throughput membrane surface modification to control NOM fouling, Environ Sci Technol, 43 (2009) 3865-3871.

[84] X. Wang, D. Fang, K. Yoon, B.S. Hsiao, B. Chu, High performance ultrafiltration composite membranes based on poly(vinyl alcohol) hydrogel coating on crosslinked nanofibrous poly(vinyl alcohol) scaffold, Journal of Membrane Science, 278 (2006) 261-268.

[85] E. Uchida, Y. Uyama, Y. Ikada, Grafting of Water-Soluble Chains onto a Polymer Surface, Langmuir, 10 (1994) 481-485.

[86] A. Asatekin, A. Menniti, S. Kang, M. Elimelech, E. Morgenroth, A.M. Mayes, Antifouling nanofiltration membranes for membrane bioreactors from self-assembling graft copolymers, Journal of Membrane Science, 285 (2006) 81-89.

[87] R.S. Kane, P. Deschatelets, G.M. Whitesides, Kosmotropes Form the Basis of Protein-Resistant Surfaces, Langmuir, 19 (2003) 2388-2391.

[88] R. Bernstein, E. Antón, M. Ulbricht, Tuning the nanofiltration performance of thin film strong polyelectrolyte hydrogel composite membranes by photo-grafting conditions, Journal of Membrane Science, 427 (2013) 129-138.

[89] P.D. Peeva, T. Knoche, T. Pieper, M. Ulbricht, Performance of Thin-Layer Hydrogel Polyethersulfone Composite Membranes during Dead-End Ultrafiltration of Various Protein Solutions, Industrial & Engineering Chemistry Research, 51 (2012) 7231-7241.

[90] R.H. Li, T.A. Barbari, Performance of poly(vinyl alcohol) thin-gel composite ultrafiltration membranes, Journal of Membrane Science, 105 (1995) 71-78.

[91] P.D. Peeva, T. Pieper, M. Ulbricht, Tuning the ultrafiltration properties of anti-fouling thin-layer hydrogel polyethersulfone composite membranes by suited crosslinker monomers and photo-grafting conditions, Journal of Membrane Science, 362 (2010) 560-568.

[92] I. Eshet, V. Freger, R. Kasher, M. Herzberg, J. Lei, M. Ulbricht, Chemical and Physical Factors in Design of Antibiofouling Polymer Coatings, Biomacromolecules, 12 (2011) 2681-2685.

[93] H. Susanto, M. Balakrishnan, M. Ulbricht, Via surface functionalization by photograft copolymerization to low-fouling polyethersulfone-based ultrafiltration membranes, Journal of Membrane Science, 288 (2007) 157-167.

[94] T. Jimbo, A. Tanioka, N. Minoura, Characterization of an Amphoteric-Charged Layer Grafted to the Pore Surface of a Porous Membrane, Langmuir, 14 (1998) 7112-7118.

[95] C. Buzea, I.I. Pacheco, K. Robbie, Nanomaterials and nanoparticles: Sources and toxicity, Biointerphases, 2 (2007) MR17-MR71.

[96] D.B. Kittelson, 2001 Recent measurements of nanoparticle emission from engines Current Research on Diesel Exhaust Particles, Japan Association of Aerosol Science and Technology, 9 January (Tokyo, Japan).

[97] P.J.A. Borm, D. Robbins, S. Haubold, T. Kuhlbusch, H. Fissan, K. Donaldson, R. Schins, V. Stone, W. Kreyling, J. Lademann, J. Krutmann, D. Warheit, E. Oberdorster, The potential risks of nanomaterials: a review carried out for ECETOC, Part Fibre Toxicol, 3 (2006) 11-11.

[98] E. Roduner, Size matters: why nanomaterials are different, Chemical Society Reviews, 35 (2006) 583-592.

[99] S.K. Sahoo, V. Labhasetwar, Nanotech approaches to drug delivery and imaging, Drug Discovery Today, 8 (2003) 1112-1120.

[100] J. Perez, Bax, L. and Escolano, C., Roadmap Report on Nanoparticles, Willems & van den Wildenberg, Spain., (2005).

[101] T. Tsuzuki, Commercial scale production of inorganic nanoparticles, International Journal of Nanotechnology, 6 (2009) 567.

[102] K. J. Klabunde, NanoscaleMaterials in Chemistry,Wiley-Interscience,

New York, NY, USA, 2001.

[103] E. Reverchon, R. Adami, Nanomaterials and supercritical fluids, The Journal of Supercritical Fluids, 37 (2006) 1-22.

[104] G.A. Silva, Introduction to nanotechnology and its applications to medicine, Surgical Neurology, 61 (2004) 216-220.

[105] S. Barcikowski, F. Devesa, K. Moldenhauer, Impact and structure of literature on nanoparticle generation by laser ablation in liquids, Journal of Nanoparticle Research, 11 (2009) 1883-1893.

[106] A. Hahn, T. Stöver, G. Paasche, M. Löbler, K. Sternberg, H. Rohm, S. Barcikowski, Therapeutic Window for Bioactive Nanocomposites Fabricated by Laser Ablation in Polymer-Doped Organic Liquids, Advanced Engineering Materials, 12 (2010) B156-B162.

[107] B. Derjaguin, (1939) A theory of interaction of particles in presence of electric double-layers and the stability of lyophobe colloids and disperse systems, Acta Phys. Chim., 10, 333-346.

[108] B. Derjaguin, L.D. Landau, (1941) Theory of the stability of strongly charged lyophobic sols and of the adhesion of strongly charged particles in solutions of electrolytes Acta Phys. Chim., 14, 633-662.

[109] E.J.W. Verwey, J.T.G. Overbeek, (1948) Theory of Stability of Lyophobic Colloids Elsevier Amsterdam.

[110] J.N. Israelachvili, Intermolecular and Surface Forces , San Diego, CA: Academic., (2011).

[111] H.C. Hamaker, The London—van der Waals attraction between spherical particles, Physica, 4 (1937) 1058-1072.

[112] L. Bergstrom, A. Meurk, H. Arwin, D.J. Rowcliffe, Estimation of Hamaker Constants of Ceramic Materials from Optical Data Using Lifshitz Theory, Journal of the American Ceramic Society, 79 (1996) 339-348.

[113] A. Meurk, P.F. Luckham, L. Bergstrom, Direct measurement of repulsive and attractive van der Waals forces between inorganic materials, LANGMUIR, 13 (1997) 3896-3899.

[114] B. Faure, G. Salazar-Alvarez, A. Ahniyaz, I. Villaluenga, G. Berriozabal, Y.R.D. Miguel, L. Bergström, Dispersion and surface functionalization of oxide nanoparticles for transparent photocatalytic and, Science and Technology of Advanced Materials, 14 (2013) 023001.

[115] R.J. Pugh, Surface and Colloid Chemistry in Advanced Ceramics Processing ed R J Pugh and L Bergström (New York: Marcel Decker) p 127, 1994

[116] H. Ohshima, Effective Surface Potential and Double-Layer Interaction of Colloidal Particles, Journal of Colloid and Interface Science, 174 (1995) 45-52.

[117] D.H. Napper, Steric stabilization, Journal of Colloid and Interface Science, 58 (1977) 390-407.

[118] K.M.M. Abou El-Nour, A.a. Eftaiha, A. Al-Warthan, R.A.A. Ammar, Synthesis and applications of silver nanoparticles, Arabian Journal of Chemistry, 3 (2010) 135-140.

[119] R. Subbiah, M. Veerapandian, K.S. Yun, Nanoparticles: functionalization and multifunctional applications in biomedical sciences, Current medicinal chemistry, 17 (2010) 4559-4577.

[120] A.J. Haes, W.P. Hall, L. Chang, W.L. Klein, R.P. Van Duyne, A Localized Surface Plasmon Resonance Biosensor: First Steps toward an Assay for Alzheimer's Disease, Nano Letters, 4 (2004) 1029-1034.

[121] I. Hussain, S. Graham, Z. Wang, B. Tan, D.C. Sherrington, S.P. Rannard, A.I. Cooper, M. Brust, Size-Controlled Synthesis of Near-Monodisperse Gold Nanoparticles in the 1−4 nm Range Using Polymeric Stabilizers, Journal of the American Chemical Society, 127 (2005) 16398-16399.

[122] A. Taleb, C. Petit, M.P. Pileni, Synthesis of Highly Monodisperse Silver Nanoparticles from AOT Reverse Micelles: A Way to 2D and 3D Self-Organization, Chemistry of Materials, 9 (1997) 950-959.

[123] C.B. Murray, D.J. Norris, M.G. Bawendi, Synthesis and characterization of nearly monodisperse CdE (E = sulfur, selenium, tellurium) semiconductor nanocrystallites, Journal of the American Chemical Society, 115 (1993) 8706-8715.

[124] C.J. Murphy, T.K. Sau, A.M. Gole, C.J. Orendorff, J. Gao, L. Gou, S.E. Hunyadi, T. Li, Anisotropic Metal Nanoparticles: Synthesis, Assembly, and Optical Applications, The Journal of Physical Chemistry B, 109 (2005) 13857-13870.

[125] J.H. Adair, E. Suvaci, Morphological control of particles, Current Opinion in Colloid and Interface Science, 5 (2000) 160-167.

[126] S. Kumar, T. Nann, Shape Control of II–VI Semiconductor Nanomaterials, Small, 2 (2006) 316-329.

[127] C.T. Yavuz, J.T. Mayo, W.W. Yu, A. Prakash, J.C. Falkner, S. Yean, L. Cong, H.J. Shipley, A. Kan, M. Tomson, D. Natelson, V.L. Colvin, Low-Field Magnetic Separation of Monodisperse Fe3O4 Nanocrystals, Science, 314 (2006) 964-967.

[128] A.H. Latham, R.S. Freitas, P. Schiffer, M.E. Williams, Capillary Magnetic Field Flow Fractionation and Analysis of Magnetic Nanoparticles, Analytical Chemistry, 77 (2005) 5055-5062.

[129] V.L. Jimenez, M.C. Leopold, C. Mazzitelli, J.W. Jorgenson, R.W. Murray, HPLC of Monolayer-Protected Gold Nanoclusters, Analytical Chemistry, 75 (2003) 199-206.

[130] J.P. Wilcoxon, J.E. Martin, P. Provencio, Size Distributions of Gold Nanoclusters Studied by Liquid Chromatography, Langmuir, 16 (2000) 9912-9920.

[131] B. Kowalczyk, I. Lagzi, B.A. Grzybowski, Nanoseparations: Strategies for size and/or shape-selective purification of nanoparticles, Current Opinion in Colloid & Interface Science, 16 (2011) 135-148.

[132] T. Siebrands, M. Giersig, P. Mulvaney, C.H. Fischer, Steric exclusion chromatography of nanometer-sized gold particles, Langmuir, 9 (1993) 2297-2300.

[133] J.J. Kirkland, High-performance size-exclusion liquid chromatography of inorganic colloids, Journal of Chromatography A, 185 (1979) 273-288.

[134] C.H. Fischer, J. Lilie, H. Weller, L. Katsikas, A. Henglein, Photochemistry of colloidal semiconductors 29. Fractionation of CdS sols of small particles by exclusion chromatography, Berichte der Bunsengesellschaft für physikalische Chemie, 93 (1989) 61-64.

[135] J.P. Novak, C. Nickerson, S. Franzen, D.L. Feldheim, Purification of Molecularly Bridged Metal Nanoparticle Arrays by Centrifugation and Size Exclusion Chromatography, Analytical Chemistry, 73 (2001) 5758-5761.

[136] M.K. Brakke, Density Gradient Centrifugation And its Application to Plant Viruses. In: Advances in Virus Research, (1960, pp. 193-224).

[137] X. Sun, S.M. Tabakman, W.-S. Seo, L. Zhang, G. Zhang, S. Sherlock, L. Bai, H. Dai, Separation of Nanoparticles in a Density Gradient: FeCo@C and Gold Nanocrystals, Angewandte Chemie International Edition, 48 (2009) 939-942.

[138] V. Sharma, K. Park, M. Srinivasarao, Shape separation of gold nanorods using centrifugation, Proceedings of the National Academy of Sciences, 106 (2009) 4981-4985.

[139] R. Westermeier, Electrophoresis in practice, (Wiley-VCH (2005)).

[140] C.R. Vestal, Z.J. Zhang, Synthesis of CoCrFeO4 Nanoparticles Using Microemulsion Methods and Size-Dependent Studies of Their Magnetic Properties, Chemistry of Materials, 14 (2002) 3817-3822.

[141] M. Hanauer, S. Pierrat, I. Zins, A. Lotz, C. Sönnichsen, Separation of Nanoparticles by Gel Electrophoresis According to Size and Shape, Nano Letters, 7 (2007) 2881-2885.

[142] I. Arnaud, J.-P. Abid, C. Roussel, H.H. Girault, Size-selective separation of gold nanoparticles using isoelectric focusing electrophoresis (IEF), Chemical Communications, (2005) 787-788.

[143] J.-S. Lee, S.I. Stoeva, C.A. Mirkin, DNA-Induced Size-Selective Separation of Mixtures of Gold Nanoparticles, Journal of the American Chemical Society, 128 (2006) 8899-8903.

[144] W. Zhao, L. Lin, I.M. Hsing, Nucleotide-Mediated Size Fractionation of Gold Nanoparticles in Aqueous Solutions, Langmuir, 26 (2010) 7405-7409.

[145] T. Xu, M. Jin, Z. Xie, Z. Jiang, Q. Kuang, H. Wu, R. Huang, L. Zheng, Tensions at Liquid Interfaces: A General Filter for the Separation of Micro-/Nanoparticles, Langmuir, 24 (2008) 2281-2283.

[146] S.R. Saunders, C.B. Roberts, Size-selective fractionation of nanoparticles at an application scale using CO 2 gas-expanded liquids, Nanotechnology, 20 (2009) 475605.

[147] O.M. Wilson, R.W.J. Scott, J.C. Garcia-Martinez, R.M. Crooks, Separation of Dendrimer-Encapsulated Au and Ag Nanoparticles by Selective Extraction, Chemistry of Materials, 16 (2004) 4202-4204.

[148] J.-f. Liu, R. Liu, Y.-g. Yin, G.-b. Jiang, Triton X-114 based cloud point extraction: a thermoreversible approach for separation/concentration and dispersion of nanomaterials in the aqueous phase, Chemical Communications, (2009) 1514-1516.

[149] H.W. Liang, L. Wang, P.Y. Chen, H.T. Lin, L.F. Chen, D. He, S.H. Yu, Carbonaceous nanofiber membranes for selective filtration and separation of nanoparticles, Advanced Materials, 22 (2010) 4691-4695.

[150] M.M. Mekawy, A. Yamaguchi, S.A. El-Safty, T. Itoh, N. Teramae, Mesoporous silica hybrid membranes for precise size-exclusive separation of silver nanoparticles, Journal of Colloid and Interface Science, 355 (2011) 348-358.

[151] T.R. Gaborski, J.L. Snyder, C.C. Striemer, D.Z. Fang, M. Hoffman, P.M. Fauchet, J.L. McGrath, High-Performance Separation of Nanoparticles with Ultrathin Porous Nanocrystalline Silicon Membranes, ACS Nano, 4 (2010) 6973-6981.

[152] Q.-L. Xie, J. Liu, X.-X. Xu, G.-B. Han, H.-P. Xia, X.-M. He, Size separation of Fe2O3 nanoparticles via membrane processing, Separation and Purification Technology, 66 (2009) 148-152.

[153] A. Akthakul, A.I. Hochbaum, F. Stellacci, A.M. Mayes, Size Fractionation of Metal Nanoparticles by Membrane Filtration, Advanced Materials, 17 (2005) 532-535.

[154] E. Krieg, H. Weissman, E. Shirman, E. Shimoni, B. Rybtchinski, A recyclable supramolecular membrane for size-selective separation of nanoparticles, Nat Nano, 6 (2011) 141-146.

[155] S.F. Sweeney, G.H. Woehrle, J.E. Hutchison, Rapid Purification and Size Separation of Gold Nanoparticles via Diafiltration, Journal of the American Chemical Society, 128 (2006) 3190-3197.

[156] G. Dalwadi, H.A. Benson, Y. Chen, Comparison of diafiltration and tangential flow filtration for purification of nanoparticle suspensions, Pharmaceutical research, 22 (2005) 2152-2162.

[157] S. Frost, M. Ulbricht, Thermoresponsive ultrafiltration membranes for the switchable permeation and fractionation of nanoparticles, Journal of Membrane Science, 448 (2013) 1-11.

[158] G. Tishchenko, K. Luetzow, J. Schauer, W. Albrecht, M. Bleha, Purification of polymer nanoparticles by diafiltration with polysulfone/hydrophilic polymer blend membranes, Separation and Purification Technology, 22-23 (2001) 403-415.

[159] G. Tishchenko, R. Hilke, W. Albrecht, J. Schauer, K. Luetzow, Z. Pientka, M. Bleha, Ultrafiltration and microfiltration membranes in latex purification by diafiltration with suction, Separation and Purification Technology, 30 (2003) 57-68.

[160] Y.-H. Zhao, K.-H. Wee, R. Bai, A Novel Electrolyte-Responsive Membrane with Tunable Permeation Selectivity for Protein Purification, ACS Applied Materials & Interfaces, 2 (2010) 203-211.

[161] G. Dalwadi, B. Sunderland, Comparison and Validation of Drug Loading Parameters of PEGylated Nanoparticles Purified by a Diafiltration Centrifugal Device and Tangential Flow Filtration, Drug Development and Industrial Pharmacy, 34 (2008) 1331-1342.

[162] G. Dalwadi, V.B. Sunderland, Purification of PEGylated Nanoparticles Using Tangential Flow Filtration (TFF), Drug Development and Industrial Pharmacy, 33 (2007) 1030-1039.

[163] C. Rehbock, J. Jakobi, L. Gamrad, S. van der Meer, D. Tiedemann, U. Taylor, W. Kues, D. Rath, S. Barcikowski, Current state of laser synthesis of metal and alloy nanoparticles as ligand-free reference materials for nano-toxicological assays, Beilstein Journal of Nanotechnology, 5 (2014) 1523-1541.

[164] C.L.E. Hart H., Hart D.J., Organische Chemie, 2nd edition, WILEY-VCH Verlag GmbH, Weinheim, Germany, 2002.

[165] M. Taniguchi, J. Pieracci, W.A. Samsonoff, G. Belfort, UV-Assisted Graft Polymerization of Synthetic Membranes: Mechanistic Studies, Chemistry of Materials, 15 (2003) 3805-3812.

[166] C. Fänger, H. Wack, M. Ulbricht, Macroporous Poly(N-isopropylacrylamide) Hydrogels with Adjustable Size “Cut-off” for the Efficient and Reversible Immobilization of Biomacromolecules, Macromolecular Bioscience, 6 (2006) 393-402.

[167] D. Möckel, E. Staude, M. Dal-Cin, K. Darcovich, M. Guiver, Tangential flow streaming potential measurements: Hydrodynamic cell characterization and zeta potentials of carboxylated polysulfone membranes, Journal of Membrane Science, 145 (1998) 211-222.

[168] J. Benesch, A. Askendal, P. Tengvall, Quantification of adsorbed human serum albumin at solid interfaces: a comparison between radioimmunoassay (RIA) and simple null ellipsometry, Colloids and Surfaces B: Biointerfaces, 18 (2000) 71-81.

[169] I.H. Malitson, Interspecimen Comparison of the Refractive Index of Fused Silica, J. Opt. Soc. Am., 55 (1965) 1205-1208.

[170] Y. Yoon, R.M. Lueptow, Concentration of colloidal silica suspensions using fluorescence spectroscopy, Colloids and Surfaces A: Physicochemical and Engineering Aspects, 277 (2006) 107-110.

[171] A.L. Zydney, A. Xenopoulos, Improving dextran tests for ultrafiltration membranes: Effect of device format, Journal of Membrane Science, 291 (2007) 180-190.

[172] P.D. Peeva, N. Million, M. Ulbricht, Factors affecting the sieving behavior of anti-fouling thin-layer cross-linked hydrogel polyethersulfone composite ultrafiltration membranes, Journal of Membrane Science, 390–391 (2012) 99-112.

[173] S. Belfer, R. Fainchtain, Y. Purinson, O. Kedem, Surface characterization by FTIR-ATR spectroscopy of polyethersulfone membranes-unmodified, modified and protein fouled, Journal of Membrane Science, 172 (2000) 113-124.

[174] R. Bernstein, E. Antón, M. Ulbricht, UV-Photo Graft Functionalization of Polyethersulfone Membrane with Strong Polyelectrolyte Hydrogel and Its Application for Nanofiltration, ACS Applied Materials & Interfaces, 4 (2012) 3438-3446.

[175] M. Nyström, M. Lindström, E. Matthiasson, Streaming potential as a tool in the characterization of ultrafiltration membranes, Colloids and Surfaces, 36 (1989) 297-312.

[176] C. Lettmann, D. Möckel, E. Staude, Permeation and tangential flow streaming potential measurements for electrokinetic characterization of track-etched microfiltration membranes, Journal of Membrane Science, 159 (1999) 243-251.

[177] M. Elimelech, C.R. O'Melia, Effect of electrolyte type on the electrophoretic mobility of polystyrene latex colloids, Colloids and Surfaces, 44 (1990) 165-178.

[178] N. Soyer, U. Salgın, S. Salgın, Streaming Potential Measurements of Polyethersulfone Ultrafiltration Membranes to Determine Salt Effects on Membrane Zeta Potential, Int. J. Electrochem. Sci., 8 4073-4080.

[179] M. Kumar, M. Ulbricht, Advanced ultrafiltration membranes based on functionalized poly(arylene ether sulfone) block copolymers, RSC Advances, 3 (2013) 12190-12203.

[180] M. Kumar, M. Ulbricht, Novel ultrafiltration membranes with adjustable charge density based on sulfonated poly(arylene ether sulfone) block copolymers and their tunable protein separation performance, Polymer, 55 (2014) 354-365.

[181] Vollhardt K.P.C., Schore N.E., Organische Chemie, 4th edition, WILEY-VCH GmbH & Co. KGaA, Weinheim, Germany, 2005.

[182] M.N. Sarbolouki, A General Diagram for Estimating Pore Size of Ultrafiltration and Reverse Osmosis Membranes, Separation Science and Technology, 17 (1982) 381-386.

[183] P.D. Peeva, A.E. Palupi, M. Ulbricht, Ultrafiltration of humic acid solutions through unmodified and surface functionalized low-fouling polyethersulfone membranes – Effects of feed properties, molecular weight cut-off and membrane chemistry on fouling behavior and cleanability, Separation and Purification Technology, 81 (2011) 124-133.

[184] E. Iritani, Y. Mukai, T. Murase, Upward Dead-End Ultrafiltration of Binary Protein Mixtures, Separation Science and Technology, 30 (1995) 369-382.

[185] B. Lorber, F. Fischer, M. Bailly, H. Roy, D. Kern, Protein analysis by dynamic light scattering: Methods and techniques for students, Biochemistry and Molecular Biology Education, 40 (2012) 372-382.

[186] P.D. Peeva, T. Knoche, T. Pieper, M. Ulbricht, Cross-flow ultrafiltration of protein solutions through unmodified and surface functionalized polyethersulfone membranes – Effect of process conditions on separation performance, Separation and Purification Technology, 92 (2012) 83-92.

[187] R. Ghosh, Z.F. Cui, Purification of lysozyme using ultrafiltration, Biotechnology and Bioengineering, 68 (2000) 191-203.

[188] N.O. Becht, D.J. Malik, E.S. Tarleton, Evaluation and comparison of protein ultrafiltration test results: Dead-end stirred cell compared with a cross-flow system, Separation and Purification Technology, 62 (2008) 228-239.

[189] S.J. Hurst, A.K.R. Lytton-Jean, C.A. Mirkin, Maximizing DNA Loading on a Range of Gold Nanoparticle Sizes, Analytical Chemistry, 78 (2006) 8313-8318.

[190] M. Kumar, M. Ulbricht, Low fouling negatively charged hybrid ultrafiltration membranes for protein separation from sulfonated poly(arylene ether sulfone) block copolymer and functionalized multiwalled carbon nanotubes, Separation and Purification Technology, 127 (2014) 181-191.

[191] V. Chen, A.G. Fane, S. Madaeni, I.G. Wenten, Particle deposition during membrane filtration of colloids: transition between concentration polarization and cake formation, Journal of Membrane Science, 125 (1997) 109-122.

[192] L. Gamrad, C. Rehbock, J. Krawinkel, B. Tumursukh, A. Heisterkamp, S. Barcikowski, Charge Balancing of Model Gold-Nanoparticle-Peptide Conjugates Controlled by the Peptide's Net Charge and the Ligand to Nanoparticle Ratio, The Journal of Physical Chemistry C, 118 (2014) 10302-10313.

[193] S. Petersen, S. Barcikowski, Conjugation Efficiency of Laser-Based Bioconjugation of Gold Nanoparticles with Nucleic Acids, The Journal of Physical Chemistry C, 113 (2009) 19830-19835.

[194] P. Wagener, A. Schwenke, S. Barcikowski, How Citrate Ligands Affect Nanoparticle Adsorption to Microparticle Supports, Langmuir, 28 (2012) 6132-6140.

[195] S.K. Balasubramanian, L. Yang, L.Y. Yung, C.N. Ong, W.Y. Ong, L.E. Yu, Characterization, purification, and stability of gold nanoparticles, Biomaterials, 31 (2010) 9023-9030.

[196] J.G. Walter, S. Petersen, F. Stahl, T. Scheper, S. Barcikowski, Laser ablation-based one-step generation and bio-functionalization of gold nanoparticles conjugated with aptamers, Journal of nanobiotechnology, 8 (2010) 21.

[197] C. Reinemann, B. Strehlitz, Aptamer-modified nanoparticles and their use in cancer diagnostics and treatment, Swiss medical weekly, 144 (2014) w13908.

[198] J.-W. Park, J.S. Shumaker-Parry, Structural Study of Citrate Layers on Gold Nanoparticles: Role of Intermolecular Interactions in Stabilizing Nanoparticles, Journal of the American Chemical Society, 136 (2014) 1907-1921.

8 Appendix

8.1 Abbreviations

UF	Ultrafiltration
MF	Microfiltration
NF	Nanofiltration
RO	Reverse Osmosis
NMWCO	Nominal molecular weight cut-off
MWCO	Molecular weight cut-off
SiO_2-NP	Silica nanoparticles
AuNP	Gold nanoparticles
AMPS	2-acrylamido-2-methyl-1-propanesulfonic acid
DMAPAA	N-[3-(dimethylamino)propyl]-acrylamide
BSA	Bovine serum albumin
LYS	Lysozyme
PES	Polyethersulfone
RC	Regenerated cellulose
DV	Infiltration
TMP	Transmembrane pressure
ZP	Zeta potential
EDTA	Ethylenediaminetetraacetic acid
Nm	Nanometer
TiO2	Titanium oxide
ZnO	Zinc oxide
HSA	Human serum albumin
FNP	Functionalization of nanoparticles
SWCNT	Single-walled carbon nano-tube
MWCNT	Multi-walled carbon nano-tube

HNO_3	Nitric acid
CF	Cross-flow (filtration)
BCF	Below critical flux
ACF	Above critical flux
CP	Concentration polarization
DE	Dead-end (filtration)
DLS	Dynamic light scattering
DLVO	Derjagin-Landau-Verwey-Overbeek (model)
GPC	Gel permeation chromatography
IEP	Isoelectric point
HGMS	High gradient magnetic separation
MFFF	Magnetic field flow fractionation
HPLC	High performance liquid chromatography
SEC	Size exclusion chromatography
RZC	Rate zonal centrifugation
AuNRs	Gold nanorods
AuNPs	Gold nanoparticles
PAA	Polyacrylamide
IEF	Isoelectric focusing
FFF	Free flow electrophoresis
GE	Gel electrophoresis
KCl	Potassium chloride
KH_2PO4	Potassium dihydrogen phosphate
H_{gel}F-PES 300	hydrogel-functionalized PES 300 membrane
SSP	size –selective precipitation
DENs	Dendrimer encapsulated NPs
CPE	Cloud point extraction
CPT	Cloud point temperature
POEM	Poly(oxyethylene methacrylate)
DG	Degree of grafting
MUA	Mercaptoundecanoic acid
Na_2HPO4	Disodium hydrogen phosphate

NaCl	Nodium chloride
NaN_3	Sodium azide
NaOH	Caustic soda
NP	Nanoparticle
PAN	Polyacrylonitrile copolymers
PBS	Phosphate buffer solution
PDI	Polydispersity index
PS	Polysulfone
PVDF	Poly(vinylidene fluoride)
RIS	Resistance-in-series (model)
SEM	Scanning electron microscopy
SiO_2	Silica
TEM	Transmission electron microscopy
UV	Ultraviolet (light)

8.2 Lists

8.2.1 List of figures

8.2.2 List of tables

8.3 Calibrations for solute concentration determination and Comparison of Analyses

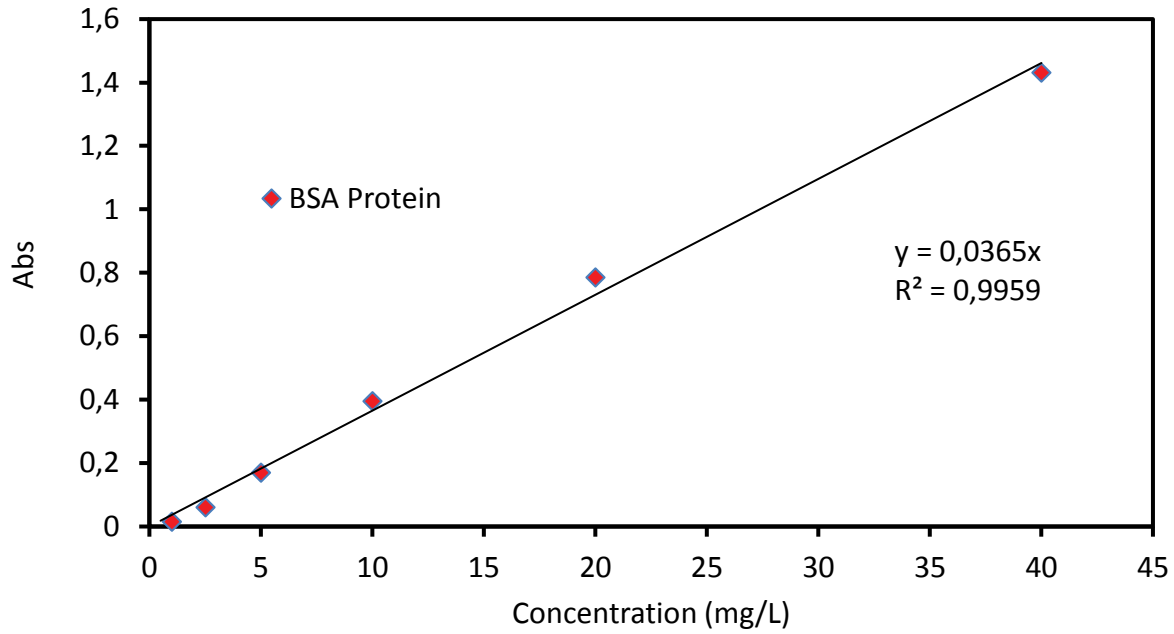

Figure A.1: Calibration to quantify the amount of single BSA using Micro BCA™ Protein Assay Kit.

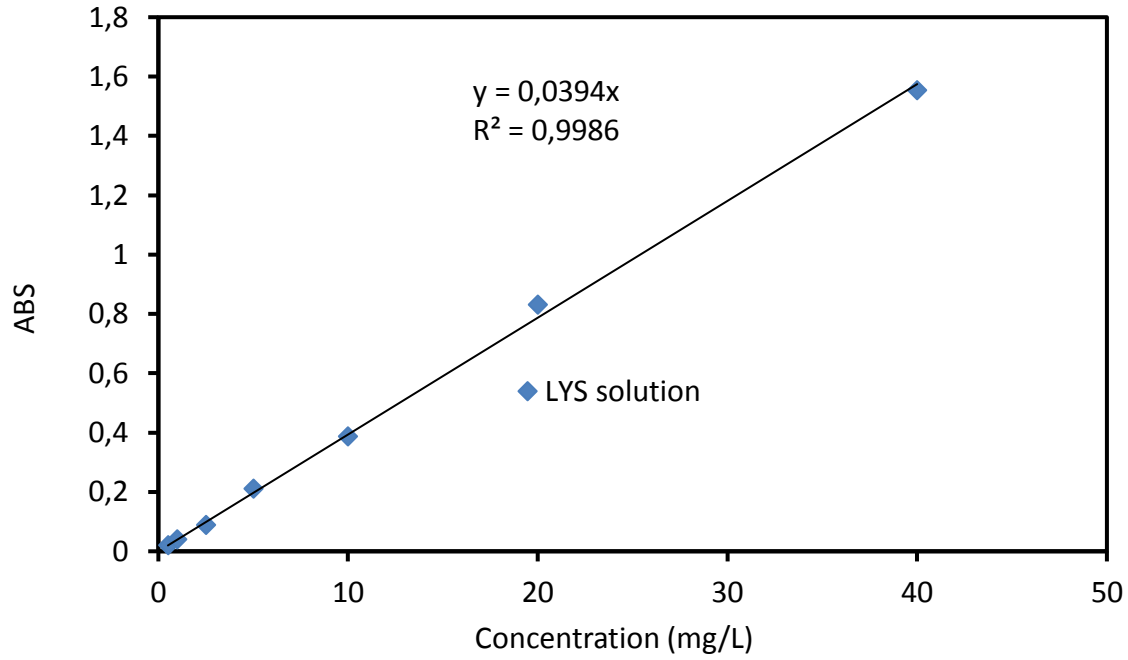

Figure A.2: Calibration to quantify the amount of single LYS solution using Micro BCA™ Protein Assay Kit.

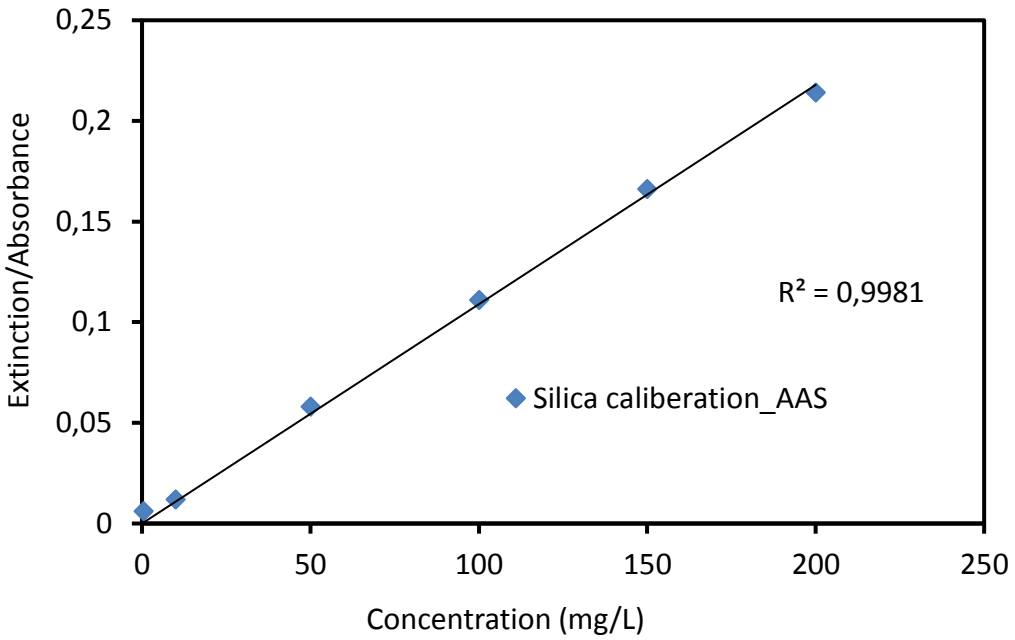

Figure A.3: Calibration to quantify the amount of single silica solutions using AAS

Figure A.4 show the calibration curves for silica-NP*s* conducted with the same standard solutions to be able to compare the different measurement methods to each other. Evaluation of the relative and absolute deviations of single measurement points from the calibration line lead to an estimation for the detection limit presented in Table A 1. Here the blank measurement points were use for the lower limit of detection (LLD). The lower limit of detection of an individual analytical procedure is the lowest amount of analyte in a sample which can be detected but not necessarily quantified as an exact value.

$$LLD = 3\,x\,S_{bl}$$

Where S_{bl} is the standard deviation of the blank.

Table A.1: Comparison of absolute/relative deviations and derived detection limits.

	Fluorescence	AAS
Absolute variation	5 a.u.	0.001 a.u.
Relative variation	1…5 %	1 %
Zero value	10 a.u.	~ 0.001 a.u.
Detection limit	5 a.u. / 5 mg/L	0.001 a.u. / 1 mg/L

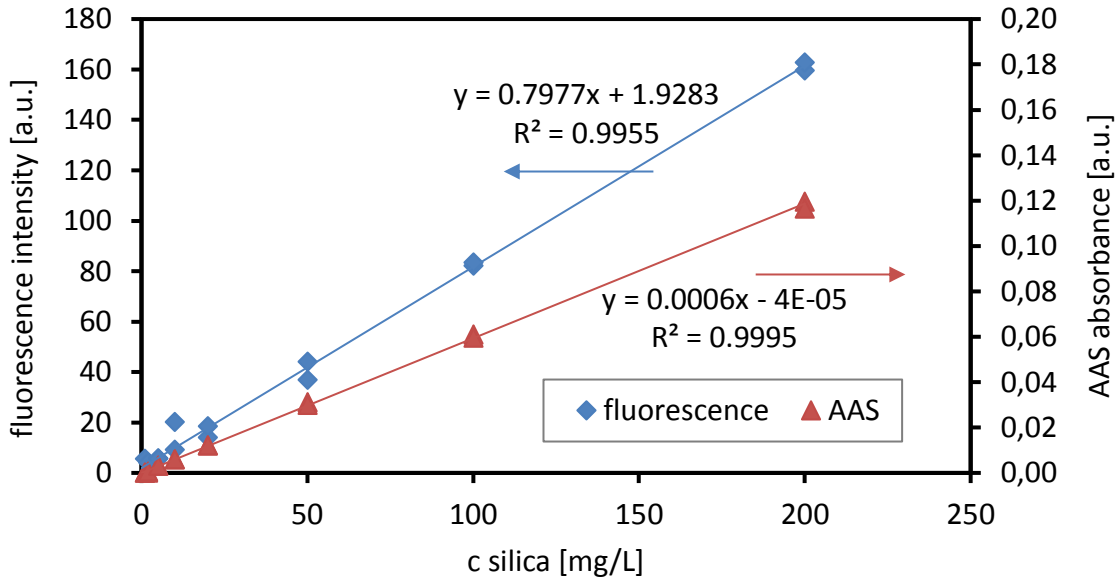

Figure A.4: Silica-NP calibrations of fluorescence spectroscopy and AAS

AAS is considered superior to fluorescence spectroscopy because it possesses a lower LLD and probably a similar linear range.

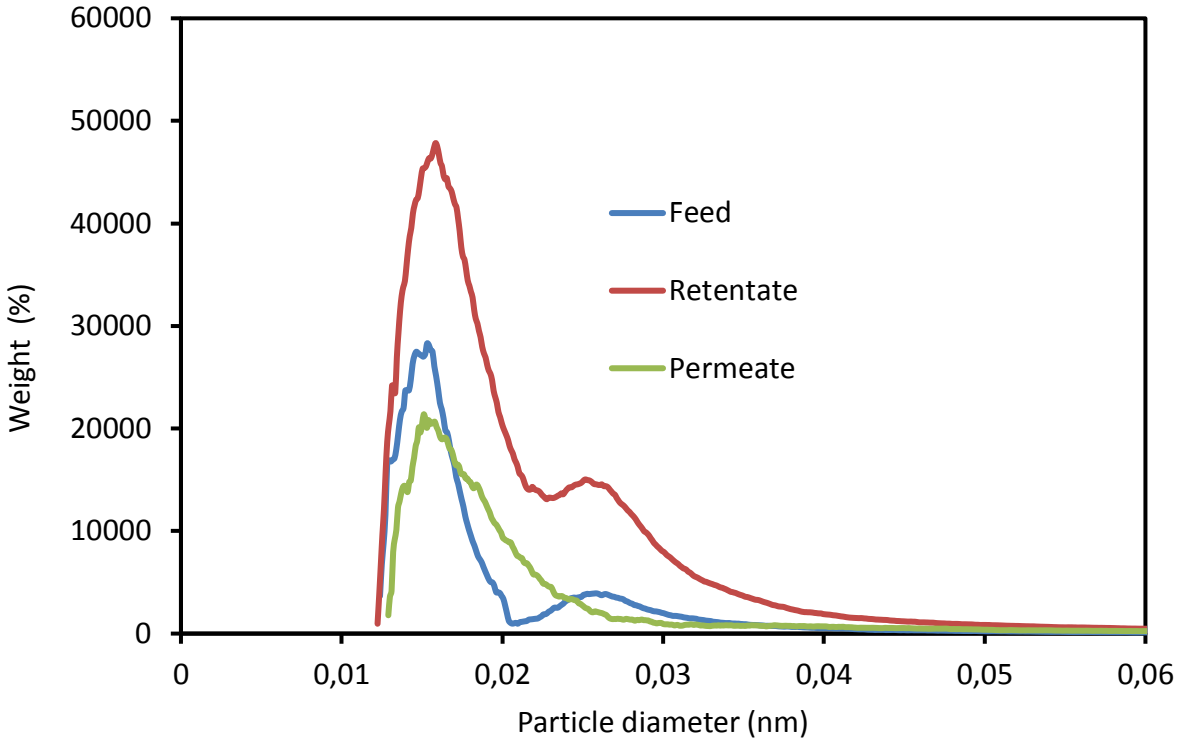

Figure A.5: Fractionation performance with PES 300 kDa membrane

Figure A.6:

8.4 Critical flux determination

Figure A.5-A.7 was used for critical flux determination using data from table A.2. The critical flux was determined through deviation from the initial slope. In table A.2, RC and PES 100 deviations from the initial slope was earlier noticed than the modified PES 300 membrane. Only up to this deviations as shown in table A.2.

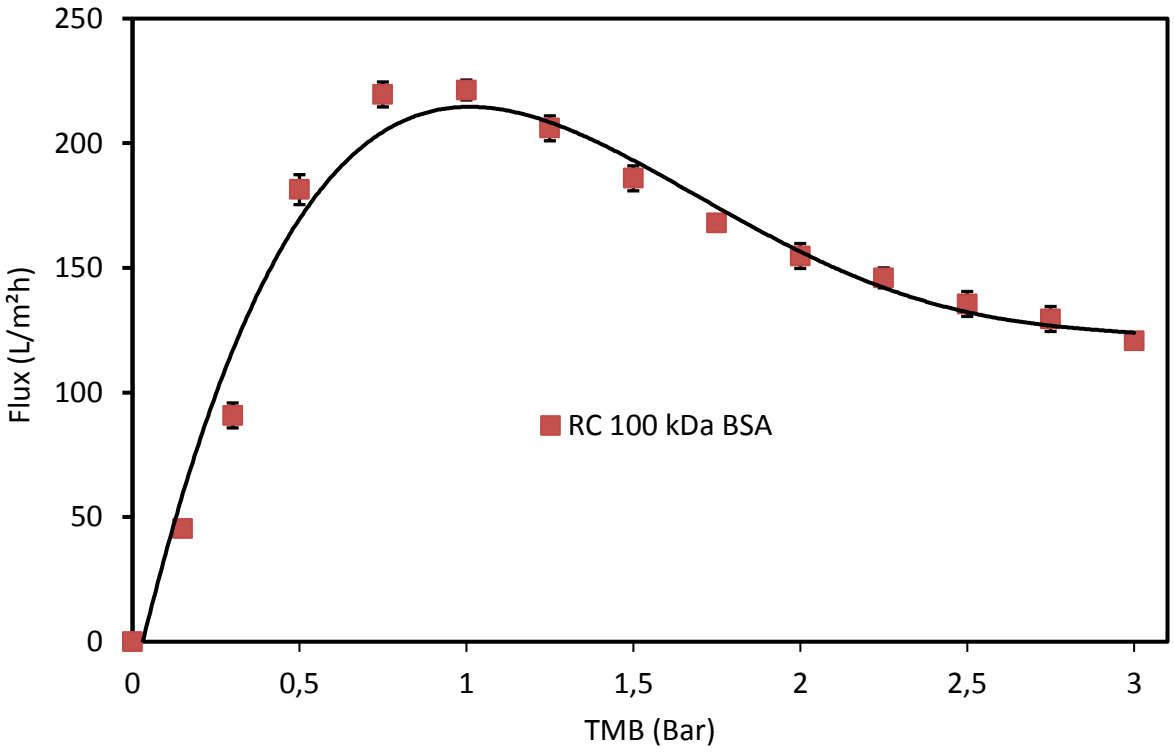

Figure A.7

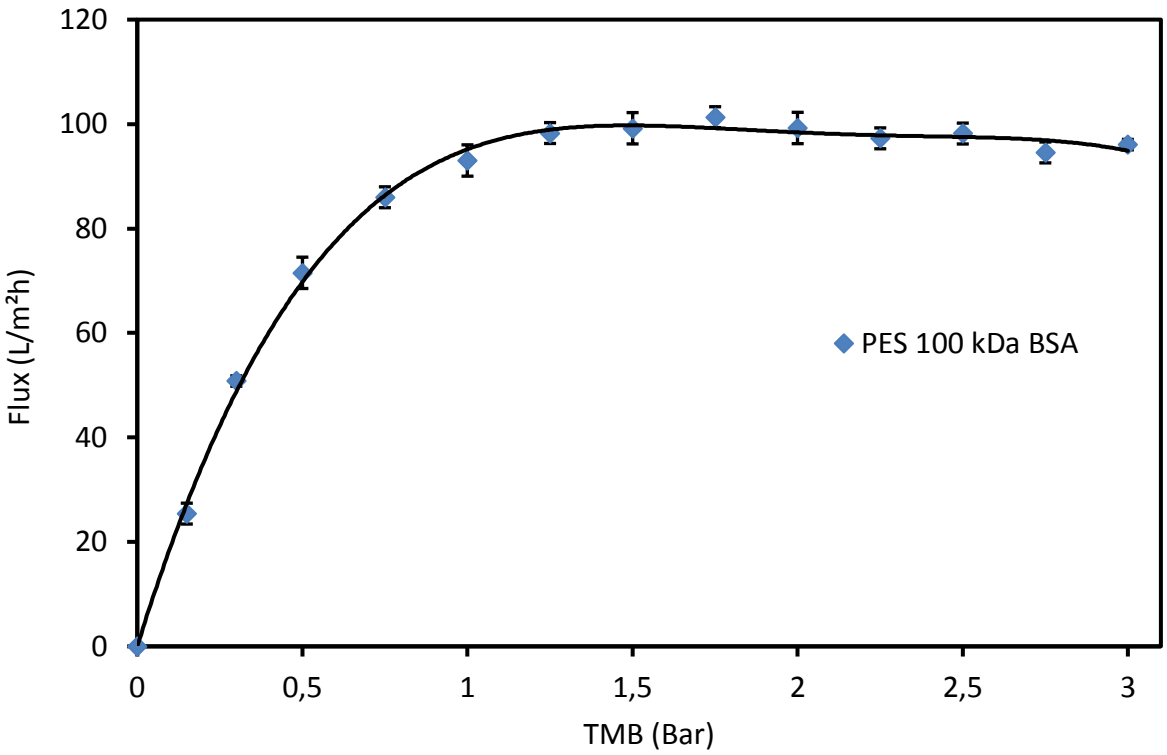

Figure A.8

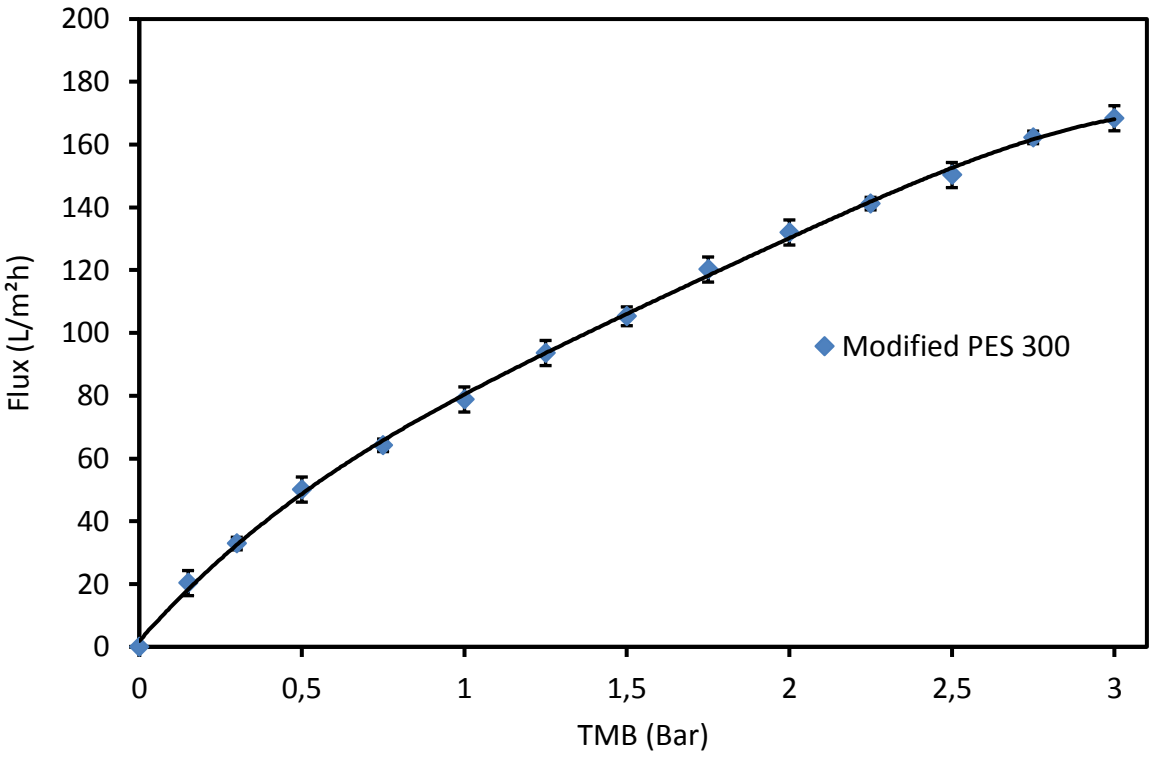

Figure A.9

Table A.2:

TMP (bar)	Flux (L/m²h) RC 100	Flux (L/m²h) PES 100	Flux (L/m²h) Modi-PES 300	Slope = DY/DX
X	Y	Y	Y	
0	0	0	0	**RC 100 kDa**
0.15	45.40349212	25.42081609	20.2000	303
0.3	**90.79264241**	**50.80313894**	32.9000	302.5943353
0.5	181.3721399	71.51685282	50.1000	452.8974874
0.75	219.5659008	85.9841865	71.5000	**PES 300 kDa**
1	221.3502053	93.02495556	92.9000	169.4721073
1.25	205.9666071	98.28142013	114.6000	169.2154857
1.5	185.9052378	99.19768459	136.1000	103.5685694
1.75	167.9175196	101.3195602	**150.3000**	**Modi-PES 300 kDa**
2	154.7522459	99.24590904	170.3000	84.6107000
2.25	145.9753968	97.26870677	180.4000	85.0100121
2.5	135.5106921	98.18497124	201.9000	… 56.0400121
2.75	129.4826364	94.56813782	223.4000	-
3	120.7057873	96.06309563	244.9000	-

8.5 Additional SEM Images

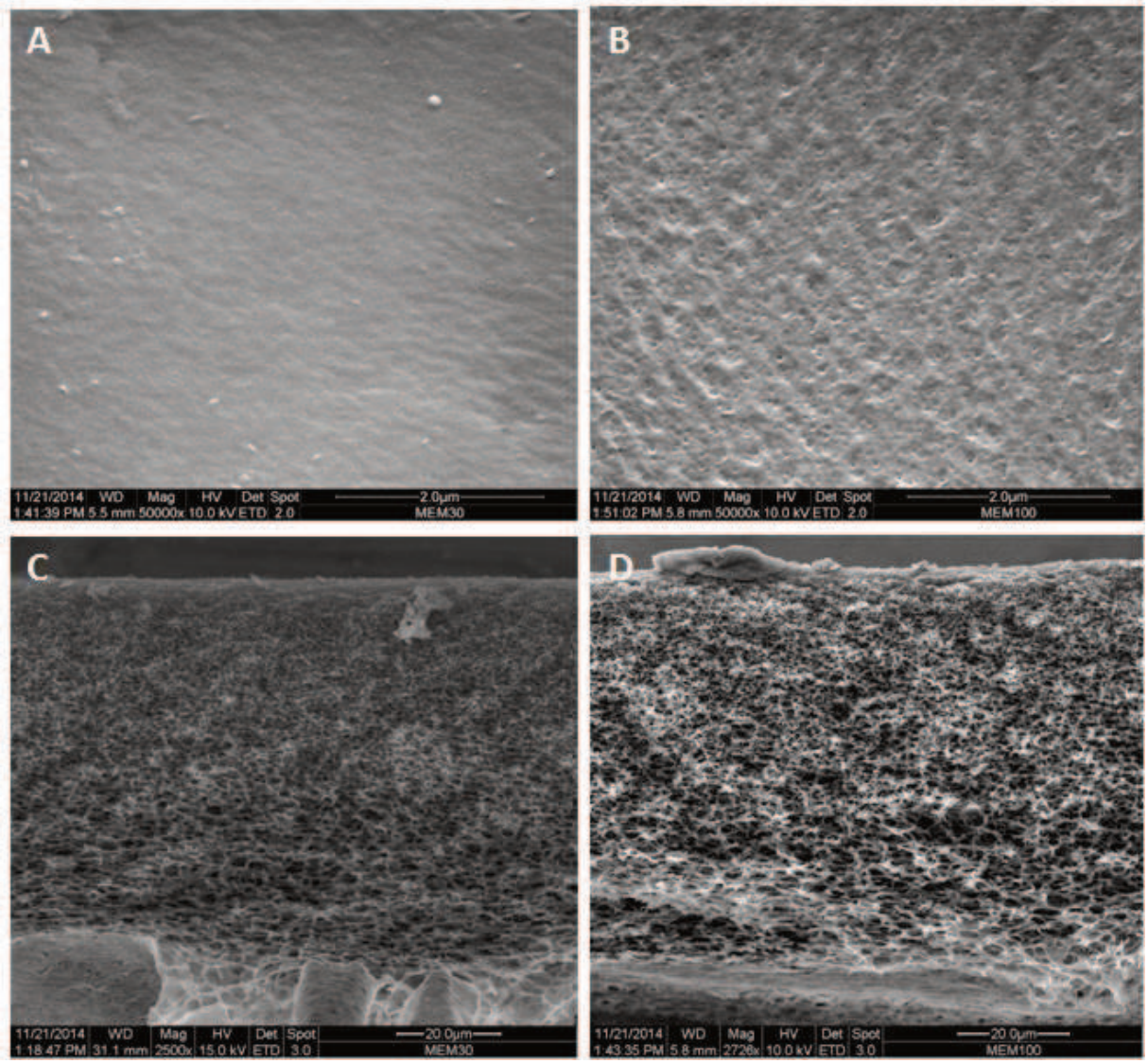

Figure A.10: SEM images of the RC membranes (A/C 30 kDa, B/D 100 kDa): (A & B) barrier surface; (C & D) cross-sectional view showing partly the surface of the barrier layer and the anisotropic pore structure over the cross-section.

8.6 List of publications

8.6.1 During doctoral study

N. Alele, M. Ulbricht, Membrane-based purification of proteins from nanoparticle dispersions: Influences of membrane type and ultrafiltration conditions, Separation and Purification Technology, 158 (2016) 171-182.

N. Alele, R. Streubel, L. Gamrad, S. Barcikowski, M. Ulbricht, Ultrafiltration membrane-based purification of bioconjugated gold nanoparticle dispersions, Separation and Purification Technology, 157 (2016) 120-130.

8.6.2 During masters study

Y. P. Jimenez, N. Alele, H. R. Galleguillos, M. Ulbricht, "Nanofiltration separation of aqueous polyethyleneglycol-salt mixtures", Separ. Sci. Techn. 2013, 48, 1298-1307.

8.7 Participation in conferences

- N. Alele, M. Ulbricht, Poster presentation: "Membrane-based purification of nanoparticle dispersions" 15th Aachener Membran Kolloquium, November 2014, Aachen
- N. Alele, M. Ulbricht, Oral presentation: "Membrane-based purification of nanoparticle dispersions"
  21st International Congress of Chemical engineers and process Engineering, "CHISA" August 2014, Prague, Czech Republic
- N. Alele, M. Ulbricht, Poster Presentation: "Membrane-based purification of nanoparticle dispersions" Gordon Research Seminar (GRS) on Membranes: Materials & Processes, July 5-6, 2014, Colby-Sawyer College, New London, NH, United States
- N. Alele, M. Ulbricht, Poster Presentation: "Membrane-based purification of nanoparticle dispersions" Gordon Research Conference(GRC) Membranes: Materials & Processes, July 6-11, 2014, Colby-Sawyer College, New London, NH, United States
- N. Alele, M. Ulbricht, Poster Presentation: "Membrane-based purification of nanoparticle dispersions" - Neuentwicklungen Cross Flow Filtration - Membranen, Module und Prozesse, April 2014, DECHEMA-Haus, Frankfurt am Main
- N. Alele, M. Ulbricht, Poster presentation: "Nanofiltration separation of aqueous polyethyleneglycol-salt mixtures" 14th Aachener Membran Kolloquium, November 2012, Aachen

“The online version does not contain curriculum vitae due to data protection”